UNIVERSITÀ
DEGLI STUDI
FIRENZE

DOTTORATO DI RICERCA IN ENERGETICA E TECNOLOGIE INDUSTRIALI E AMBIENTALI INNOVATIVE

CICLO XXXI
COORDINATORE Prof. Maurizio De Lucia

Advanced CFD Modelling of Multi-Stage Axial Compressors

Settore scientifico disciplinare ING-IND/08

PhD Candidate
Eng. Lorenzo Cozzi

Tutor
Prof. Andrea Arnone

Co-ordinatore
Prof. Maurizio De Lucia

Firenze 2015/2018

UNIVERSITÀ
DEGLI STUDI
FIRENZE

DOTTORATO DI RICERCA IN ENERGETICA E TECNOLOGIE INDUSTRIALI E AMBIENTALI INNOVATIVE

CICLO XXXI
COORDINATORE Prof. Maurizio De Lucia

Advanced CFD Modelling of Multi-Stage Axial Compressors

Settore scientifico disciplinare ING-IND/08

PhD Candidate
Eng. Lorenzo Cozzi
Department of Industrial Engineering, Univerity of Florence

Tutor
Prof. Andrea Arnone
Department of Industrial Engineering, Univerity of Florence

Co-Tutor
Doc. Filippo Rubechini
Department of Industrial Engineering, Univerity of Florence

Firenze 2015/2018

«Et il n'est rien de plus beau que l'instant qui précède le voyage, l'instant où l'horizon de demain vient nous rendre visite et nous dire ses promesses». Milan Kundera

Contents

Acknowledgements

I would like to warmly thank all those with whom I have had the pleasure to work during my PhD studies.

First of all, I would like to express my very great appreciation to my co-tutor, Dr. Filippo Rubechini, for its patient guidance, motivation, enthusiasm and immense knowledge. He has been a great help in all the activities I carried out in the last years.

Then, I would like to pay special thankfulness to my tutor, Prof. Andrea Arnone, that encouraged me to continue my studies in the field of turbomachinery and allowed me to join his research group.

Special thanks should also be given to Dr. Michele Marconcini, for all his valuable and constructive suggestions that helped me a lot during my PhD cycle.

Furthermore, completing my PhD path would have been way more difficult without the support and friendship provided by my colleagues of the T-group. I am indebted to them for their help.

Finally, I wish to thank my family, that strongly supported and encouraged me during all my education. In particular, I would like to dedicate this thesis to the memory of my beloved grandfather Bruno, that led a life full of sacrifices and hard work in order to donate a solid future to his family. An eternal gratitude and deep love for him will survive in me till my last breath.

Abstract

The axial compressors of power-generation gas turbines have a high stage count, blades with low aspect ratios and relatively large clearances in the rear section. These features tend to promote the development of intense secondary flows that, coupled with the severe diffusion characterizing these machines, make the CFD modelling of axial compressors a great challenge.

The focus of this thesis is on the use and tuning of modern CFD methods able to assess a reliable numerical setup to be used by the industry as a base for the design of efficient and high-performing multi-stage axial compressors.

The first part of the work includes the details about the development and implementation of a highly conservative non-reflecting mixing plane model in the in-house CFD code TRAF, able to handle both the perfect and the real gas case.

Later, the numerical setup for steady-state multi-stage compressor simulations is presented, providing also details about some crucial aspects of the compressor modelling, namely shroud leakages and clearances. The setup has been validated against experimental data on a GT compressor designed by Ansaldo Energia. To determine the influence of mixing plane models on performance prediction, unsteady full-annulus simulations have been performed at two different operating conditions: design point and near-stall.

Finally, the last part of the thesis is dedicated to well-known phenomenon of radial mixing in axial compressors. The physical causes of radial mixing are discussed in depth, leading to the conclusion that a state-of-the-art, unsteady calculation of the

full compressor is able to provide very strong evidence of radial mixing. A special attention is devoted to the evaluation of what is lost in the compressor modelling due to the assumption of a steady-state picture of the flow. In order to do this, the high-pressure section of a heavy-duty axial compressor of the Ansaldo Energia fleet, characterized by really high clearances, is considered. The results of steady and unsteady RANS simulations are compared with experimental data, showing that only adopting an unsteady approach, the enhanced radial mixing of this peculiar application can be properly captured. On the contrary, the steady-state modelling leads to a strong underestimation of the radial transport phenomenon. A possible explanation for this is provided after examining what occurs across the inter-row interfaces for RANS and URANS solutions: the stream-wise vorticity associated with clearance flows is one of the main drivers of radial mixing and restraining it by pitch-averaging the flow at mixing planes is the reason why the RANS approach is not able to properly predict the radial transport of fluid properties in the rear part of the axial compressor.

Nomenclature

A	Cross-sectional area
c	Absolute velocity/speed of sound
CFD	Computational fluid dynamics
CFL	Courant-Friedrichs-Lewy number
c_p	Specific heat at constant pressure
DFT	Discrete Fourier transform
E	Total internal specific energy
F	Flux/flow function
GT	Gas turbine
h	Enthalpy
H	Total enthalpy
i	Incidence angle
IGV	Inlet guide vanes
k	Thermal conductivity
l	Blade chord
LES	Large eddy simulation
$\dot{m}$	Mass-flow
Ma	Mach number
n	Normal vector
NRBC	Non-reflecting boundary conditions
OGV	Outlet guide vanes
p	Pressure
Pr	Prandtl number
PR	Pressure ratio
R	Reaction/residual
RANS	Reynolds-averaged Navier-Stokes
RBC	Reflecting boundary conditions
s	Row pitch/Entropy

T	Temperature
t	Time
U	Rotational speed
u	X velocity component
URANS	Unsteady Reynolds-averaged Navier-Stokes
v	Relative velocity/y velocity component
w	Relative velocity/z velocity component
W	Specific work

Greek

α	Absolute flow angle
β	Relative flow angle
γ	Specific heats ratio
δ	Deviation angle
ε	Mixing coefficient
η	Efficiency
θ	Camber angle/circumferential direction
μ	Dynamic viscosity
ξ	Stagger angle
ρ	Density
σ	Row solidity/relaxation factor
φ	Generic flow quantity
ϕ	Flow coefficient/characteristic variable
χ	Metal angle
ψ	Load coefficient
ω	Vorticity

Subscripts

0	Stagnation quantity
c	Convective
d	Diffusive
F	Mixed-out value

is/ss	Isentropic transformation
l	Laminar
p	Polytropic/profile/primitive
R	Radial direction/rotor
ref	Reference quantity
rel	Relative quantity
S	Stator
t	Turbulent

1 Introduction

The current trend of the energy market sees an always increasing importance of the power produced by renewable sources as, just to mention some, wind and solar energy. The main issue related with most of these sources is the fact that they cannot perfectly follow the energy demand of the market and, until affordable and reliable ways of large energy storage are introduced, they need to be supported by conventional energy conversion power plants based on fossil fuels.

Due to their high flexibility and reliability, gas turbines still have a prominently strategic role in the present energy horizon, as they can shortly answer to a peak request from the electric grid that could not otherwise be satisfied. Nevertheless, GT engineers that were traditionally used to design and test these machines to work for most of their lifetime close to nominal operating conditions had to start considering, especially in the last years, more complex lifecycles. The reliability of the numerical tools used in the design phase, at present day adopted also to evaluate operating conditions really far from the nominal one, is hence acquiring an increasing importance for the GT industry. This because in a complex lifecycle full of start/stop procedures, the risk of failures must be carefully considered, and an incorrect machine performance analysis can mislead designers and result in a shorter life of the components and an increased maintenance cost.

In recent years, high-fidelity CFD approaches are spreading throughout the academia and are slowly reaching the R&D in-

dustrial departments. However, when dealing with high-Reynolds applications, such as multi-stage industrial turbomachines, the huge computational cost of these really accurate models just confines their applicability to small computational domains (e.g. a thin span-wise portion of one row or, at most, one stage). Some efforts are being made in order to transfer the information gathered from high-fidelity LES analyses to less accurate RANS models [1] [2], but the latter still remain the standard adopted by the industry, as they are at present the optimal trade-off between computational cost and simulation accuracy.

Even in the framework of the RANS modelling, the unsteady approach is not yet suitable for the routine design practice of turbomachines with a high stage count, as axial compressors of heavy-duty GTs. In particular, the use of URANS computations is generally limited to the design validation phase and to research activities aimed at investigating flow features influenced by blade rows interactions [3]. As steady-state RANS modelling of turbomachinery flows is, at present day and in the near future, the standard industrially used to design high stage count turbomachines, any model improvement is an asset that could bring remarkable benefits.

1.1 Thesis objectives and outline

Multi-stage axial compressors have always been a great challenge for designers since the flow within them is subjected to severe diffusion and is usually characterized by complex and widely developed 3D structures, especially next to the endwalls.

The development of reliable numerical tools capable of providing an accurate prediction of the overall compressor performance is a topic of a great interest to both the scientific community and the industry. The focus of this work is indeed on

the use and tuning of a state-of-the-art numerical setup for multi-stage simulations on axial compressors.

In particular, after a general introduction about the fundamentals of compressor aerodynamics reported in chapter 2, the details of the implementation of a non-reflecting mixing plane model for steady-state RANS simulations in the in-house CFD code TRAF, are presented in chapter 3. This newly implemented model is characterized by improved fluxes conservation properties in terms of both mass-flow and total temperature. More importantly, it has been extended to the real gas version of the code, making it ready to be used as a standard for every kind of multi-row turbomachinery application that could be properly treated with a steady-state approach.

Moreover, the numerical setup for multistage axial compressor steady simulations, developed in the framework of the collaboration between Ansaldo Energia and the University of Florence, is presented in chapter 4. Some key aspects of the compressor modelling are addressed, such as mixing planes, shroud leakages and rotor tip clearances. The setup has been validated against experimental measurement on a GT compressor of the Ansaldo Energia fleet. Furthermore, the results of unsteady full-annulus computations of a whole 15-stage compressor at two different operating conditions, namely design and near-stall, are compared with steady-state analyses to evaluate the influence of mixing plane models on performance prediction. The outline of the numerical setup, together with the abovementioned validation and results, has been included in a publication [4] presented at ASME Turbo Expo 2017.

Additionally, in chapter 5, the results of steady and unsteady RANS simulations on the high-pressure section of an industrial heavy-duty axial compressor are presented and compared with

experimental data. Adopting an unsteady full-annulus URANS approach, the enhanced radial mixing in the rear stages of the compressor is properly captured, obtaining a really good agreement with experimental data both in terms of total temperature and pressure outlet radial distributions. On the contrary, with a steady-state modelling, the radial transport is strongly underestimated, leading to results with marked departures from experiments. Examining what occurs across the inter-row interfaces for RANS and URANS solutions, a possible explanation for this underestimation is provided. In particular, as the stream-wise vorticity associated with clearance flows is one of the main drivers of radial mixing, restraining it by pitch-averaging the flow at mixing planes of a steady-state analysis is the reason why this simplified approach is not able to properly predict the radial transport of fluid properties in the rear part of the axial compressor. The content of the last part of this work has been collected in a publication [5] presented at ASME Turbo Expo 2018. This paper has been accepted for publication on the ASME Journal of Turbomachinery (currently in publication phase, reference TURBO-18-1184).

Finally, the concluding remarks and some future developments sparkling from the work reported in this thesis are reported in chapter 6.

2 Fundamentals of Axial Compressor Aerodynamics

The foundations of the aerodynamics of an axial compressor are presented in this chapter. After a brief section introducing an historical perspective about axial compressors, in the second part of the chapter some bases about the design of these really challenging turbomachines are provided to the reader.

2.1 Historical perspective

The idea of "reversing" a reaction turbine to create an axial compressor dates back to the end of the 19^{th} century. As recorded by Stoney [6], in 1884 Sir Charles Parsons registered a patent connected with a reversed turbine used as an axial compressor. Around the beginning of the 20^{th} century, Parsons built some of these turbomachines basing the blade design on propeller sections. The first compressors were used in blast furnaces, operating with delivery pressures in the range between 0.1 and 1 bar and attaining efficiencies around 55%. Parsons designed and built also a high-pressure compressor, with a delivery pressure of 5.5 bar, but this machine had several issues (mainly connected with unstable operating conditions and surge) that forced the designer to finally give up the project. In the 1940s, Howell [7] stated that a high pressure-ratio axial compressor designed simply reversing a turbine could lead to an efficiency lower than 40%.

Due to these generally low values of efficiency, axial compressors were abandoned in favor of more effective multi-stage centrifugal compressors that could reach higher efficiencies up to $70 \div 80\%$.

There were no further developments in the axial compressor field till the 1920s, when the basic principles of Griffith's airfoil theory of compressor and turbine design were published. From that moment on, the history of axial compressors is strongly connected with the one of aeronautical gas turbines [8] [9]. Through research efforts developed in several years, the team led by Griffith concluded that efficiencies over 90% could be achieved for stages with a relatively low pressure-ratio. This assumption was confirmed later by experimental test rigs.

The difficulties that characterized the early development of axial compressors were mainly connected with the fundamentally different flow process compared with the one typical of axial turbines. While in turbines the flow in each row is accelerated in the relative frame of reference, in compressors it is decelerated (i.e. subjected to diffusion). A fluid can rapidly accelerate through a blade passage with just a small or moderate total pressure loss, but in case of a severe diffusion large losses arise due to blade stall typical of flow conditions with a strong adverse pressure gradient.

In order to limit the losses, diffusion and turning for each blade passage must be substantially restricted. These limitations are the reason why axial compressors need more stages that an axial turbine for a given pressure-ratio.

The overall performance of axial compressors strongly depends on the application for which they are designed. In heavy-duty and industrial applications aerodynamic efficiency is one of the main design drivers, while in the field of aeronautical gas turbines designers are more focused on maximizing the work done per stage preserving anyway an acceptable level of overall efficiency, in order to limit the compressor stage count and hence the engine weight. For the latter case, it is worth to emphasize

that an increased stage loading almost inevitably leads to some aerodynamic constraint. Pushing to operating conditions involving high Mach numbers, this constraint is more severe due to possible shock-induced boundary layer separation or increased losses arising from intense flow diffusion.

An outline of the history of high-loaded axial compressors has been published by Wennerstrom [10]. In this document, special emphasis is given to the importance of reducing the number of stages and to the possible ways to achieve an improved performance.

An important change in a design feature of multi-stage axial compressors was adopted around the 1970: from that moment on, low aspect ratio blading started to be introduced in these machines. Despite the fact that blades with a large chord seemed to go against the trend of making engines more compact and lighter, as reviewed by Wennerstrom [11], the increased usage of low aspect ratio blading in aircraft axial compressors led to higher loading capability, higher efficiency and wider operating range with respect to higher aspect ratio configurations. This general trend characterized by a rise in row solidity and a fall in blade aspect ratio was mostly due to an increase in the chord length, and has also been reported by Wisler [12] in a comprehensive set of lecture notes referring mainly to the work of General Electric (GE). One of the key consequences of this new design strategy was the significant increase in the pressure rise per stage and in the overall pressure ratio of a single compressor. Large chord blades have the main advantage of being more effective in the endwall regions, the ones that are crucial in determining both the stall point and the efficiency. One of the first examples of machine adopting low aspect ratio blades was an axial-flow compressor that achieved a pressure ratio of 12.1 in

only five stages, with an isentropic efficiency of 81.9% and an 11% stall margin, with a flow rate per unit frontal area of 192.5 kg/(sm^2) [13]. For this compressor, the aspect ratio of its rows ranged from 1.0 to 1.2.

2.2 Compressor design

In the early design phase of an axial compressor the calculations are generally performed at a mean radius through the machine. This kind of approach is particularly appropriate if the blade height is small compared to the mean radius, while further refinements should be introduced to assess the aerodynamic loadings also at hub and casing sections for configurations with a small hub to tip radius ratio.

2.2.1 Compressor stage

The stage of a compressor is defined as a rotor blade row followed by a stator blade row. The blades of the rotor row are mounted on the rotor drum while the stator blades are fixed to the machine outer casing. The blades of the row immediately upstream of the first rotor row are referred to as inlet guide vanes (IGV). This stator row is not considered to be part of the first stage and is generally treated separately. Its function is quite different from the other rows as it accelerates the flow rather than diffusing it.

2.2.2 Velocity triangles

The mean-line design is based on the stage velocity triangles, as the ones reported in Figure 2.1. The flow exiting an upstream stage or the guide vanes has an absolute velocity c_1 and direction α_1 with respect to the machine rotating axis. The relative velocity vector at the rotor inlet section, with magnitude w_1 and direction β_1, can be obtained by subtracting vectorially the blade rotational speed U from the absolute velocity vector. In

the relative frame of reference, the flow is then turned across the rotor to the direction β_2 with an outlet velocity w_2. Adding vectorially the blade speed U onto w_2 gives the absolute velocity at the rotor exit section, c_2 at angle α_2.

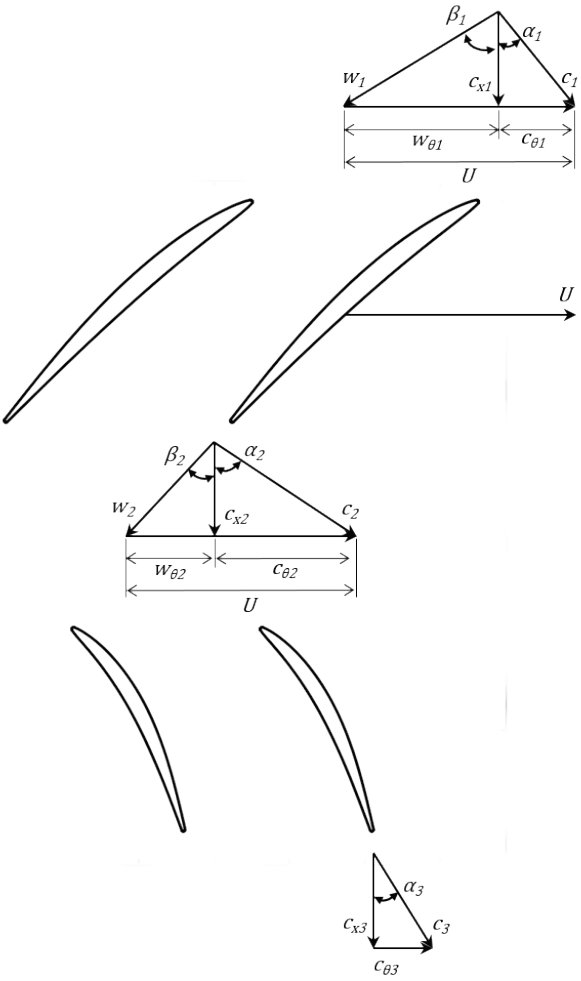

Figure 2.1 Velocity triangles for a compressor stage

The stator row then deflects the flow toward the axis, leading to an exit velocity c_3 at angle α_3. For a repeating or normal stage of a multi-stage axial compressor, the absolute velocity vector at the stage outlet section has the same magnitude and direction of the flow entering the rotor row. In every compressor stage, both the relative velocity in the rotor and the absolute velocity in the stator decrease. This diffusion of kinetic energy significantly influences the stage efficiency.

2.2.3 Flow deflection, incidence and deviation

The main geometrical features of a compressor blade profile are highlighted in Figure 2.2.

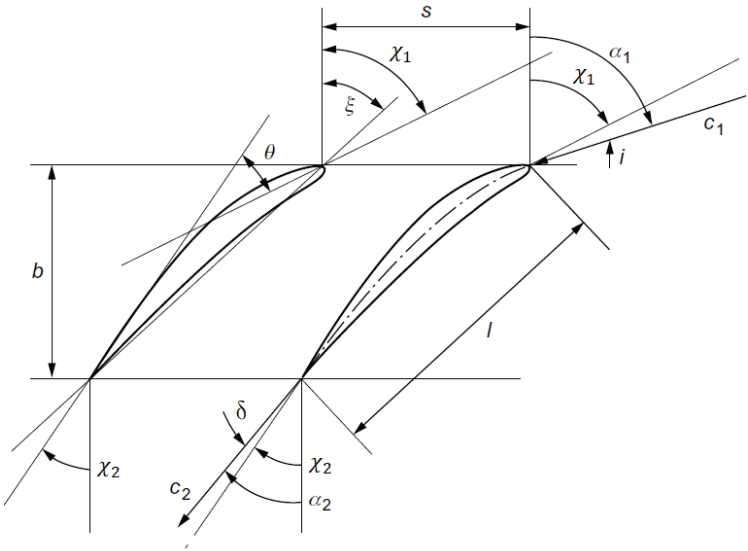

Figure 2.2 Main geometrical parameters of compressor blade profiles

Between these parameters, a really important one characterizing the aerodynamics of the profile is the flow deflection, that is the

change in angle of the flow due to the presence of the blade. In general, this will be different to the camber angle due to flow incidence at the leading edge and deviation at the trailing edge.

The incidence angle is the difference between the inlet flow angle α_1 and the blade inlet angle χ_1:

$$i = \alpha_1 - \chi_1 \tag{1}$$

At the design point of a compressor blade, the inlet flow angle is almost parallel to the camber line at the leading edge (i.e., the inlet blade angle). Hence, there is close to zero incidence and almost all the deflection, or turning, of the flow is achieved via the camber of the blades. As the incidence is increased, the flow impinges on the blade pressure surface, and the flow on the suction surface must rapidly accelerate around the leading edge then it decelerates to a speed comparable with the mainstream flow. This leads to very high local diffusion close to the front of the blade and sometimes what is referred to as a leading edge spike on the blade suction surface. The diffusion can cause boundary layer transition and, thus, higher blade losses, and at very high incidences the flow will separate, leading to stall. With positive incidence, the flow deflection is increased. Some of the turning can be thought of as being due to the blade camber, and some due to the incidence. At negative incidence, the flow accelerates around the leading edge onto the pressure surface. The pressure distributions on the front of the suction and pressure surfaces swap and the diffusion on the pressure surface is increased. The flow deflection is reduced in this case and at very high values of negative incidence, the diffusion becomes so high that the flow can separate on the pressure surface.

The tolerance of the compressor blades to incidence variations is critical to enable stable and efficient off-design operation of a

compressor. When a compressor operates at mass-flow rates or rotational speeds that are away from the design point, the blades experience incidence variations. Typically, a compressor blade needs to tolerate at least $\pm 5°$ variation of incidence without stalling, although the exact requirements will depend on the application. The variations in incidence that can be tolerated by a compressor airfoil reduce as the inlet Mach number increases.

The direction of the flow leaving a compressor blade does not follow the profile camber line at the trailing edge. The difference between the outlet flow angle and the blade outlet angle is referred to as deviation. This deviation arises predominantly because of inviscid effects since the diffusion within the blade passages is associated with diverging streamlines and therefore the flow is not moving in a single direction. This contribution is intensified when increasing the spacing between the blades, because the uncovered part of the channel increases and the flow is less guided by the blades. Moreover, the deviation is further increased by viscous effects since the boundary layer blockage modifies the effective blade shape.

A widespread empirical relationship between the nominal deviation δ and the blade geometry is the one proposed by Carter [14] in 1950, commonly called "Carter's rule" and valid for a blade operating at design condition:

$$\delta = m\theta \left(\frac{s}{l}\right)^n \tag{2}$$

Where n is equal to 0.5 for compressor cascades and 1.0 for compressor inlet guide vanes, while θ is the blade camber, s is the pitch and l is the chord.

This relation reflects the fact that the deviation increases with pitch-to-chord ratio and blade camber. The value of m depends on the camber line shape and the blade stagger. A typical correlation for m in a compressor cascade is:

$$m = 0.23\left(\frac{2a}{l}\right)^2 + \frac{\beta_2}{500} \tag{3}$$

In which a is the distance between the leading edge and the point with maximum camber of the blade. Deviation increases further going towards off-design conditions, and any flow separation will cause a rapid increase in δ.

2.2.4 Blade loading

The choice of a satisfactory blade loading, pressure rise and maximum Mach number is generally based on proper design criteria. As far as blade loading is concerned, it is usually assessed using the diffusion factor DF [15] or alternatively the diffusion ratio DR [16], both introduced by Lieblein. The definitions for these two parameters are the following:

$$DF = \left[1 - \frac{c_2}{c_1}\right] + \frac{\Delta c_\theta}{2\sigma c_1} \tag{4}$$

$$DR = \frac{c_{max}}{c_2} \tag{5}$$

In the equation (4), σ is the compressor row solidity i.e. the chord-to-pitch ratio, while Δc_θ is the tangential velocity variation across the row. The first term on the right-hand side of equation (4), $1 - c_2/c_1$, represents the mean deceleration of the flow. The second term, $\Delta c_\theta/2c_1$, represents the flow turning.

The pitch-to-chord ratio determines how well the flow is guided by the blades. A low value implies lower pressure gradients across the blade passages required to turn the flow and, hence, lower diffusion. Lieblein showed that the loss in a blade row increases rapidly as the flow starts to separate, and this occurs when the diffusion factor exceeds about 0.6. Typically, a well-designed blade with moderate loading will operate with a diffusion factor around 0.45. Although it was developed using just a small range of compressor blade designs operating at a minimum loss condition, the diffusion factor is widely applied to a range of compressor designs, both compressible and incompressible, for preliminary design purposes.

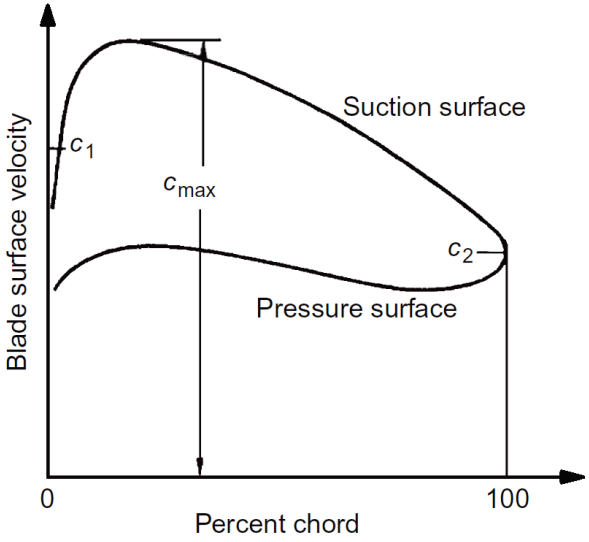

Figure 2.3 Isentropic velocity distribution on the blade surface

As far as the equation (5) is concerned, the velocity c_{max} is the maximum isentropic velocity on the blade suction side (see Figure 2.3).

Another, really simple, measure of the overall amount of diffusion through a compressor blade row is known as the De Haller number, c_2/c_1 [17]. This parameter is still often used to limit the maximum pressure rise across a compressor blade row. De Haller's rule recommends that:

$$\frac{c_2}{c_1} \geq 0.72 \tag{6}$$

2.2.5 Compressor stage thermodynamics

Considering the purely axial compressor stage whose velocity triangles are reported in Figure 2.1 and assuming stationary and adiabatic flow, the specific work done by the rotor on the fluid is:

$$\Delta W = h_{02} - h_{01} = U(c_{\theta 2} - c_{\theta 1}) \tag{7}$$

For axial machines, where there is no radial shift of the streamlines across the rotor (i.e. $U_1 = U_2$), the total relative enthalpy is constant across this row:

$$h_1 + \frac{1}{2}w_1^2 = h_2 + \frac{1}{2}w_2^2 \tag{8}$$

Across the stator row, the quantity that is constant is the total enthalpy:

$$h_2 + \frac{1}{2}c_2^2 = h_3 + \frac{1}{2}c_3^2 \tag{9}$$

The thermodynamic process occurring across the compressor stage is reported in the Mollier diagram of Figure 2.4. The diagram has been generalized to consider the effects of irreversibility.

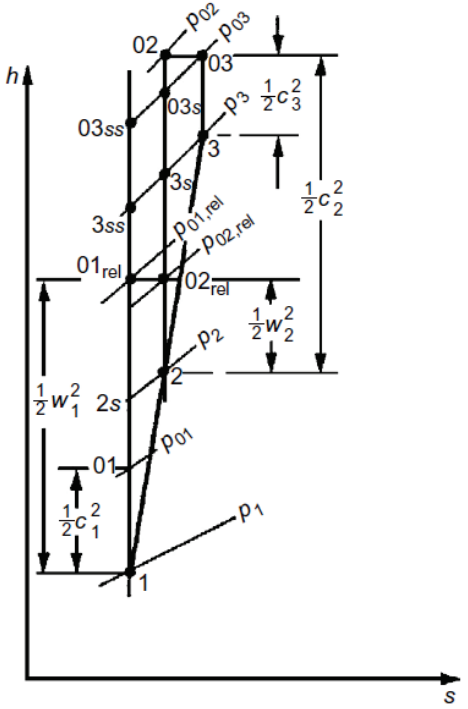

Figure 2.4 Mollier diagram for an axial compressor stage

2.2.6 Stage efficiency and losses

Combining equations (7) and (9), the specific work absorbed by the compressor stage can be expressed as:

$$\Delta W = h_{03} - h_{01} \tag{10}$$

Referring to Figure 2.4, the reversible or minimum specific work needed to attain the same final stagnation pressure of the real process is:

$$\Delta W_{min} = h_{03ss} - h_{01} = (h_{03} - h_{01}) - (h_{03} - h_{03ss}) \qquad (11)$$

There are two main ways of expressing the isentropic efficiency, that is the efficiency resulting from a comparison between the real transformation and an isentropic one. The choice of the definition to be used depends largely upon whether the exit kinetic energy is usefully employed or is wasted. If the exhaust kinetic energy is useful, then the ideal compression is to the same stagnation (or total) pressure as the actual process. This efficiency is referred to as total-to-total stage efficiency and is defined as:

$$\eta_{tt} = \frac{\Delta W_{min}}{\Delta W} = \frac{h_{03ss} - h_{01}}{h_{03} - h_{01}} \qquad (12)$$

A case in which the exhaust kinetic energy is not wasted is the last stage of an aircraft gas turbine engine, where it contributes to the propulsive thrust. Similarly, the kinetic energy exiting one stage of a multi-stage compressor can be used in the following stage and is not wasted.

On the contrary, if the exhaust kinetic energy cannot be usefully employed and is entirely unexploited, the ideal compression is to the same static pressure as the actual process, with zero exit kinetic energy. This efficiency is referred to as total-to-static stage efficiency and has the following expression:

$$\eta_{ts} = \frac{h_{3ss} - h_{01}}{h_{03} - h_{01}} \tag{13}$$

A situation where the outlet kinetic energy is completely wasted is a compressor exhausting directly into a plenum without a diffuser. By comparing equations (12) and (13), it is clear that the total-to-static efficiency is always lower than the total-to-total efficiency. The total-to-total efficiency relates to the internal losses (entropy creation) within the compressor, whereas the total-to-static efficiency relates to the internal losses plus the wasted kinetic energy.

The isentropic efficiency described above, although fundamentally valid, can be misleading if used for comparing turbomachines operating with a different overall pressure ratio.

In order to overcome this issue, another definition of efficiency can be introduced. Any turbomachine can be regarded as being composed of a large number of very small stages. If each small stage has the same efficiency, then the isentropic efficiency of the whole machine will be different from the small stage or polytropic efficiency, the difference depending on the machine pressure ratio.

Considering the perfect gas case, the polytropic efficiency for the small stage is:

$$\eta_p = \frac{dh_{is}}{dh} = \frac{dp/\rho}{c_p dT} = \frac{\gamma - 1}{\gamma} \frac{dp/p}{dT/T} \tag{14}$$

Then, rearranging the previous expression and integrating across all the compression transformation:

$$\frac{T_2}{T_1} = \left(\frac{p_2}{p_1}\right)^{(\gamma-1)/\eta_p \gamma} \tag{15}$$

Hence, the polytrophic efficiency for the case considered is given by:

$$\eta_p = \frac{\gamma}{\gamma - 1} \frac{\ln(p_2/p_1)}{\ln(T_2/T_1)} \tag{16}$$

A really important effect that is somehow a counterpart of the efficiency is the aerodynamic loss that arises across a row of the compressor. As for efficiency, also in this case the overall aerodynamic loss can be expressed through a proper coefficient, that assumes a different definition for stationary and rotating rows. Starting from the case of a stator row, the related loss coefficient is defined as:

$$Y_{p,stator} = \frac{p_{02} - p_{03}}{p_{02} - p_2} \tag{17}$$

Therefore, the measure of the aerodynamic loss across the row is given by the ratio of total pressure drop to the inlet dynamic pressure.

As far as the rotor row is concerned, the loss coefficient is characterized by the following expression:

$$Y_{p,rotor} = \frac{p_{01,rel} - p_{02,rel}}{p_{01,rel} - p_1} \tag{18}$$

The loss coefficient is, in this case, evaluated with respect to relative quantities.

In a compressor stage, there are many loss sources causing the generation of entropy. The sum of all the entropy creation across a blade row determines the loss coefficients presented above. The loss sources can be categorized as 2D and 3D. The possible 2D loss sources are:

- the blade boundary layers
- trailing edge mixing
- flow separation
- shock waves

The total 2D loss for a compressor stage can be determined through cascade tests or 2D computational methods, but there are no general correlations that can be applied to all cases. In general, the boundary layer and the trailing edge mixing loss cannot be avoided and their value is strongly dependent on the blade surface pressure distribution. On the contrary, separation losses can be avoided (at least at design operating condition) adopting well-designed compressor blades. However, moving towards off-design conditions, the diffusion level becomes higher and the flow can separate leading to excessive loss and possible stall or surge. Shock wave losses arise only for the case of transonic stages, generally the front ones of a multi-stage axial compressor.

As far as 3D losses are concerned, the main ones impacting on the overall compressor performance are:

- end wall loss
- tip leakage loss

The total 3D loss is often simply referred to as secondary flow loss. This because the two loss sources that have been mentioned strongly interact and are difficult to isolate.

Annulus boundary layers increase rapidly along the hub and casing of a compressor. They are swept across the blade passage by the pressure difference between the pressure and the suction surfaces, leading to complex 3D flow structures. These endwall flows cause losses both through viscous shear and mixing with the mainstream flow. In addition, they interact with the boundary layers on the blade surfaces, potentially causing further loss.

Between the many attempts to model and predict the losses caused by compressor endwall generated secondary flows, the work done by Koch and Smith [18] deserves to be mentioned.

Nevertheless, as the endwall boundary layers are generally large and the flow field is highly case-dependent, experimental test results or advanced 3D computational methods are nowadays used to determine endwall loss.

In addition, clearance flows coming from the gap above the tips of compressor rotor blades interact with both the endwall and the primary flow within the passage, creating further losses through mixing and shear. Moreover, the leakage flow causes blockage, reducing the overall flow capacity of the compressor stage and the stable operating range [19].

In order to improve the stability margin and to reduce the losses, the designers always try to minimize the clearance gap, but the minimum value is normally established by manufacturing and mechanical considerations.

Leakage flows are not only related to rotor tip gas. They can also be found at the hub section of stator rows, if they are built

with a cantilever configuration. Such kind of layout is normally introduced to minimize the weight and to relieve the high diffusion at stator hub section, at the price of an increased blockage and further loss. In addition, leakage flows arise from any gaps or seals that are present in the real geometry of a compressor, such as shroud cavities.

The contribution of 3D flows to the total amount of losses within an axial compressor is typically around 50% or more. They also lead to reduced flow capacity due to the additional blockage, reduced work input, and more limited operating range. They need to be accounted for in the preliminary design by using average loss coefficients for the whole flow field and by factoring the velocity triangle parameters appropriately so that they could represent average flow conditions.

2.2.7 Other remarkable parameters

In order to have a complete definition of the velocity triangles at the design condition, some important parameters need to be set, namely the stage loading ψ, the flow coefficient ϕ, and the reaction R.

2.2.7.1 Stage loading

Within the blade passages of a compressor the flow is subjected to diffusion, and in each row of rotors and stators the relative velocity is decreased. The amount of diffusion needs to be limited, to avoid flow separation and possible instable operation resulting in stall or surge. As already introduced, De Haller proposed that the relative velocity at exit from a blade row should be at least 72% of the inlet relative velocity to have satisfactory performance. This prescription is equivalent to limiting the pressure rise and the maximum stage loading. The stage loading ψ for a normal, or repeating, stage has the following expression:

$$\psi = \frac{h_{03} - h_{01}}{U^2} = \frac{\Delta c_\theta}{U} = \frac{c_{\theta 2} - c_{\theta 1}}{U} = \phi(\tan\alpha_2 - \tan\alpha_1) \quad (19)$$

In the previous expression, $\phi = c_x/U$ is the flow coefficient that will be introduced in section 2.2.7.2. Considering the velocity triangles reported Figure 2.1, the equation (19) can be rewritten as:

$$\psi = \phi(\tan\beta_1 - \tan\beta_2) = 1 - \phi(\tan\alpha_1 + \tan\beta_2) \quad (20)$$

The choice of the stage loading at the compressor design point is critical. A value that is too low for this parameter will lead to an excessive number of compressor stages to achieve a required pressure ratio. On the contrary, a value that is too high will limit the operating range of the compressor and increase the number of blades needed to avoid flow separation. This leads to increased profile losses due to the higher wetted area and also leads to problems at high Mach numbers since the increased blade number will increase the possibility of choking. For these reasons the stage loading is generally limited to values around 0.4. However, more advanced aeronautical compressors, where the need to reduce the number of stages is most pressing, may have higher stage loadings.

2.2.7.2 Flow coefficient

For an axial machine, the flow coefficient is given by the ratio of the axial velocity to the local rotational speed:

$$\phi = \frac{c_x}{U} \quad (21)$$

The equation (19) shows that, for a fixed stage loading, as the flow coefficient increases, the flow turning required reduces.

Hence, the diffusion through the row reduces as flow coefficient increases. Similarly, for a fixed level of diffusion, the stage loading can increase as the flow coefficient rises. This suggests that a high flow coefficient is beneficial. Furthermore, higher values of flow coefficient correspond to higher inlet mass flow per unit area, leading to a smaller diameter machine for a given mass-flow.

However, in axial compressors, stage performance is often limited by Mach number effects and, for a given rotational speed, high values of flow coefficient will lead to higher relative Mach number and potentially greater losses from choking and shock waves. Another disadvantage of a higher flow coefficient design concerns the tolerance of the compressor to non-uniform inflow. Compressors need to remain stable in the event of a disturbance in the inlet flow, and lower flow coefficient designs are found to absorb fluctuations more readily than high flow coefficient designs. The reasons for this are detailed in [20].

As a result of these considerations, typical values of ϕ used in designs are between 0.4 and 0.8 and often, at the beginning of the design phase, 0.5 is chosen.

2.2.7.3 Reaction

In general, the reaction for a turbomachinery stage is defined as the ratio of the rotor static enthalpy rise to the stage static enthalpy rise. For the case of a compressor stage as the one considered in this chapter, the reaction is given by:

$$R = \frac{h_2 - h_1}{h_3 - h_1} \tag{22}$$

From equation (8) it is possible to obtain the static enthalpy rise across the rotor in terms of relative velocities:

$$h_2 - h_1 = \frac{1}{2}(w_1^2 - w_2^2) \tag{23}$$

Then, considering a repeating stage ($c_3 = c_1$), the static enthalpy rise across the compressor stage can be written as:

$$h_3 - h_1 = h_{03} - h_{01} = U(c_{\theta 2} - c_{\theta 1}) \tag{24}$$

Substituting the previous expressions in the reaction definition gives:

$$R = \frac{w_1^2 - w_2^2}{2U(c_{\theta 2} - c_{\theta 1})} = \frac{(w_{\theta 1} + w_{\theta 2})(w_{\theta 1} - w_{\theta 2})}{2U(c_{\theta 2} - c_{\theta 1})} \tag{25}$$

It is important to notice that the assumption that c_x is constant across the stage has been considered. From Figure 2.1, $c_{\theta 2} = U - w_{\theta 2}$ and $c_{\theta 1} = U - w_{\theta 1}$ so that $\Delta c_\theta = \Delta w_\theta$. Therefore:

$$R = \frac{w_{\theta 1} + w_{\theta 2}}{2U} = \frac{1}{2}\phi(\tan\beta_1 + \tan\beta_2) \tag{26}$$

Another expression for the reaction, in terms of outlet flow angles of each blade row in a stage, can be obtained from the previous one considering that $w_{\theta 1} = U - c_{\theta 1}$:

$$R = \frac{1}{2} + \frac{\phi}{2}(\tan\beta_2 - \tan\alpha_1) \tag{27}$$

Eliminating β_2 by combining equations (27) and (20), it is possible to derive an equation that relates ϕ, ψ, R and the inter-stage swirl angle α_1:

$$\psi = 2(1 - R - \phi \tan \alpha_1) \tag{28}$$

From this equation, it is possible to notice that a higher reaction tends to reduce the stage loading, which is normally good for a compressor. Nevertheless, in most of the cases a 50% reaction is used to equally share the adverse pressure gradient through the rotor row and stator row. A 50% reaction also means that the rotor and stator blades tend to have similar shapes. In particular, when choosing a 50% reaction, the stage velocity triangles are symmetrical ($\alpha_1 = \beta_2$).

However, an interesting work published by Dickens and Day [21] shows that, for stages with high loading, high reaction is required to achieve optimum efficiency. The explanation for this provided by the authors is that it is necessary to reduce the pressure rise across the stator row because it is more susceptible than the rotor to large separations.

Anyway, in many cases, the reaction is simply a consequence of other design choices. Just to mention an example, in a design where both the stage loading and the flow coefficients have already been chosen, if the inlet swirl angle α_1 is fixed (e.g. axial inflow for a first row or an IGV upstream of the stage), then the reaction must also be fixed.

In advanced compressor designs, especially in aero-engines, high reaction is common and values between 0.5 and 0.8 are the ones generally adopted.

2.2.7.4 Inter-stage swirl angle

From equation (28), it can be noticed that a positive swirl between the stages reduces the stage loading. Furthermore, a positive swirl angle also reduces the relative inlet Mach number at

rotor inlet section. That is why advanced multistage compressors, especially the ones for gas turbine applications, tend to have an inter-stage swir1 angle of around 20°-30°.

2.2.7.5 Blade aspect ratio

After setting the values for ψ, φ, and R at the design condition, the number of stages for a multi-stage compressor can be determined. For a given mass-flow and blade speed, the mean radius of the compressor and the blade heights can also be calculated. The total compressor axial length and the number of blades can then be estimated by choosing suitable aspect ratio values, H/l, for each blade row.

The choice of aspect ratios is important as it influences both the blade losses and the stability margin. Lowering the aspect ratios, the losses will increase due to augmented wetted area and the growth of boundary layers. Nevertheless, as shown by Koch [22], lower aspect ratios can guarantee a higher surge margin. This is the reason why modern multi-stage compressors have generally low aspect ratios, typically in the range [1:2].

Once chosen the aspect ratio and the blade height, the chord (l) can be determined. The pitch-to-chord ratio, s/l, can be computed from equation (4) combined with a proper choice of the diffusion factor. The number of blades can be derived from the pitch-to-chord ratio and the chord.

Finally, the total compressor length depends on the axial gaps between blade rows. These values are normally set in order to limit the vibration and noise generated by rotor-stator interaction. Generally, spaces between the rows of about half an axial chord are adopted.

2.2.8 Stage matching

Every compressor is designed for a particular operating condition, the one referred to as design point. This condition is normally the one where the compressor will operate for most of the time and is generally near to the maximum speed and pressure rise that the machine can deliver. Nevertheless, it is also important to have adequate values for efficiency and pressure ratio at other conditions as, for example, low speed operating during the start-up. The problem of matching the inlet flow requirements of each stage to the outlet flow of the upstream one is general to all multi-stage compressors. The design point is the combination of non-dimensional speed and mass-flow $\dot{m}$ at which the inlet flow at each stage corresponds to its optimum. Difficulties may arise when the compressor operates at different speed and/or mass-flow, i.e. on a different working line. Even if the flow is usually expressed in terms of mass-flow, the requirement of a stage is best thought in terms of volume flow rate. This because the inlet flow angle is the key parameter to determine whether a blade row is operating correctly or not, and the angle depends on the ratio of flow velocity to rotational speed. It is the volume flow which fixes the flow velocity. Therefore, the flow coefficient ϕ can be used as a proper dimensionless group. As shown in [23], for a constant corrected blade speed $U/\sqrt{c_p T_0}$, there is a proportionality relationship between the flow coefficient and the flow function F, given by:

$$F = \frac{\dot{m}\sqrt{c_p T_0}}{A p_0} \tag{29}$$

In the previous expression, A is the compressor cross-sectional area.

Considering the design point, the blading and the cross-sectional area will have been chosen for each stage to be appropriate for the design mass-flow and rotational speed. The density rise is likely to be significant. To compensate for this and to avoid a too low axial velocity, the cross-sectional area must decrease in the downstream direction.

Every compressor during his life cycle will operate at least some of the time at pressure ratios or speeds different from the design value. The greatest difficulty arising in these cases is the fact that an excursion in the flow function at inlet of a stage generally leads to a larger excursion at outlet. This because the pressure ratio $PR = p_{02}/p_{01}$ depends strongly on the flow function and for unstalled blades increases rapidly as the flow is reduced. The temperature ratio T_{02}/T_{01} also rises when reducing the flow function and can be expressed as follows:

$$\frac{T_{02}}{T_{01}} = PR^{\frac{\gamma-1}{\gamma\eta_p}} \approx PR^{0.3} \tag{30}$$

The latter approximation is valid for a reasonably high efficiency compressor. Therefore, the ratio of inlet to outlet flow functions can be approximated as:

$$\frac{F_2}{F_1} \approx PR^{-0.85} \approx PR^{-1} \tag{31}$$

Considering, for example, a 1% reduction of the inlet flow function of a stage, the pressure ratio will increase and the outlet flow function will decrease by more than 1%. Similarly, an increase in the inlet flow function of the stage will produce a larger increase in the outlet flow function. Hence, the volume flow rate

is amplified through the stages, the magnitude of the amplification rising with the pressure ratio.

The effect of mismatching is really large in multi-stage compressors because of their multiplicative nature; the overall pressure ratio can be written as:

$$PR_{overall} = PR_1 PR_2 \ldots PR_n \tag{32}$$

Where $PR_1$is the pressure ratio of the first stage and so on. The effect is diagrammatically reported in Figure 2.5, in which the overall pressure ratio/mass-flow characteristic is shown together with the characteristics for the first and last stage. Point a represents the design condition, point b refers to a reduced pressure rise at design speed and point c relates to an increased pressure rise at the same speed. For point a, the position is the same on the first and last stage characteristics. For the increased mass-flow condition, point b, the stages produce a smaller pressure rise and therefore smaller density rise than the design one. The situation gets progressively worse through the compressor until the last stage, where the operating condition is far away from the design point. It is possible that the pressure ratios in the rear stages decrease to a value lower than unity. The last stage acts in this case as a throttle and the phenomenon is often referred to as apparent choking. This apparent chocking is severe negative incidence stall.

Just as a reduction in the stage pressure rise from the design value leads to a chocking of the rear stages, an increase in the pressure rise at the design speed leads to their stalling. Point c shows this latter case. The choking or stalling of the rear stage (or stages) puts a limit on the flow function range for all the compressor.

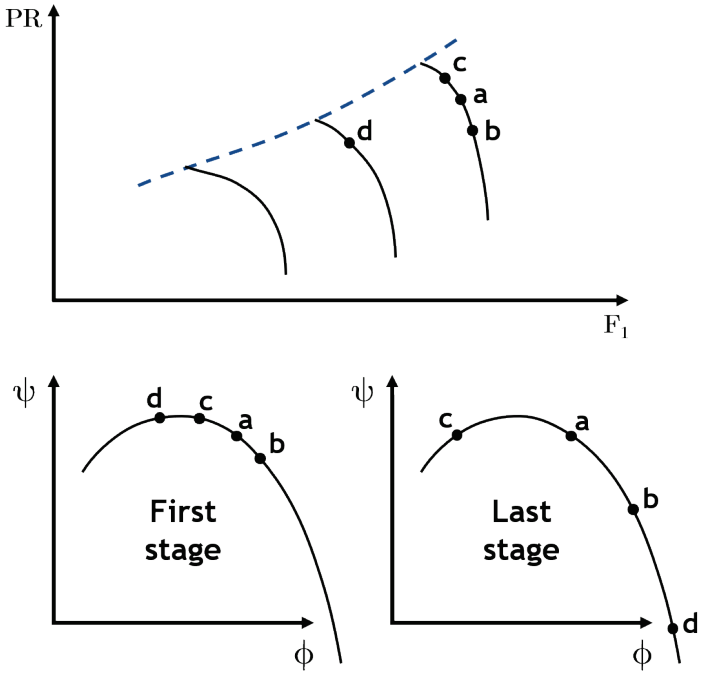

Figure 2.5 Overall pressure ratio/mass-flow characteristic and characteristic curves for the first and last stage

Finally, point d shows the effect of a significant reduction in the rotational speed. This reduction is reflected in the fact that the density rise is reduced below the design value. The mass-flow is hence limited by the rear stage, which is choked. This means that the mass-flow into the front stages is much lower than the design value, making them subjected to stall.

3 Computational Framework

This chapter is aimed to introduce the numerical setup that has been used for the computations presented within this work. The first section contains the main characteristics of the CFD code TRAF, developed by the research group led by Prof. Andrea Arnone starting from the end of the 1980s. The second section focuses on the non-reflecting mixing plane model that has been improved and extended to the real gas version of the code.

3.1 TRAF

The CFD code that has been used for all the numerical simulations whose result are presented in the following chapters is the TRAF code. The code started to be developed in 1988 in the framework of a joint research project between the University of Florence and NASA (ICASE and ICOMP), focused on viscous cascade flow analysis.

3.1.1 Governing equations

The 3D-unsteady Navier-Stokes equations are averaged adopting the Reynolds approach (RANS). For each blade passage, rotating at constant angular speed Ω (zero for stationary blade rows), the Reynolds averaged Navier-Stokes equations in conservative form are expressed with respect to a curvilinear coordinate system ξ, η, ζ. The link between the Cartesian coordinate system and the curvilinear one is handled by means of transformation matrices and Jacobian.

The molecular viscosity μ is determined as a function of temperature through the following power law:

$$\frac{\mu}{\mu_0} = \left(\frac{T}{T_0}\right)^{\alpha} \tag{33}$$

Where μ_0, T_0 and α are gas-dependent reference parameters. The eddy-viscosity hypothesis is used to take into account for turbulence effects. Following the above-mentioned hypothesis, the molecular viscosity and thermal conductivity are expressed as:

$$\mu = \mu_l + \mu_t \tag{34}$$

$$k = c_p \left[\left(\frac{\mu}{Pr}\right)_l + \left(\frac{\mu}{Pr}\right)_t\right] \tag{35}$$

where c_p is the specific heat at constant pressure, Pr is the Prandtl number and the subscripts l and t refer to laminar and turbulent, respectively.

3.1.2 Turbulence closures

Several turbulence closures have been implemented in the TRAF code, ranging from algebraic to more complex one- and two-equation models. A complete list of the turbulence models available is the following:

- Baldwin-Lomax algebraic model [24]
- Baldwin-Lomax algebraic model with Degani-Schiff correction [25]
- Mixing length algebraic model [26]
- One-equation Spalart-Allmaras model [27]
- One-equation Spalart-Allmaras model with Spalart-Shur correction [28]
- Two-equation k-ω Wilcox Low-Reynolds model [29]
- Two-equation k-ω Wilcox High-Reynolds model 1988 ver. [29]

- Two-equation k-ω Menter SST model [30]
- Two-equation k-ω Wilcox High-Reynolds model 2006 ver. [31]

3.1.3 Spatial discretization

As far as the spatial discretization is concerned, the code is based on a finite-volume approach, with the governing equations discretized in space starting from an integral formulation and without any intermediate mapping [32] [33] [34]. All the viscous terms are discretized using 2nd order accurate central differences, while for the inviscid fluxes two different options are available:

- 2nd order cell-centered scheme
- Roe's upwind scheme

For the cell-centered scheme, on each cell face, the fluxes are calculated after computing the necessary flow quantities at the face center. Those quantities are obtained by a simple averaging of adjacent cell-center values of the dependent variables. To assure stability and prevent oscillations near shocks or stagnation points, artificial dissipation terms are also included away from the shear layer regions, where the physical diffusion associated with diffusive terms is generally not sufficient to prevent the possible odd-even point decoupling typical of centered schemes. Both scalar [32] and matrix [35] dissipation models are available in the code. To minimize the amount of artificial diffusion inside the shear layers, these terms are weighed with an eigenvalue scaling [36] [37].

As far as the upwind option is concerned [38], a higher order of spatial accuracy is achieved through a MUSCL (Monotone Upstream-centered Schemes for Conservation Laws) extrapolation

scheme (3^{rd} order spatial discretization). To avoid numerical instabilities, a TVD (Total Variation Diminishing) scheme is applied [39].

3.1.4 Time-stepping scheme

In the TRAF code, the system of differential equations is advanced in time using an explicit four-stage Runge-Kutta scheme [32]. In order to reduce the computational cost, a hybrid version of the scheme is implemented. In particular, the viscous terms are evaluated only at the first stage and then left unchanged for the remaining stages of the method. By performing two evaluations of the artificial dissipating terms at the first and at the second stage, good high-frequency damping properties have been obtained. These damping properties are particularly important for the multigrid process, which will be introduced later in this section.

For the case of time accurate calculations, a dual-time stepping method [40] [41] is adopted and the coupling between consecutive rows is handled by means of sliding interface planes.

3.1.5 Acceleration techniques

To strongly reduce the computational cost and to speed up the convergence of the code, four different techniques have been adopted [42]. They are briefly described in the following subsections.

3.1.5.1 Local time-stepping

While adopting the time-marching approach, a faster expulsion of disturbances can be attained by locally using the maximum available time step. In particular, the local time step limit is computed accounting for both the convective (Δt_c) and diffusive (Δt_d) contributions:

$$\Delta t = CFL \left(\frac{\Delta t_c \, \Delta t_d}{\Delta t_c + \Delta t_d} \right) \tag{36}$$

In the previous expression, *CFL* is a constant usually referred to as Courant-Friedrichs-Lewy number.

3.1.5.2 Residual smoothing

To extend the stability limit and the robustness of the basic scheme, an implicit smoothing of residuals is adopted in the code. This technique, first introduced by Lerat [43] in conjunction with Lax-Wendroff type schemes, was later implemented by Jameson [44] on the Runge-Kutta stepping scheme. For viscous calculations on highly-stretched meshes, the variable coefficient formulations of Martinelli and Jameson [36] and Swanson and Turkel [37] have proven to be robust and reliable.

3.1.5.3 Multigrid

This convergence accelerating method was developed in the 1970s for the solution of elliptic problems [45]. At the beginning of the following decade, Ni [33] and Jameson [44] applied the multigrid method to the Euler equations. The idea on which the method is based is to introduce a series of coarser grids obtained by the fine one simply eliminating every other mesh line in each coordinate direction; these coarser meshes are used to speed up the propagation of the fine grid corrections, leading to a faster expulsion of disturbances. The procedure is repeated on a succession of coarser grids and the corrections computed on each coarse grid are transferred back to the finer one by bilinear interpolations. Even if more grid levels can be adopted, usually the multigrid method is performed with a V-cycle on three grids: coarse ($4h$), medium ($2h$) and fine (h).

3.1.5.4 Grid refinement

A grid refinement strategy is introduced in the code to provide a cost-effective initialization of the fine grid solution. Adopting this methodology together with multigrid leads to the so called Full Multigrid (FMG) procedure. The solution is initialized on the coarser grid level and iterated for a prescribed number of multigrid cycles. The solution is then passed, by bilinear interpolations, onto the next finer grid and the process is repeated until the finest grid level is reached.

3.1.6 Boundary conditions

In typical turbomachinery configurations there are five main types of boundaries: inlet, outlet, solid walls, periodicity and interface between adjacent rows. The radial distributions of total temperature, total pressure and flow angles are prescribed at the computational domain inlet, while the outgoing Riemann invariant is taken from the interior. On the domain outlet section, the static pressure is enforced through a spanwise distribution or a value at the casing used to impose a radial equilibrium boundary condition, while density and momentum components are extrapolated. On the solid walls within the computational domain, the pressure is extrapolated from the interior grid nodes and no-slip and temperature conditions are used to compute the values for density and total energy. Two different temperature conditions are currently available in the code: adiabatic wall and prescribed constant wall temperature. In the former case, the adiabatic condition is obtained by nullifying the wall temperature gradient in the normal-like direction, while in the latter case the constant wall temperature is prescribed by the user as a fraction of the total temperature at the domain inlet section. As the code has been implemented adopting one phantom-cell layer for each grid boundary, the periodicity in circumferential direction form a blade passage to the contiguous one is

imposed by setting periodic phantom cell values. If the grid lines do not match at the periodicity interface, linear interpolations are performed in order to set a reasonable value for the dependent variables in phantom cells. Despite the fact that this approach cannot guarantee a complete conservation of mass, momentum and energy, in most of the applications no accuracy losses have been experienced, if no strong gradients occur along non-periodic grid boundaries with high differences in cell sizes. As far as boundary conditions for the interfaces between adjacent rows are concerned, a different treatment is adopted for the time-accurate and the steady-state case. When running an unsteady analysis, the coupling between consecutive rows is handled by means of sliding interface planes, with the exchange of information between adjacent blocks obtained performing linear interpolations in both the tangential and the radial direction. Conversely, for steady simulations, mixing-planes are introduced to handle the coupling between adjacent rows. Data exchange through the common interface plane of consecutive rows is obtained by an appropriate calculation of phantom cell values, keeping the spanwise distribution while averaging in the pitchwise direction. A deeper overview of the mixing plane models available in the code will be presented further in section 3.2.

3.1.7 Code parallelization

In order to properly exploit the computational power available nowadays in multi-core work stations, clusters and high performance computing platforms, the TRAF code has been parallelized following a multi-level hybrid strategy [46]. This hybrid scheme is obtained from the coupling of OpenMP and MPI parallelism, that can also be used independently on user's request. The shared memory standard OpenMP is an implementation of multithreading, a method of parallelization in which the master thread (a series of instructions executed consecutively) forks a

specified number of slave threads and a task is divided among them. The threads then run concurrently, with the runtime environment allocating threads to different processors. The code has two levels of OpenMP parallelism: the first one involves computational blocks (blade passages), while the second level is nested and related to the spanwise direction of computational blocks. The Message Passing Interface (MPI) standard instead has been adopted to handle communications for distributed memory systems. Splitting the computation among different nodes, MPI parallelization offers the possibility to handle very-large domains whose memory requirements exceed the resources available on one node.

3.1.8 Real gas version

Two different gas models are implemented in the TRAF code: the perfect and the real gas one. The real gas version [47] of the code was developed following these key targets: simple implementation, limited additional computational cost with respect to the perfect gas version, a level of accuracy suitable for industrial standards and capability of dealing with any kind of gas.

The behavior of real gases, gas mixtures or steam is reproduced by replacing the perfect gas analytic relationships with the local interpolation of gas data from property tables. In order to reduce the computational cost, the gas tables are external to the flow solver and must be generated before running the code, using commercial or in-house developed databases. This method can be applied to any working fluid and extends property evaluations into saturated and superheated regions. The main restriction is given by the assumption that only one working fluid is present in the computational domain.

3.1.9 Computational grids

The code was originally able to handle H- or C-type structured grids but has been extended to O-type grid topology in 2009. The computational grids are obtained using in-house developed tools by stacking in the spanwise direction 2D grids generated through a process based on an elliptic procedure that solves the discretized Poisson equations using a point relaxation scheme. Forcing functions like the one proposed by Steger and Sorenson [48] are used to control the grid spacing and orientation at the wall. Viscous grids are obtained from the inviscid grids by adding lines near the wall.

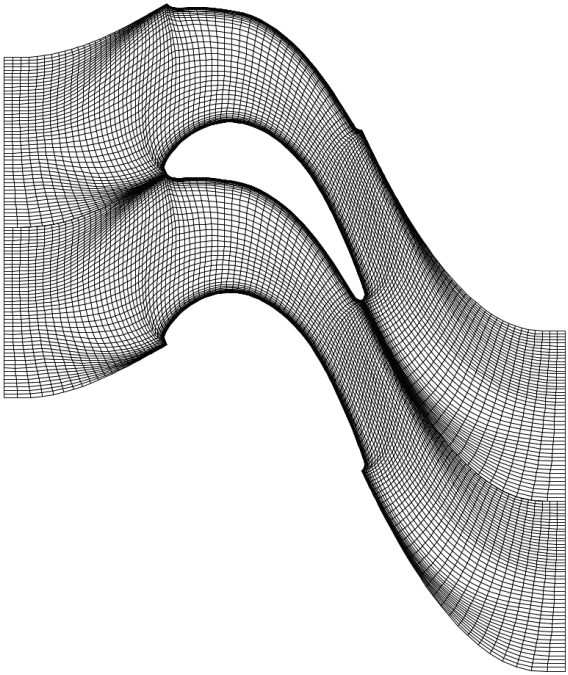

Figure 3.1 Blade-to-blade H-type grid

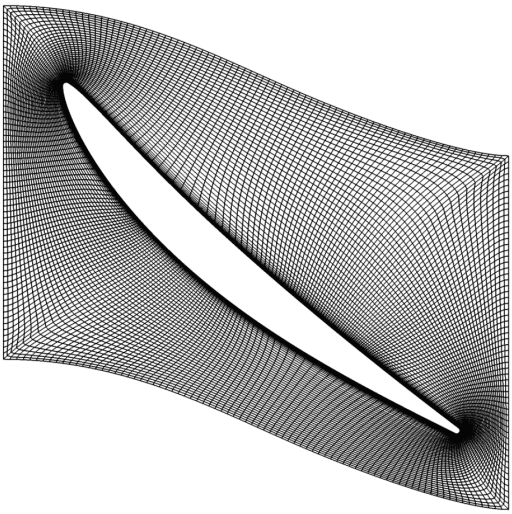

Figure 3.2 Blade-to-blade O-type grid

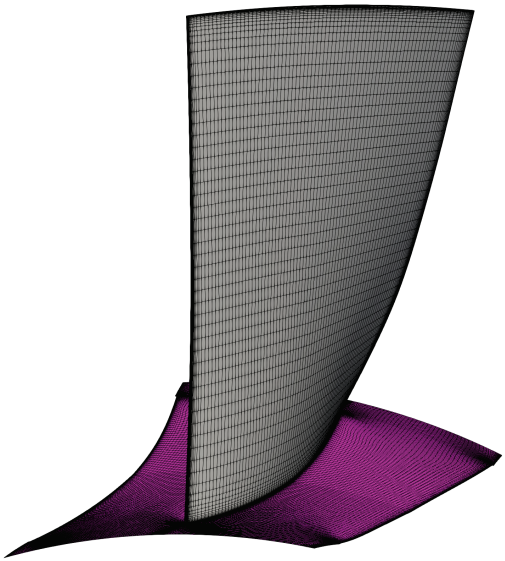

Figure 3.3 H-type 3D mesh of an axial compressor blade

For standard viscous full Navier-Stokes simulations, the grid spacing is chosen to obtain a y^+ value lower than 2 for the first grid point above the wall. This condition allows a proper resolution of the laminar sub-layer of all the boundary layers located in the computational domain due to the presence of solid walls.

Some examples of H- and O-type blade-to-blade grids are shown in Figure 3.1 and Figure 3.2, respectively. A 3D H-type mesh of one the front stages of an axial compressor, obtained by stacking in the spanwise direction different blade-to-blade grids, is then represented in Figure 3.3.

3.2 Non-reflecting mixing plane model

As already introduced in section 3.1.6, in the case of multi-row steady-state computations, mixing-planes are introduced to handle the coupling between adjacent rows. Data exchange through the common interface plane of consecutive rows is obtained by an appropriate calculation of phantom cell values, keeping the spanwise distribution while averaging in the pitchwise direction.

Two main mixing plane models are available in the TRAF code: a robust reflecting model and a more accurate non-reflecting one. In the former, the boundary conditions imposed in each phantom cell on one side of the interface are obtained by averaging in the pitchwise direction the values of the governing conservative variables of the grid cells at the same span on the other interface side; if the adjacent grids do not match in spanwise direction (e. g. different number of cells or nodes distribution), an interpolation of the pitchwise averaged values is performed. Robustness and capability of handling flow reversals across the interface are the main positive aspects of this mixing plane

model, both making it attractive for industrial design purposes. By imposing as boundary condition a constant value for the conservative governing variables for all the grid cells at the same span, reflections of the main quantities of interest arise next to the interface. In some particularly demanding cases, as transonic compressor rows with a shock system which reaches the interface or machines with small inter-row axial gaps, the effects of reflections are enhanced.

To avoid non-physical reflections next to the mixing planes of the computational domain, a non-reflecting model, based on the 2D theory developed by Giles [49] [50] and extended to the 3D case by Saxer [51], has been implemented in the TRAF code. A perfect gas version of this model was first introduced in the code in the early 2000s, but due to some fluxes-conservation issues, his application to the case of multi-stage axial compressors was strongly limited. Indeed, the need for good mass-flow conservation properties is particularly important for compressors with a high stage count, in which even a relatively low error at each interface can lead to unacceptable mass-flow evaluations in the rear part of the machine. This can result in a wrong stage matching and overall performance prediction.

In 2016, to overcome these restrictions, a deep revision of the model has been carried out. The non-reflecting model has hence been renewed paying particular attention to mass-flow and total temperature conservation across the interface; for other quantities, such as total pressure and entropy, the non-conservation through the mixing plane is due to the mixing process itself and cannot be avoided. The model has also been extended to the real gas case, making it ready to be used as a standard for the full compressor steady-state analysis.

3.2.1 Perfect gas version

The task of each non-reflecting model is to allow the positioning of a far-field boundary close to a blade row without affecting the flow field in the vicinity of the blades. This is a key aspect when dealing with multi-row steady-state analyses characterized by a relatively low axial spacing between adjacent rows.

The approach used to develop the steady non-reflecting boundary condition model is based on a characteristic analysis of the linearized Euler equations [49]. At every inlet and outlet interface of the computational domain, there are some incoming and outgoing modes. While the outgoing characteristic values are extrapolated from the inner-domain, the average changes in all the incoming characteristics are set in order to target some user-specified mean quantities. The remaining changes (e. g. the circumferential harmonics of the incoming characteristics), are determined applying the non-reflecting boundary condition theory from the amplitudes of corresponding harmonics of the outgoing characteristics.

The basic idea is that, in the steady steady-state approximation, the flow at each boundary for a certain span can be assumed as periodic in the pitchwise direction. A Fourier decomposition of this periodic flow can be performed, leading to an average value and circumferential components. Hence, the 0^{th} Fourier mode represent the circumferential average of the flow and can be treated according to the standard 1D [52] procedure. The remaining part coming from the decomposition, that is represented by the sum of the harmonics, is treated according to Giles' 2D non-reflecting boundary condition theory [49]. Considering the 3D case, this is the part of the method that uncouples the tangential and the radial flow variation. As it considers

every radial flow variation only from an average point of view, the method is called quasi-3D.

3.2.1.1 Average flow definitions

In order to ease and reduce the computational effort required to enforce the non-reflecting boundary conditions, for each span, the solution is interpolated on a node distribution that is equally spaced in the circumferential direction, for both inlet and outlet boundaries. The average values of a generic flow quantity φ are, for this simplified case:

$$\overline{\varphi} = \frac{1}{N}\sum_{j}\varphi_j \tag{37}$$

Where N is the number of equally spaced nodes at the boundary, including only once the periodic grid node.

When dealing with stator/rotor interaction steady simulations, averaged data are transferred from one row to the other and vice versa. Between the many possible averaging procedures, the only rigorous one is based on the 'mixed-out' flow-field. Assuming that sufficiently far upstream or downstream the flow is uniform, then the flux $\boldsymbol{F}$ based on these uniform conditions, specified from now on with the subscript $_F$, must be equal to the average flux $\bar{\boldsymbol{F}}$ at the considered boundary. Differently from the simplified fluxes definition used by Saxer [51] in its 3D extension of Giles' method, the one that has been implemented in the TRAF code is the following:

$$\bar{F}_1 = \overline{\rho v_n} = \rho_F \boldsymbol{V}_F \cdot \boldsymbol{n} \tag{38}$$

$$\bar{\boldsymbol{F}}_{234} = \overline{\rho v_n \boldsymbol{V}} + \bar{p}\boldsymbol{n} = \rho_F(\boldsymbol{V}_F \cdot \boldsymbol{n})\boldsymbol{V}_F + p_F\boldsymbol{n} \tag{39}$$

$$\bar{F}_5 = \overline{\rho v_n H} = \left(\frac{\gamma}{\gamma - 1} p_F + \frac{1}{2}\rho_F V_F^2\right)(\boldsymbol{V}_F \cdot \boldsymbol{n}) \tag{40}$$

The vector $\bar{\boldsymbol{F}}_{234}$ is introduced to store the average fluxes ($\bar{F}_2$ $\bar{F}_3$ $\bar{F}_4$), while $\boldsymbol{V}$ and $\boldsymbol{V}_F$ are the local and 'mixed-out' velocity vectors. The vector $\boldsymbol{n}$ is, for a generic infinitesimal spanwise band of width *ds* on the interface, the normal unity vector. In the previous expressions, the velocity components and the total enthalpy are quantities referring to the relative frame of reference, so that they can apply to both rotor and stator rows.

Solving the system of equations (38) (39) (40), it is possible to obtain the "mixed-out" values for the primitive variables:

$$p_F = \frac{\bar{\boldsymbol{F}}_{234} \cdot \boldsymbol{n} + \sqrt{(\bar{\boldsymbol{F}}_{234} \cdot \boldsymbol{n})^2 + (\gamma^2 - 1)(\bar{F}_{234}^2 - 2\bar{F}_1 \bar{F}_5)}}{\gamma - 1} \tag{41}$$

$$\boldsymbol{V}_F = \frac{\bar{\boldsymbol{F}}_{234} - p_F \boldsymbol{n}}{\bar{F}_1} \tag{42}$$

$$\rho_F = \frac{\bar{F}_1}{\boldsymbol{V}_F \cdot \boldsymbol{n}} \tag{43}$$

The mixing process characterizing this averaging procedure leads to higher viscous losses and to a flow with a higher entropy level, as discussed in [53].

3.2.1.2 Characteristic variables

The characteristic variables are defined in terms of perturbations with respect to the average inlet or outlet flow-field. The 1D characteristic variables are connected to the perturbations of the primitive variables by the following relations [54]:

$$\begin{pmatrix}\phi_1\\ \phi_2\\ \phi_3\\ \phi_4\\ \phi_5\end{pmatrix} = \begin{pmatrix}-\bar{c}^2 & 0 & 0 & 0 & 1\\ 0 & 0 & \bar{\rho}\bar{c} & 0 & 0\\ 0 & 0 & 0 & \bar{\rho}\bar{c} & 0\\ 0 & \bar{\rho}\bar{c} & 0 & 0 & 1\\ 0 & -\bar{\rho}\bar{c} & 0 & 0 & 1\end{pmatrix} \boldsymbol{U}_p \tag{44}$$

$$\boldsymbol{U}_p = \begin{pmatrix} -\frac{1}{\bar{c}^2} & 0 & 0 & \frac{1}{2\bar{c}^2} & \frac{1}{2\bar{c}^2}\\ 0 & 0 & 0 & \frac{1}{2\bar{\rho}\bar{c}} & -\frac{1}{2\bar{\rho}\bar{c}}\\ 0 & \frac{1}{\bar{\rho}\bar{c}} & 0 & 0 & 0\\ 0 & 0 & \frac{1}{\bar{\rho}\bar{c}} & 0 & 0\\ 0 & 0 & 0 & \frac{1}{2} & \frac{1}{2}\end{pmatrix} \begin{pmatrix}\phi_1\\ \phi_2\\ \phi_3\\ \phi_4\\ \phi_5\end{pmatrix} \tag{45}$$

where:

$$\boldsymbol{U}_p = \begin{pmatrix}\rho-\bar{\rho}\\ u-\bar{u}\\ v-\bar{v}\\ w-\bar{w}\\ p-\bar{p}\end{pmatrix} = \begin{pmatrix}\tilde{\rho}\\ \tilde{u}\\ \tilde{v}\\ \tilde{w}\\ \tilde{p}\end{pmatrix} \tag{46}$$

The first characteristic variable is the linearized entropy perturbation, the second and third are the tangential and the spanwise velocity at the boundary and are related to vorticity, while the last two variables are the downstream and the upstream running pressure waves (assuming that the axial Mach number is subsonic). At the inflow boundary, the first four characteristics are incoming and hence must be specified. The fifth is outgoing and so it must be extrapolated from the inner domain. At the outlet boundary, the situation is the opposite and only the fifth characteristic variable must be set.

3.2.1.3 Fourier analysis

The way of handling the boundary conditions is approached by assuming that, in the area close to inlet, outlet and inter-row interfaces the flow is governed by the linearized Euler equations. These equations, written in primitive form and considering just 2D steady-state variations for a certain span, assume the following expression:

$$\bar{A}\frac{\partial \boldsymbol{U}_p}{\partial x} + \overline{B}\frac{\partial \boldsymbol{U}_p}{\partial y} = 0 \tag{47}$$

with:

$$\bar{A} = \begin{pmatrix} \bar{u} & \bar{\rho} & 0 & 0 & 0 \\ 0 & \bar{u} & 0 & 0 & \frac{1}{\bar{\rho}} \\ 0 & 0 & \bar{u} & 0 & 0 \\ 0 & 0 & 0 & \bar{u} & 0 \\ 0 & \gamma\bar{p} & 0 & 0 & \bar{u} \end{pmatrix} \tag{48}$$

$$\overline{B} = \begin{pmatrix} \bar{v} & \bar{\rho} & 0 & 0 & 0 \\ 0 & \bar{v} & 0 & 0 & 0 \\ 0 & 0 & \bar{v} & 0 & \frac{1}{\bar{\rho}} \\ 0 & 0 & 0 & \bar{v} & 0 \\ 0 & 0 & \gamma\bar{p} & 0 & \bar{v} \end{pmatrix} \tag{49}$$

The vector $\boldsymbol{U}_p$ contains the perturbations of the primitive variables from a uniform flow, while both the matrices $\bar{A}$ and $\overline{B}$ are evaluated using the same uniform flow conditions. A Fourier analysis of the flow considers wave-like solutions given by a scalar wave function multiplying a constant column vector:

$$\boldsymbol{U}_p(x, y) = e^{i(kx+ly)}\boldsymbol{u}^R \tag{50}$$

Introducing this solution in the differential equation gives:

$$\left(k\bar{A} + l\overline{B}\right)\boldsymbol{u}^R = 0 \tag{51}$$

The solution is non-trivial in the case:

$$det\left(k\bar{A} + l\overline{B}\right) = 0 \tag{52}$$

The previous expression leads to a polynomial 5^{th} degree equation in both k and l:

$$(\bar{u}k + \bar{v}l)^3((\bar{u}k + \bar{v}l)^2 - \bar{c}^2(k^2 + l^2)) = 0 \tag{53}$$

Considering a given value for l, the k_n roots are:

$$k_{1,2,3} = -\frac{\bar{v}l}{\bar{u}} \tag{54}$$

$$k_4 = \frac{\bar{u}\bar{v}l + \bar{c}\beta l}{\bar{c}^2 - \bar{u}^2} \tag{55}$$

$$k_5 = \frac{\bar{u}\bar{v}l - \bar{c}\beta l}{\bar{c}^2 - \bar{u}^2} \tag{56}$$

where:

$$\beta = \begin{cases} i\ sign(l)\sqrt{\bar{c}^2 - (\bar{u}^2 + \bar{v}^2)}, & \bar{u}^2 + \bar{v}^2 < \bar{c}^2 \\ -sign(\bar{v})\sqrt{(\bar{u}^2 + \bar{v}^2) - \bar{c}^2}, & \bar{u}^2 + \bar{v}^2 \geq \bar{c}^2 \end{cases} \tag{57}$$

It is worth to notice that, for supersonic flow, the parameter β does not depend on l, reflecting the different behavior in terms of perturbation propagation in subsonic and supersonic flow. In the former, the perturbation decays exponentially while, in the latter, it propagates indefinitely.

Once obtained the eigenvalues, it is possible to determine the corresponding left and right eigenvectors, needed in the construction of the non-reflecting boundary conditions.

The column vector $\boldsymbol{u}^R$ is a right eigenvector of the matrix $l\bar{A}^{-1}\overline{B}$, with eigenvalue $-k$, if:

$$\left(kI + l\bar{A}^{-1}\overline{B}\right)\boldsymbol{u}^R = \bar{A}^{-1}\left(k\bar{A} + l\overline{B}\right)\boldsymbol{u}^R = 0 \qquad (58)$$

Instead, the row vector $\boldsymbol{v}^L$ is a left eigenvector of the matrix $l\bar{A}^{-1}\overline{B}$, with eigenvalue $-k$, if:

$$\boldsymbol{v}^L\bar{A}^{-1}\left(k\bar{A} + l\overline{B}\right) = 0 \qquad (59)$$

An important feature of the left null-vector $\boldsymbol{v}^L$, that will be used in the non-reflecting method, is its orthogonality to $\boldsymbol{u}^R$. After some algebra, the left and right eigenvectors for the five roots k_n are the following:

- $k_1 = -\bar{v}l/\bar{u}$:

$$\boldsymbol{v}_1^L = \begin{pmatrix} -\bar{c}^2 & 0 & 0 & 0 & 1 \end{pmatrix} \qquad (60)$$

$$\boldsymbol{u}_1^R = \begin{pmatrix} -1/\bar{c}^2 \\ 0 \\ 0 \\ 0 \\ 0 \end{pmatrix} \qquad (61)$$

These eigenvalue and eigenvectors refer to an entropy wave. This can be verified by the fact that only the term related to density is different from zero in the right eigenvector, hence the wave is characterized by varying entropy, no vorticity and constant pressure. Also the left eigenvector is connected to entropy, as $\boldsymbol{v}_1^L \boldsymbol{U}_p$ is equal to the linearized entropy $\tilde{p} - \bar{c}^2 \tilde{\rho}$.

- $k_2 = -\bar{v}l/\bar{u}$:

$$\boldsymbol{v}_2^L = \bar{\rho}\bar{c} \begin{pmatrix} 0 & -\bar{u} & -\bar{v} & 0 & -1/\bar{\rho} \end{pmatrix} \tag{62}$$

$$\boldsymbol{u}_2^R = \frac{1}{\bar{\rho}\bar{c}} \begin{pmatrix} 0 \\ -\bar{u}^2/\bar{v}^2 \\ -1/\bar{v} \\ 0 \\ 0 \end{pmatrix} \tag{63}$$

This root is associated with a vorticity wave, as the right eigenvector gives a wave with vorticity, but uniform entropy and pressure.

- $k_3 = -\bar{v}l/\bar{u}$:

$$\boldsymbol{v}_3^L = \bar{\rho}\bar{c}(0 \quad 0 \quad 0 \quad -\bar{v} \quad 0) \tag{64}$$

$$\boldsymbol{u}_3^R = \frac{1}{\bar{\rho}\bar{c}} \begin{pmatrix} 0 \\ 0 \\ 0 \\ -1/\bar{v} \\ 0 \end{pmatrix} \tag{65}$$

As for the previous root, also in this case this eigenvalue and these eigenvectors refer to a vorticity wave. Since the first three eigenvalues have the save numerical value, the orthogonality of the corresponding eigenvectors must be verified. This can be easily done by checking that:

$$\boldsymbol{v}_n^L \boldsymbol{u}_m^R = 0, \qquad n,m = 1,2,3, \qquad n \neq m \tag{66}$$

- $k_4 = \frac{\bar{u}\bar{v}l + \bar{c}\beta l}{\bar{c}^2 - \bar{u}^2}$:

$$\boldsymbol{v}_4^L = \bar{\rho}\bar{c}\begin{pmatrix} 0 & -\bar{v} & \bar{u} & 0 & \beta/\bar{\rho} \end{pmatrix} \tag{67}$$

$$\boldsymbol{u}_4^R = \frac{1}{2\bar{\rho}\bar{c}(\bar{c}-\bar{u})}\begin{pmatrix} -\frac{\bar{\rho}}{\bar{c}}(\bar{c}\bar{v} + \beta\bar{u}) \\ \beta\bar{c} + \bar{u}\bar{v} \\ \bar{c}^2 - \bar{u}^2 \\ 0 \\ -\bar{\rho}\bar{c}(\bar{c}\bar{v} + \beta\bar{u}) \end{pmatrix} \tag{68}$$

This root relates to an isentropic, irrotational pressure wave, propagating downstream if the flow is axially subsonic ($\bar{u} < \bar{c}$).

- $k_5 = \frac{\bar{u}\bar{v}l - \bar{c}\beta l}{\bar{c}^2 - \bar{u}^2}$:

$$\boldsymbol{v}_5^L = \bar{\rho}\bar{c}\begin{pmatrix} 0 & \bar{v} & -\bar{u} & 0 & \beta/\bar{\rho}\bar{c} \end{pmatrix} \tag{69}$$

$$\boldsymbol{u}_5^R = \frac{1}{2\bar{\rho}\bar{c}(\bar{c}+\bar{u})} \begin{pmatrix} -\frac{\bar{\rho}}{\bar{c}}(\bar{c}\bar{v} - \beta\bar{u}) \\ -\beta\bar{c} + \bar{u}\bar{v} \\ \bar{c}^2 - \bar{u}^2 \\ 0 \\ -\bar{\rho}\bar{c}(\bar{c}\bar{v} - \beta\bar{u}) \end{pmatrix} \tag{70}$$

This root corresponds to an isentropic, irrotational pressure wave, propagating upstream if the flow is axially subsonic ($\bar{u} < \bar{c}$).

3.2.1.4 Quasi-3D steady NRBC

Considering the inlet or the outlet boundary of the blade-to-blade section of a linear cascade and a particular choice of l, the most general form of the perturbation $\boldsymbol{U}_p$ is:

$$\boldsymbol{U}_p(x,y) = \left[\sum_{n=1}^{5} a_n \boldsymbol{u}_n^R e^{ik_n x}\right] e^{ily} \tag{71}$$

where k_n is the n^{th} root obtained from the previously introduced Fourier analysis and $\boldsymbol{u}_n^R$ is the corresponding right eigenvector. The ideal non-reflecting boundary condition formulation would be to enforce $a_n = 0$ for each n referring to an incoming wave. Exploiting the orthogonality of eigenvectors, and multiplying both sides of the equation (71) for the left eigenvector $\boldsymbol{v}_n^L$ gives:

$$\boldsymbol{v}_n^L \boldsymbol{U}_p = a_n (\boldsymbol{v}_n^L \boldsymbol{u}_n^R) e^{ik_n x} e^{ily} \tag{72}$$

Hence, an equivalent non-reflecting boundary conditions specification is:

$$\boldsymbol{v}_n^L \boldsymbol{U}_p = 0 \tag{73}$$

For each value of n associated to an incoming mode (e. g. n=1, 2, 3, 4 for an inlet boundary and n=5 at the outflow). The right

and left eigenvectors already introduced do have a physical meaning: the former shows the primitive variables variation caused by the corresponding wave mode, while the latter is related to the amplitude of a particular wave component when applied to the general solution.

The conditions already introduced can be easily extended to the more general three-dimensional case by considering the boundary at $x = 0$ of a 3D linear cascade, with pitch P in the y direction. The perturbation $\boldsymbol{U}_p$ can be written as:

$$\boldsymbol{U}_p(0, y, z) = \overline{\boldsymbol{U}}_p(z) + \sum_{-\infty, m \neq 0}^{\infty} \widehat{\boldsymbol{U}}_{p_m}(z) e^{i l_m y} \tag{74}$$

in which $\overline{\boldsymbol{U}}_p(z)$ is the pitchwise solution average on the boundary, corresponding to the 0^{th} Fourier mode, while the harmonics are defined as follows:

$$\widehat{\boldsymbol{U}}_{p_m}(z) = \frac{1}{P} \int_0^P \boldsymbol{U}_p(0, y, z) e^{-i l_m y} dy \tag{75}$$

where:

$$l_m = \frac{2\pi m}{P} \tag{76}$$

For each span, 2D steady-state non-reflecting boundary conditions can be enforced for every Fourier mode m different from the one of order zero. The boundary conditions are:

$$\boldsymbol{v}_n^L \widehat{\boldsymbol{U}}_{p_m} = 0 \tag{77}$$

Using the eigenvectors introduced in section 3.2.1.3, the previous expression becomes, for the inlet boundary:

$$\begin{pmatrix} -\bar{c}^2 & 0 & 0 & 0 & 1 \\ 0 & -\bar{\rho}\bar{c}\bar{u} & -\bar{\rho}\bar{c}\bar{v} & 0 & -\bar{c} \\ 0 & 0 & 0 & -\bar{\rho}\bar{c}\bar{v} & 0 \\ 0 & -\bar{\rho}\bar{c}\bar{v} & \bar{\rho}\bar{c}\bar{u} & 0 & \beta \end{pmatrix} \widehat{\boldsymbol{U}}_{p_m} = 0 \qquad (78)$$

While, for the outflow, the boundary condition is:

$$\begin{pmatrix} 0 & \bar{\rho}\bar{c}\bar{v} & -\bar{\rho}\bar{c}\bar{u} & 0 & \beta \end{pmatrix} \widehat{\boldsymbol{U}}_{p_m} = 0 \qquad (79)$$

The harmonics can be expressed in terms of the spatial Fourier transform of the characteristic variables:

$$\widehat{\boldsymbol{U}}_{p_m} = \begin{pmatrix} -\dfrac{1}{\bar{c}^2} & 0 & 0 & \dfrac{1}{2\bar{c}^2} & \dfrac{1}{2\bar{c}^2} \\ 0 & 0 & 0 & \dfrac{1}{2\bar{\rho}\bar{c}} & -\dfrac{1}{2\bar{\rho}\bar{c}} \\ 0 & \dfrac{1}{\bar{\rho}\bar{c}} & 0 & 0 & 0 \\ 0 & 0 & \dfrac{1}{\bar{\rho}\bar{c}} & 0 & 0 \\ 0 & 0 & 0 & \dfrac{1}{2} & \dfrac{1}{2} \end{pmatrix} \begin{pmatrix} \hat{\phi}_1 \\ \hat{\phi}_2 \\ \hat{\phi}_3 \\ \hat{\phi}_4 \\ \hat{\phi}_5 \end{pmatrix} \qquad (80)$$

Substituting (80) in (78) and (79) gives, respectively:

$$\begin{pmatrix} 1 & 0 & 0 & 0 & 0 \\ 0 & -\bar{v} & 0 & -\dfrac{\bar{c}+\bar{u}}{2} & \dfrac{\bar{u}-\bar{c}}{2} \\ 0 & 0 & \bar{v} & 0 & 0 \\ 0 & \bar{u} & 0 & \dfrac{\beta-\bar{v}}{2} & \dfrac{\beta+\bar{v}}{2} \end{pmatrix} \begin{pmatrix} \hat{\phi}_1 \\ \hat{\phi}_2 \\ \hat{\phi}_3 \\ \hat{\phi}_4 \\ \hat{\phi}_5 \end{pmatrix} = 0 \qquad (81)$$

and:

$$\begin{pmatrix} 0 & -\bar{u} & 0 & \dfrac{\beta+\bar{v}}{2} & \dfrac{\beta-\bar{v}}{2} \end{pmatrix} \begin{pmatrix} \hat{\phi}_1 \\ \hat{\phi}_2 \\ \hat{\phi}_3 \\ \hat{\phi}_4 \\ \hat{\phi}_5 \end{pmatrix} = 0 \tag{82}$$

Rearranging, it is possible to get some compact relations:

$$\begin{pmatrix} \hat{\phi}_1 \\ \hat{\phi}_2 \\ \hat{\phi}_3 \\ \hat{\phi}_4 \end{pmatrix} = \begin{pmatrix} 0 \\ -\left(\dfrac{\beta+\bar{v}}{\bar{c}+\bar{u}}\right) \hat{\phi}_5 \\ 0 \\ \left(\dfrac{\beta+\bar{v}}{\bar{c}+\bar{u}}\right)^2 \hat{\phi}_5 \end{pmatrix} \tag{83}$$

$$\hat{\phi}_5 = \left(\frac{2\bar{u}}{\beta-\bar{v}}\right) \hat{\phi}_2 - \left(\frac{\beta+\bar{v}}{\beta-\bar{v}}\right) \hat{\phi}_4 \tag{84}$$

Hence, the model enforces incoming characteristics that are function of the outgoing ones. For the annular case, the boundary conditions can be obtained following the same procedure already introduce and substituting (θ, R) for (y, z) and (u_θ, u_R) for (u, v). This approximation applies properly only if the blade pitch is much smaller than the tip radius, which is true for many turbomachinery applications. The approximation error is lower than the one arising due to the uncoupled radial and circumferential modes.

3.2.1.5 Implementation of the method

The non-reflecting boundary conditions are enforced in the TRAF code at every Runge-Kutta stage on fine grid at the point in which the overall numerical scheme has already computed the changes in the conservative variables for all the nodes of the

domain, including the ones on the boundaries, but the nodal values have not yet been updated. The characteristics variations corresponding to these changes in the conservative variables can be determined using proper transformation matrices.

The characteristics variables are used to define the changes in the phantom cell values on the boundary. As already stated, the characteristics are defined in terms of perturbations with respect to the average inflow or outflow. Considering only the case of subsonic axial Mach number, for an inlet boundary the only exiting mode is an upstream running pressure wave. Thus, only the fifth characteristic variable is extrapolated from the interior domain. On the contrary, at an outlet boundary with subsonic axial Mach number, the first four characteristic variables representing the linearized entropy, two vorticity and the downstream running pressure waves are outgoing and can be obtained extrapolating the interior flow-field. The specific treatments adopted for every kind of boundary (e. g. subsonic inlet, supersonic inlet, subsonic outlet, supersonic outlet and inter-row interfaces) are reported in the following sub-sections, for the case of a linear cascade. As explained at the end of section 3.2.1.4, the approximate relations for the annular case can be obtained following the same procedure and substituting (θ, R) for (y, z) and (u_θ, u_R) for (u, v).

Subsonic inlet

For a given spanwise position, the change in the incoming characteristic variables at each point in the tangential direction on the inlet boundary is split into two parts. The first one represents the average change along the boundary, defined to target certain physical quantities. The other component consists of the harmonic variations in the characteristics along the interface, designed to guarantee the non-reflectiveness of the boundary.

The average characteristic changes are calculated starting from the requirement that the average entropy, radial and tangential flow angles, and stagnation enthalpy must have the values specified by the user at the inlet section of the computational domain. This can be obtained driving to zero the following four residuals:

$$R_1^n = \bar{p}^n(\bar{s}^n - \bar{s}_{in}) \tag{85}$$

$$R_2^n = \bar{\rho}^n \bar{c}^n (v_F^n - |\boldsymbol{V}_F^n| \sin(\alpha_{in}) \cos(\beta_{in})) \tag{86}$$

$$R_3^n = \bar{\rho}^n \bar{c}^n (w_F^n - |\boldsymbol{V}_F^n| \sin(\beta_{in})) \tag{87}$$

$$R_4^n = \bar{\rho}^n (\bar{H}^n - \bar{H}_{in}) \tag{88}$$

The superscript n indicates the current iteration step of the overall integration algorithm. In order to maintain the same definition for the first residual in both the perfect gas formulation and the real gas one, s is not the entropy related function used by Giles:

$$s = ln(\gamma p) - \gamma\, ln(\rho) \tag{89}$$

In the TRAF code, the parameter s in the first residual is the entropy that, due to the code scaling, can be expressed as:

$$s = \frac{ln(p) - \gamma\, ln(\rho)}{\gamma - 1} \tag{90}$$

The velocity components, magnitude and flow angles present in the definitions of the second and third residuals are expressed in the relative frame of reference, to make them valid for both rotor and stator case. The angle α is the one formed between the flow direction and the x-axis in the x-y (blade-to-blade)

plane, while the angle β is related to the one formed between the flow direction and the x-axis in the x-z (meridional) plane, β_m, by the following expression:

$$\beta = \tan^{-1}\left(\frac{\tan(\beta_m)}{\cos(\alpha)}\right) \tag{91}$$

The average changes in the incoming characteristic variables are obtained using a one-step Newton-Rapson procedure. Therefore, the residuals are linearized with respect to the current iteration and their values for the n+1 iteration are set equal to zero:

$$\begin{pmatrix} R_1 \\ R_2 \\ R_3 \\ R_4 \end{pmatrix}^{n+1} \cong \begin{pmatrix} R_1 \\ R_2 \\ R_3 \\ R_4 \end{pmatrix}^{n} + \left(\frac{\partial(R_1, R_2, R_3, R_4)}{\partial(\phi_1, \phi_2, \phi_3, \phi_4)}\right)^{n} \begin{pmatrix} \delta\bar{\phi}_1 \\ \delta\bar{\phi}_2 \\ \delta\bar{\phi}_3 \\ \delta\bar{\phi}_4 \end{pmatrix} = 0 \tag{92}$$

Dropping the superscript n and applying the chain rule, the Jacobian matrix can be written as:

$$J = \frac{\partial(R_1, R_2, R_3, R_4)}{\partial(\phi_1, \phi_2, \phi_3, \phi_4)} = \underbrace{\frac{\partial(R_1, R_2, R_3, R_4)}{\partial(\bar{\rho}, \bar{u}, \bar{v}, \bar{w})}}_{J_1} \underbrace{\frac{\partial(\bar{\rho}, \bar{u}, \bar{v}, \bar{w})}{\partial(\bar{\phi}_1, \bar{\phi}_2, \bar{\phi}_3, \bar{\phi}_4)}}_{J_2} \tag{93}$$

After performing the derivatives and not considering the terms proportional to the residuals that are equal to zero at the converged limit, the matrix J_1 assumes the following expression:

$$J_1 = \begin{pmatrix} -\dfrac{\bar{c}^2}{\gamma - 1} & 0 & 0 & 0 & \dfrac{1}{\gamma - 1} \\ 0 & -\bar{\rho}\bar{c}\tan(\alpha_{in}) & \bar{\rho}\bar{c} & 0 & 0 \\ 0 & -\bar{\rho}\bar{c}\tan\left(\beta_{m_{in}}\right) & 0 & \bar{\rho}\bar{c} & 0 \\ -\dfrac{\bar{c}^2}{\gamma - 1} & \bar{\rho}\bar{u} & \bar{\rho}\bar{v} & \bar{\rho}\bar{w} & \dfrac{\gamma}{\gamma - 1} \end{pmatrix} \tag{94}$$

The matrix J_2 can be obtained by dropping the 5^{th} column in the matrix that can be found in (80) and has the following structure:

$$J_2 = \begin{pmatrix} -\frac{1}{\overline{c}^2} & 0 & 0 & \frac{1}{2\overline{c}^2} \\ 0 & 0 & 0 & \frac{1}{2\overline{\rho c}} \\ 0 & \frac{1}{\overline{\rho c}} & 0 & 0 \\ 0 & 0 & \frac{1}{\overline{\rho c}} & 0 \\ 0 & 0 & 0 & \frac{1}{2} \end{pmatrix} \tag{95}$$

The Jacobian matrix J is therefore:

$$J = \begin{pmatrix} \frac{1}{\gamma - 1} & 0 & 0 & 0 \\ 0 & 1 & 0 & -\frac{\tan(\alpha_{in})}{2} \\ 0 & 0 & 1 & -\frac{\tan(\beta_{m\,in})}{2} \\ \frac{1}{\gamma - 1} & \overline{Ma}_y & \overline{Ma}_z & \frac{1}{2}(1 + \overline{Ma}_x) \end{pmatrix} \tag{96}$$

In the matrix J, Ma_x, Ma_y and Ma_z correspond to u/c, v/c and w/c, respectively. The determinant of the Jacobian matrix is given by:

$$\det(J) = \frac{1 + \overline{Ma}_x + \overline{Ma}_y \tan(\alpha_{in}) + \overline{Ma}_z \tan(\beta_{m\,in})}{\gamma - 1} \tag{97}$$

The elements of the inverted Jacobian matrix J^{-1} can be obtained from the following expression:

$$J_{ji}^{-1} = \frac{(-1)^{j+i} det(J^{ij})}{det(J)} \qquad j = 1{,}4;\ i = 1{,}4 \tag{98}$$

where J^{ij} is the matrix obtained from J dropping the i^{th} line and the j^{th} column. Therefore, the average changes in the incoming characteristic variables can be obtained as follows:

$$\begin{pmatrix} \delta\bar{\phi}_1 \\ \delta\bar{\phi}_2 \\ \delta\bar{\phi}_3 \\ \delta\bar{\phi}_4 \end{pmatrix} = -J^{-1} \begin{pmatrix} R_1 \\ R_2 \\ R_3 \\ R_4 \end{pmatrix} \tag{99}$$

For the case considered, these average changes are given by:

$$\delta\bar{\phi}_1 = (1-\gamma)R_1 \tag{100}$$

$$\delta\bar{\phi}_2 = \frac{\tan(\alpha_{in})}{\Delta}(R_1 - \Delta_z R_2 + \overline{Ma}_z R_3 - R_4) \tag{101}$$

$$\delta\bar{\phi}_3 = \frac{\tan(\beta_{m_{in}})}{\Delta}(R_1 + \overline{Ma}_y R_2 - \Delta_y R_3 - R_4) \tag{102}$$

$$\delta\bar{\phi}_4 = \frac{2}{\Delta}(R_1 + \overline{Ma}_y R_2 + \overline{Ma}_z R_3 - R_4) \tag{103}$$

where:

$$\Delta = 1 + \overline{Ma}_x + \overline{Ma}_y \tan(\alpha_{in}) + \overline{Ma}_z \tan\left(\beta_{m_{in}}\right) \tag{104}$$

$$\Delta_y = \frac{1 + \overline{Ma}_x + \overline{Ma}_y \tan(\alpha_{in})}{\tan(\beta_{m_{in}})} \tag{105}$$

$$\Delta_z = \frac{1 + \overline{Ma}_x + \overline{Ma}_z \tan\left(\beta_{m_{in}}\right)}{\tan(\alpha_{in})} \tag{106}$$

The local changes in the characteristic variables for each grid node in the y-direction still need to be evaluated to properly update the solution on the inlet boundary. The first step consists of performing a discrete Fourier transform (DFT) of the outgoing characteristic ϕ_5, that can be used to determine the steady-state amplitude of the incoming characteristics according to the equation (83). Considering a range of values form $-N/2+1$ to $N/2$-1, where N is the number of nodes in the y-direction, and including just once the periodic node, the DFT leads to:

$$\hat{\phi}_{5k} = \frac{1}{N} \sum_{j=1}^{N} \phi_{5j} e^{-\frac{i2\pi jk}{N}} \tag{107}$$

The steady-state amplitude of the Fourier transform of the second characteristic is:

$$\hat{\phi}_{2ks} = -\left(\frac{\beta + \overline{v}}{\overline{c} + \overline{u}}\right) \hat{\phi}_5 \tag{108}$$

with:

$$\beta = i \; sign(k) \sqrt{\overline{c}^2 - (\overline{u}^2 + \overline{v}^2)} \tag{109}$$

The amplitudes in the physical domain are obtained performing an inverse DFT:

$$\phi_{2js} = 2Re \left[\sum_{k=1}^{\frac{N}{2}-1} \hat{\phi}_{2ks} e^{-\frac{i2\pi jk}{N}} \right] \tag{110}$$

The steady-state correction to the local second characteristic variable is, for each node j along the boundary, the difference between the correct steady-state value and the current value:

$$\delta\phi_{2js} = \phi_{2js} - \phi_{2j} = \phi_{2js} - \bar{\rho}\bar{c}(v_j - \bar{v}) \tag{111}$$

As the harmonics of the third incoming characteristic are zero, the correction to apply is:

$$\delta\phi_{3js} = \phi_{3js} - \phi_{3j} = -\phi_{3j} = -\bar{\rho}\bar{c}(w_j - \overline{w}) \tag{112}$$

The corrections to the local first and fourth characteristic variables are obtained from the condition that the local entropy and stagnation enthalpy should match the average values. The residuals are given by perturbations from the average entropy and stagnation enthalpy values:

$$R_{1j} = \bar{p}(s_j - \bar{s}) \tag{113}$$

$$R_{4j} = \bar{\rho}(H_j - \overline{H}) \tag{114}$$

The Newton-Rapson method leads in this case to:

$$\begin{pmatrix} R_{1j} \\ R_{4j} \end{pmatrix}^n = -\begin{pmatrix} \dfrac{1}{\gamma-1} & 0 & 0 & 0 \\ \dfrac{1}{\gamma-1} & \overline{Ma}_y & \overline{Ma}_z & \dfrac{(1+\overline{Ma}_x)}{2} \end{pmatrix} \begin{pmatrix} \delta\phi_{1js} \\ \delta\phi_{2js} \\ \delta\phi_{3js} \\ \delta\phi_{4js} \end{pmatrix} \tag{115}$$

whose solution is:

$$\delta\phi_{1js} = (1-\gamma)R_1 \tag{116}$$

$$\delta\phi_{4js} = -2\frac{\left(\frac{\delta\phi_{1js}}{\gamma-1} + \overline{Ma}_y\delta\phi_{2js} + \overline{Ma}_z\delta\phi_{3js} + R_{4j}\right)}{1+\overline{Ma}_x} \tag{117}$$

Once all the local changes in the incoming characteristic variables have been determined, these can be added to the average changes and multiplied by an under-relaxation factor σ:

$$\delta\phi_{1j} = \sigma(\delta\bar{\phi}_1 + \delta\phi_{1js}) \tag{118}$$

$$\delta\phi_{2j} = \sigma(\delta\bar{\phi}_2 + \delta\phi_{2js}) \tag{119}$$

$$\delta\phi_{3j} = \sigma(\delta\bar{\phi}_3 + \delta\phi_{3js}) \tag{120}$$

$$\delta\phi_{4j} = \sigma(\delta\bar{\phi}_4 + \delta\phi_{4js}) \tag{121}$$

The change in the outgoing fifth characteristic, for the j^{th} node on the interface in the y-direction, is:

$$\delta\phi_{5j} = p_e - p_j + \bar{\rho}\bar{c}(u_e - u_j) \tag{122}$$

The local values for pressure and velocity in the previous expression, with the subscript $_e$, are obtained through a zero or first order extrapolation of the values available in the domain interior. The combined five characteristic changes are hence transformed into variations in the primitive variables according to equation (80) and then into conservative variable changes, in order to update the current solution on the inlet boundary.

The relation that links conservative and primitive variables changes, for the case of a perfect gas, is reported below:

$$\begin{pmatrix} \delta\rho \\ \delta(\rho u) \\ \delta(\rho v) \\ \delta(\rho w) \\ \delta(\rho E) \end{pmatrix} = \begin{pmatrix} 1 & 0 & 0 & 0 & 0 \\ \bar{u} & \bar{\rho} & 0 & 0 & 0 \\ \bar{v} & 0 & \bar{\rho} & 0 & 0 \\ \bar{w} & 0 & 0 & \bar{\rho} & 0 \\ \frac{|\bar{\boldsymbol{V}}|^2}{2} & \bar{\rho}\bar{u} & \bar{\rho}\bar{v} & \bar{\rho}\bar{w} & \frac{1}{\gamma-1} \end{pmatrix} \begin{pmatrix} \delta\rho \\ \delta u \\ \delta v \\ \delta w \\ \delta p \end{pmatrix} \tag{123}$$

Supersonic inlet

This case is implemented similarly to the subsonic inflow case already introduced. The main difference is in the definition of the parameter β, which is:

$$\beta = -sign(\bar{v})\sqrt{(\bar{u}^2 + \bar{v}^2) - \bar{c}^2} \tag{124}$$

Since β does not depend on the Fourier mode k, there is no need to perform the DFT. Therefore, the correct steady-state values for the local incoming second characteristic are:

$$\phi_{2js} = -\frac{\beta + \bar{v}}{\bar{c} + \bar{u}} \qquad j = 1, \dots, N \tag{125}$$

The rest of the procedure is identical to the subsonic inflow case. It is worth to remember that the method here reported is valid only for a supersonic flow that is axially subsonic.

Subsonic outlet

The implementation of non-reflecting boundary conditions on an outlet boundary is way easier than at inflow because there is only one incoming characteristic that must be handled. As in the procedure introduced for the inlet case, the process that allows to determine the fifth characteristic variable change is split in two parts.

The first one allows the user to set an average pressure value $\bar{p}_{out}$ at each span-wise position. The residual used in this case is:

$$R_5^n = p_F^n - \bar{p}_{out} \tag{126}$$

Linearizing the residual from the current iteration gives:

$$R_5^n + \frac{\partial R_5}{\partial \phi_5} \delta \bar{\phi}_5 = 0 \tag{127}$$

From the chain rule:

$$\frac{\partial R_5}{\partial \phi_5} = \frac{\partial R_5}{\partial p} \frac{\partial p}{\partial \phi_5} = \frac{1}{2} \tag{128}$$

Therefore:

$$\delta \bar{\phi}_5 = -2(p_F - \bar{p}_{out}) \tag{129}$$

The second part is related to the local changes. After evaluating the outgoing local second and fourth characteristic variables, their DFT are performed:

$$\hat{\phi}_{mk} = \frac{1}{N} \sum_{j=1}^{N} \phi_{mj} e^{-\frac{i2\pi jk}{N}} \qquad m = 2{,}4 \tag{130}$$

As introduced in section 3.2.1.4, the correct steady-state amplitude of the Fourier transform of the only incoming characteristic for an outlet is reported in the equation (84). Performing an inverse discrete Fourier transform, the local steady-state value for the incoming fifth characteristic can be written as:

$$\phi_{5js} = 2Re\left[\sum_{k=1}^{\frac{N}{2}-1} \hat{\phi}_{5ks} e^{-\frac{i2\pi jk}{N}}\right] \tag{131}$$

The local change is then:

$$\delta\phi_{5js} = \phi_{5js} - \phi_{5j} = \phi_{5js} - \left(p_j - \bar{p} + \bar{\rho}\bar{c}(u_e - u_j)\right) \tag{132}$$

As before, the overall change in the incoming characteristic is obtained summing the average to the local change and introducing an under-relaxation factor σ:

$$\delta\phi_{5j} = \sigma(\delta\bar{\phi}_5 + \delta\phi_{5js}) \tag{133}$$

As far as the outgoing characteristics are concerned, the changes needed are computed using the primitive variables extrapolated from the inner domain:

$$\delta\phi_{1j} = p_e - p_j - \bar{c}^2(\rho_e - \rho_j) \tag{134}$$

$$\delta\phi_{2j} = \bar{\rho}\bar{c}(v_e - v_j) \tag{135}$$

$$\delta\phi_{3j} = \bar{\rho}\bar{c}(w_e - w_j) \tag{136}$$

$$\phi_{4j} = p_e - p_j - \bar{\rho}\bar{c}(u_e - u_j) \tag{137}$$

The combined five characteristic changes are transformed into variations in the primitive variables and then into conservative variable changes, in order to update the current solution on the outlet boundary.

Supersonic outlet

The procedure is identical to the subsonic outlet condition, except for the definition of β that is the same valid for the supersonic inlet case, given by the equation (124). Again, the parameter β is independent of the Fourier mode k and the procedure does not need to perform the DFTs of the second and fourth characteristic variables. The steady state amplitude of the incoming fifth characteristic is simply given by:

$$\phi_{5js} = \left(\frac{2\bar{u}}{\beta - \bar{v}}\right)\phi_{2js} - \left(\frac{\beta + \bar{v}}{\beta - \bar{v}}\right)\phi_{4js} \tag{138}$$

The rest of the boundary condition treatment is the same as for the subsonic outlet.

Inter-row interfaces

In order to get reliable results for steady-state multi-row analyses, mass, momentum and energy have to be conserved across each inter-row interface. Hence, the target is to have a balance of the flux of these quantities through the interfaces between rotor and stator rows. Using the "mixed-out" averaging technique introduced in section 3.2.1.1, an equivalent objective is to match the averaged primitive variables:

$$\rho_{F_R} = \rho_{F_S} \tag{139}$$

$$u_{F_R} = u_{F_S} \tag{140}$$

$$v_{F_R} = v_{F_S} \tag{141}$$

$$w_{F_R} = w_{F_S} \tag{142}$$

$$p_{F_R} = p_{F_S} \tag{143}$$

The subscripts $_R$ and $_S$ refer to rotor and stator, respectively. For the rotor row, the absolute frame of reference needs to be considered in the previous expressions, in order to be able to match the velocities in the y-direction. If there is no balance in these matching conditions in the current solution, this can be interpreted as a jump in the characteristic values:

$$\begin{pmatrix} \Delta\bar{\phi}_1 \\ \Delta\bar{\phi}_2 \\ \Delta\bar{\phi}_3 \\ \Delta\bar{\phi}_4 \end{pmatrix} = \begin{pmatrix} -\bar{c}^2 & 0 & 0 & 0 & 1 \\ 0 & 0 & \bar{\rho}\bar{c} & 0 & 0 \\ 0 & 0 & 0 & \bar{\rho}\bar{c} & 0 \\ 0 & \bar{\rho}\bar{c} & 0 & 0 & 1 \\ 0 & -\bar{\rho}\bar{c} & 0 & 0 & 1 \end{pmatrix} \begin{pmatrix} \rho_{F_R} - \rho_{F_S} \\ u_{F_R} - u_{F_S} \\ v_{F_R} - v_{F_S} \\ w_{F_R} - w_{F_S} \\ p_{F_R} - p_{F_S} \end{pmatrix} \tag{144}$$

The average characteristic changes at each side of the interface are now set to remove these characteristic jumps; once this is done, the remainder of the boundary condition treatment is exactly the same as for standard inflow and outflow boundaries.

3.2.2 Real gas extension

In the turbomachinery industry, many different fluids are used, working on a wide range of thermodynamic operating conditions. For applications concerning compressible fluids, in most of the cases, the perfect gas assumption is accurate enough to properly describe the physical characteristics of the fluid involved. Nevertheless, there are some applications where this simplified approach is not satisfactory. Just to mention one example, in the low-pressure stages of a steam turbine, the thermodynamic transformations occur close or above the steam saturation curve, the latter condition involving a two-phase flow. In practical applications, it is common to carry out also in these demanding cases CFD analyses using the perfect gas model with modified values of the gas constant and the specific heats ratio. However, the assumption that the fluid thermodynamic properties do not affect too much the aerodynamic performance can

be misleading and may result in unacceptable errors in predicting some basic design parameters. An incorrect evaluation of total pressure and temperature values leads to bad predictions of losses, specific work and heat exchange. Errors in evaluating density affect also the computation of momentum components, and consequently the flow structure prediction. Therefore, it is not possible to attain an accurate and reliable analysis for design purposes without considering a proper fluid property modeling.

The non-reflecting boundary condition theory introduced by Giles and extended to the 3D case by Saxer was developed assuming that the fluid considered could be properly modelled as a perfect gas. To make this model ready to be used as a standard for all compressible fluid turbomachinery applications, a real gas version of it has been implemented in the TRAF code in 2016.

The extension to the real gas case consisted in removing all the perfect gas assumptions present in Giles' and Saxer's theory. The key differences from the perfect gas version are an iterative procedure to compute mixed-out quantities from the mean fluxes of the governing conservative variables and the use of numerical derivatives instead of analytical expressions in some of the terms within the matrices already introduced in section 3.2.1.

3.2.2.1 Mixed-out flow quantities

For the perfect gas case, the mixed-out values of the primitive variables could be obtained analytically by solving a system of five equations and five unknowns reported in expressions (38), (39) and (40). Removing the perfect gas assumption, it is no more possible to find an analytical relation connecting the fluid enthalpy and its pressure. Therefore, the evaluation of the mixed-out values of the primitive variables must be performed through an iterative procedure. Considering again the case of a

linear cascade in a Cartesian environment, the system of equations already mentioned can be rearranged as:

$$\begin{cases} \bar{F}_1 = \rho_F(\boldsymbol{V}_F \cdot \boldsymbol{n}) \\ \bar{F}_2 = \rho_F(\boldsymbol{V}_F \cdot \boldsymbol{n})u_F + p_F n_x \\ \bar{F}_3 = \rho_F(\boldsymbol{V}_F \cdot \boldsymbol{n})v_F + p_F n_y \\ \bar{F}_4 = \rho_F(\boldsymbol{V}_F \cdot \boldsymbol{n})w_F + p_F n_z \\ \bar{F}_5 = \rho_F(\boldsymbol{V}_F \cdot \boldsymbol{n})H_f \end{cases} = \begin{cases} \bar{F}_1 = \rho_F(u_F n_x + w_F n_z) \\ \bar{F}_2 = \bar{F}_1 u_F + p_F n_x \\ \bar{F}_3 = \bar{F}_1 v_F \\ \bar{F}_4 = \bar{F}_1 w_F + p_F n_z \\ \bar{F}_5 = \bar{F}_1 H_f \end{cases} \tag{145}$$

As each inlet/outlet interface of the computational grids used to run the TRAF code is built so that it is orthogonal to the y-direction (θ for the annular case), the $y(\theta)$-component of the interface normal vector $\boldsymbol{n}$ is zero.

The mixed-out values for the y-component of velocity and the total enthalpy can be easily found:

$$v_F = \frac{\bar{F}_3}{\bar{F}_1} \tag{146}$$

$$H_f = \frac{\bar{F}_5}{\bar{F}_1} \tag{147}$$

Solving both second and fourth equations of the system (145) for the variable p_F and imposing their equality, the z-component of velocity can be derived:

$$w_F = \frac{\bar{F}_4 - \frac{n_z}{n_x}(\bar{F}_2 - \bar{F}_1 u_F)}{\bar{F}_1} \tag{148}$$

Substituting (148) in the first equation of the system (145) and solving for u_F:

$$u_F = \frac{n_x}{n_x^2 + n_z^2}\left(\frac{\bar{F}_1}{\rho_F} - n_z\frac{\bar{F}_4}{\bar{F}_1} + \frac{n_z^2}{n_x}\frac{\bar{F}_2}{\bar{F}_1}\right) = f(\rho_F) \tag{149}$$

The mixed-out pressure can be obtained solving the second equation of the system (145):

$$p_F = \frac{\bar{F}_2 - \bar{F}_1 u_F}{n_x} \tag{150}$$

For each interface band in the spanwise direction of width dz, the iterative procedure to compute the mixed-out values for the primitive variables is structured as follows:

1) The mixed-out values for the y-component of velocity and the total enthalpy are computed according to (146) and (147).

2) The mixed-out primitive variables values are initialized to the band-averaged values.

3) The static enthalpy value is obtained subtracting the dynamic component from the total enthalpy:

$$h_F(i) = H_F - |\boldsymbol{V}_F|^2(i)$$

4) The mixed-out value of density is obtained by interrogating the gas tables, using as input the current mixed-out values of pressure and static enthalpy:

$$p_F(i), h_F(i) \rightarrow \rho_F(i)$$

5) The x-component of mixed-out velocity is computed according to (149).

6) Once obtained u_F, the mixed-out values of z-component of velocity and pressure can be calculated using (148) and (150), respectively.

7) The steps from 3 to 6 are repeated until the convergence of the process is reached.

Two convergence criteria have been adopted for the iterative process, one is based on the number of iterations and the other one on a relative tolerance on the mixed-out pressure value.

3.2.2.2 Average characteristic changes

The average characteristic changes are determined in order to enforce certain average conditions on the inlet/outlet boundaries. As already introduced in section 3.2.1.5, this is attained driving to zero some residuals that are linearized using a one-step Newton-Rapson procedure. To linearize the residuals, their derivatives with respect to the primitive variables need to be computed. Adopting the perfect gas approximation, all these derivatives do have an analytic expression, usually a function of the gas specific heats ratio γ. On the contrary, when removing the perfect gas assumption, some of the derivatives need to be performed through a numerical procedure, as it is not possible to solve them analytically.

For the case of an outflow, in which only the fifth residual (126) must be driven to zero, the computation of the average change in the incoming characteristic can be done as illustrated for the perfect gas case.

Conversely, when dealing with an inflow boundary, some differences arise if the perfect gas assumption is removed. In this case,

four residuals are introduced to force the solution to have a specified value for the average entropy, flow angles and the stagnation enthalpy at the inlet (see section 3.2.1.5). Between these residuals, two must be carefully handled in order to properly model the real gas case, i.e. the first and fourth ones given by (85) and (88), respectively.

For both the first and the fourth residuals, the derivatives that are different from the perfect gas case are the ones with respect to density and pressure:

$$\frac{\partial R_1}{\partial \rho} = \bar{p}\frac{\partial s}{\partial \rho}\bigg|_{p=cost} \tag{151}$$

$$\frac{\partial R_1}{\partial p} = \bar{s} - \bar{s}_{in} + \bar{p}\frac{\partial s}{\partial p}\bigg|_{\rho=cost} \cong \bar{p}\frac{\partial s}{\partial p}\bigg|_{\rho=cost} \tag{152}$$

$$\frac{\partial R_4}{\partial \rho} = \bar{H} - \bar{H}_{in} + \bar{\rho}\frac{\partial H}{\partial \rho}\bigg|_{p=cost} \cong \bar{\rho}\frac{\partial H}{\partial \rho}\bigg|_{p=cost} \tag{153}$$

$$\frac{\partial R_4}{\partial p} = \bar{\rho}\frac{\partial H}{\partial p}\bigg|_{\rho=cost} \tag{154}$$

Therefore, the Jacobian matrix assumes the following structure:

$$J = \begin{pmatrix} -\dfrac{\bar{p}}{\bar{c}^2}\dfrac{\partial s}{\partial \rho}\bigg|_p & 0 & 0 & \dfrac{\bar{p}}{2}\left(\dfrac{\partial s}{\partial p}\bigg|_\rho + \dfrac{1}{\bar{c}^2}\dfrac{\partial s}{\partial \rho}\bigg|_p\right) \\ 0 & 1 & 0 & -\dfrac{\tan(\alpha_{in})}{2} \\ 0 & 0 & 1 & -\dfrac{\tan(\beta_{m_{in}})}{2} \\ -\dfrac{\bar{\rho}}{\bar{c}^2}\dfrac{\partial H}{\partial \rho}\bigg|_p & \overline{Ma}_y & \overline{Ma}_z & \dfrac{\overline{Ma}_x + \bar{\rho}\dfrac{\partial H}{\partial p}\bigg|_\rho - \dfrac{\bar{\rho}}{\bar{c}^2}\dfrac{\partial H}{\partial \rho}\bigg|_p}{2} \end{pmatrix} \tag{155}$$

The average changes in the incoming characteristics can be found, once calculated the inverted Jacobian matrix J^{-1}, according to (99).

3.2.2.3 Corrections to local characteristics

As explained in section 3.2.1.5, the steady-state corrections to the local first and fourth incoming characteristic variables need a particular treatment in order to guarantee that both local entropy and stagnation enthalpy match the average values. Using the first and the fourth row of the matrix J reported in (155), the Newton-Rapson equation, that for the perfect gas case was given by (115), becomes:

$$\boldsymbol{R}_j = -\begin{pmatrix} -\dfrac{\bar{p}}{\bar{c}^2}\dfrac{\partial s}{\partial \rho}\Big|_p & 0 & 0 & \dfrac{\bar{p}}{2}\left(\dfrac{\partial s}{\partial p}\Big|_\rho + \dfrac{1}{\bar{c}^2}\dfrac{\partial s}{\partial \rho}\Big|_p\right) \\ -\dfrac{\bar{\rho}}{\bar{c}^2}\dfrac{\partial H}{\partial \rho}\Big|_p & \overline{Ma}_y & \overline{Ma}_z & \dfrac{\Gamma}{2} \end{pmatrix} \delta\boldsymbol{\phi}_{js} \qquad (156)$$

where:

$$\boldsymbol{R}_j = \begin{pmatrix} R_{1j} \\ R_{4j} \end{pmatrix}; \quad \delta\boldsymbol{\phi}_{js} = \begin{pmatrix} \delta\phi_{1js} \\ \delta\phi_{2js} \\ \delta\phi_{3js} \\ \delta\phi_{4js} \end{pmatrix} \qquad (157)$$

and:

$$\Gamma = \overline{Ma}_x + \bar{\rho}\frac{\partial H}{\partial p}\Big|_\rho - \frac{\bar{\rho}}{\bar{c}^2}\frac{\partial H}{\partial \rho}\Big|_p \qquad (158)$$

Thus, the values of the local steady-state corrections to the first and the fourth incoming characteristic for an inlet can be found by solving the system (156).

3.2.2.4 Conservative variables change

Once determined, for every node on the boundary at a certain spanwise position, the overall chance in the characteristic variables, it is finally possible to update the solution in this location. This update is attained in two steps: the change in the characteristics is first transformed in a variation in the primitive variables and then, the latter variation, is converted in a change in the conservative variables. The first step can be achieved using the transformation matrix reported in the expression (80), which is valid for every gas model adopted, as far as the speed of sound is properly determined. Conversely, the second step needs a peculiar treatment for the real gas case, for which the transformation between primitive and conservative variables is given by:

$$\begin{pmatrix} \delta\rho \\ \delta(\rho u) \\ \delta(\rho v) \\ \delta(\rho w) \\ \delta(\rho E) \end{pmatrix} = \begin{pmatrix} 1 & 0 & 0 & 0 & 0 \\ \bar{u} & \bar{\rho} & 0 & 0 & 0 \\ \bar{v} & 0 & \bar{\rho} & 0 & 0 \\ \bar{w} & 0 & 0 & \bar{\rho} & 0 \\ \bar{E} + \bar{\rho}\left.\dfrac{\partial e}{\partial \rho}\right|_p & \bar{\rho}\bar{u} & \bar{\rho}\bar{v} & \bar{\rho}\bar{w} & \bar{\rho}\left.\dfrac{\partial e}{\partial p}\right|_\rho \end{pmatrix} \begin{pmatrix} \delta\rho \\ \delta u \\ \delta v \\ \delta w \\ \delta p \end{pmatrix} \tag{159}$$

3.2.2.5 Numerical derivatives

As shown in the previous sections, to extend the non-reflecting boundary condition model to the case of a real gas, some numerical derivatives with respect to density and pressure need to be computed. In the TRAF code, these derivatives have been expressed in terms of finite differences. The pressure and density variations to be used in the derivatives have been determined through pseudo-isentropic relations:

$$dp = p' \left(\left(1 + \frac{\gamma_0 - 1}{2} {Ma_0}^2 \right)^{\gamma_0 / \gamma_0 - 1} - 1 \right) \tag{160}$$

$$d\rho = \rho' \left(\left(1 + \frac{\gamma_0 - 1}{2} {Ma_0}^2 \right)^{1/\gamma_0 - 1} - 1 \right) \qquad (161)$$

The pressure p' and density ρ' are local values when computing the derivatives needed for the transformation matrix from primitive to conservative variables, while they are band-averaged values in the Jacobian matrix (155) and in the system of equations (156).

The specific heats ratio γ_0 and Mach number Ma_0 introduced in the previous expressions are reference values adopted to have a relatively small variation in both pressure and density.

The derivative of a generic quantity φ (e.g. entropy, stagnation enthalpy or internal energy) with respect to pressure has the following expression:

$$\left. \frac{\partial \varphi}{\partial p} \right|_{\rho} = \frac{\varphi_2 - \varphi_1}{2dp} \qquad (162)$$

where the values φ_1 and φ_2 are computed interpolating the gas table that gives φ as a function of pressure and density:

$$\varphi_1 = f(p' - dp, \rho') \qquad (163)$$

$$\varphi_2 = f(p' + dp, \rho') \qquad (164)$$

Following a similar procedure, it is possible to determine also the derivative of a generic quantity with respect to density. For this case:

$$\left. \frac{\partial \varphi}{\partial \rho} \right|_{p} = \frac{\varphi_2 - \varphi_1}{2d\rho} \qquad (165)$$

$$\varphi_1 = f(p', \rho' - d\rho) \tag{166}$$

$$\varphi_2 = f(p', \rho' + d\rho) \tag{167}$$

3.2.3 Near-wall treatment

There are two main issues connected with the non-reflecting boundary condition model presented in the previous sections. The first is related to the definition of the mixed-out average of the primitive variables, while the second one derives from the different conditions to be applied for an inflow or an outflow boundary.

As can be noticed from the mixed-out velocity definition reported in the expression (42), each component is defined as a ratio whose denominator is the flux $\bar{F}_1$, that is the average mass-flow. Therefore, when the normal velocity across the interface at a certain span has a very low magnitude, the procedure to compute mixed-out flow variables tends to become unstable and this can result in an abrupt divergence of the simulation.

Another occurrence that is quite challenging from a numerical point of view for the non-reflecting model is a flow reversal across an inter-row interface. As already introduced, the treatments for an inflow and an outflow are different and switching the conditions on one portion of the interface during the pseudo-time integration to follow the evolution of a separation could un-stabilize the computation.

Both these issues refer to flow conditions that are typically verified next to the channel endwalls. To face them and increase the robustness of the model, it is possible to use the reflecting model for a certain percentage of the channel span next to the

endwalls. In the reflecting model, the boundary conditions imposed in each phantom cell on one side of the interface are obtained by averaging in the pitchwise direction the values of the governing conservative variables of the grid cells at the same span on the other interface side. As the model consists of a simple averaging of the conservative variables, it can perfectly handle flow reversals and low velocity magnitudes without stability issues.

If there are no flow reversals across the mixing planes within the computational domain, the use of the reflecting model for $1 \div 2\%$ of the channel span next to hub and tip endwalls is usually enough to assure the stability of the computation.

3.2.4 Model results

The use of non-reflecting boundary conditions is highly beneficial in turbomachinery applications characterized by low inter-row gaps and/or shock waves reaching the inter-row interfaces or the domain inlet/outlet boundary. In order to assess the improvements attained with the non-reflecting model presented in section 3.2, a particularly challenging example can be considered. It consists of the Inlet Guide Vanes (IGV) and the first stage of a heavy-duty multistage axial compressor. In this case, the rotor row generates a shock structure reaching the interface with the upstream IGV row and the axial distance between the rows of the first compressor stage is less than half of the axial chord of the rotor blades. The outline of the computational environment considered is shown in Figure 3.4.

Three steady-state simulations have been performed adopting different mixing-plane models for the inter-row interfaces within the computational domain. In particular, one analysis has been run with the reflecting mixing-plane model while the others have been carried out with the non-reflecting boundary condition

model in both its old and new implementation in the TRAF code. Furthermore, a full-annulus unsteady analysis has been performed to use its average results as a reference.

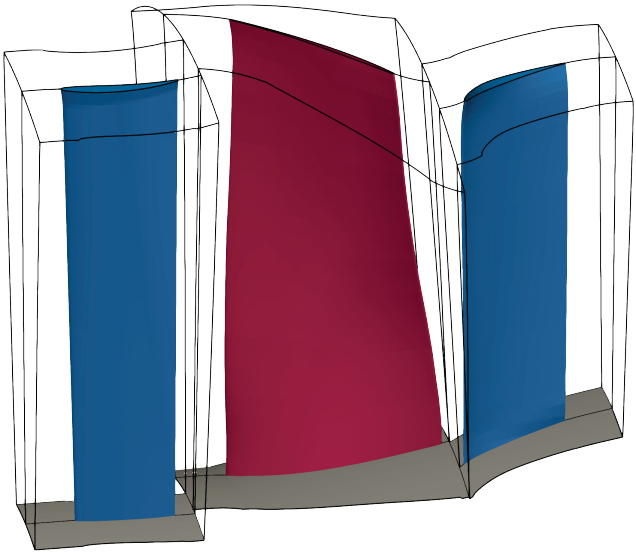

Figure 3.4 Turbomachinery environment used to test the non-reflecting boundary condition model

For all the analyses, uniform inlet boundary conditions and the outlet value of static pressure at the compressor casing have been set, the latter one used by the code to enforce the radial equilibrium on the domain outlet boundary. As far as turbulence closure is concerned, the two-equation k-ω model has been adopted.

The results in terms of mass-flow elaborated by the compressor at each interface of the computational domain are reported in

Figure 3.5. The average inlet mass-flow coming from the unsteady simulation ($\dot{m}_{Ref}$) is used as reference value to scale the data in the plot. The interface referred to as 0 is the one upstream of the IGV row, the interface 1 separates the IGV and the rotor row, the interface 2 is the one between rotor and stator row, while the interface 3 refers to the computational domain outlet.

The steady-state simulations with the reflecting mixing-plane model (RBC) and the new non-reflecting boundary condition model (NRBC new) have comparable mass-flow shifts at the inter-row interfaces with respect to the averaged unsteady solution (UNST).

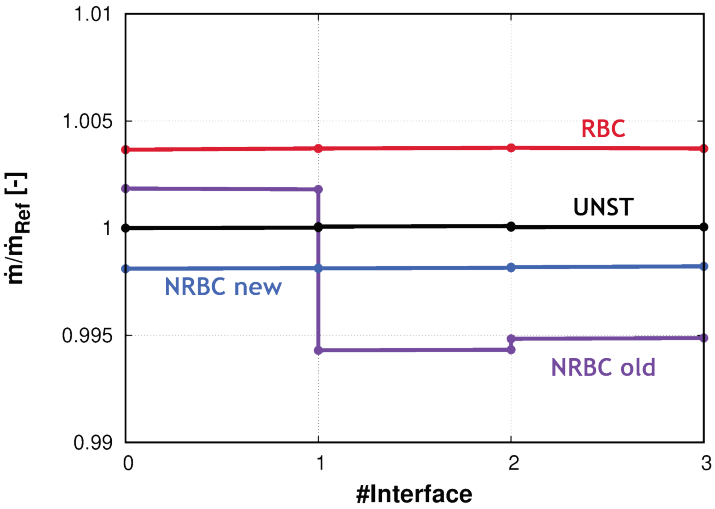

Figure 3.5 Mass-flow at row interfaces

On the contrary, the steady computation with the old implementation of the non-reflecting model (NRBC old) shows remarkable errors, especially through the IGV/rotor interface,

reached by the shock structure generated by the rotor row. Even if the interface mass-flow shift is less than 1% of the inlet value, it cannot be accepted when dealing with multi-stage compressors with a high stage count, in which even a relatively low error at each interface can lead to incorrect mass-flow evaluations in the rear part of the machine, resulting in a wrong stage matching and overall performance prediction.

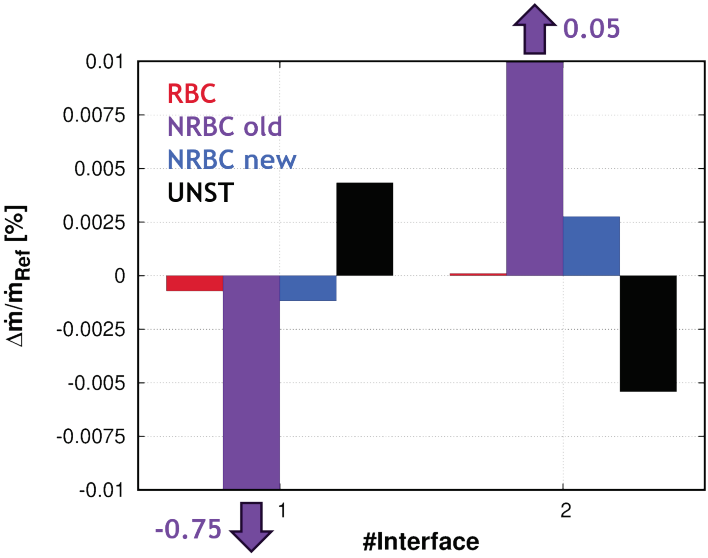

Figure 3.6 Percentage mass-flow shift at interfaces

The percentage mass-flow shift at inter-row interfaces with respect to the inlet value obtained for the unsteady computation ($\dot{m}_{Ref}$) is shown in Figure 3.6. The shift resulting from the steady-state computations with reflecting and newly implemented non-reflecting boundary conditions is lower than the discretization error that characterizes the unsteady solution. Conversely, the old implementation of the non-reflecting mixing

plane model leads to an error that is two orders of magnitude bigger than the unsteady one for the interface between the IGV and the rotor row.

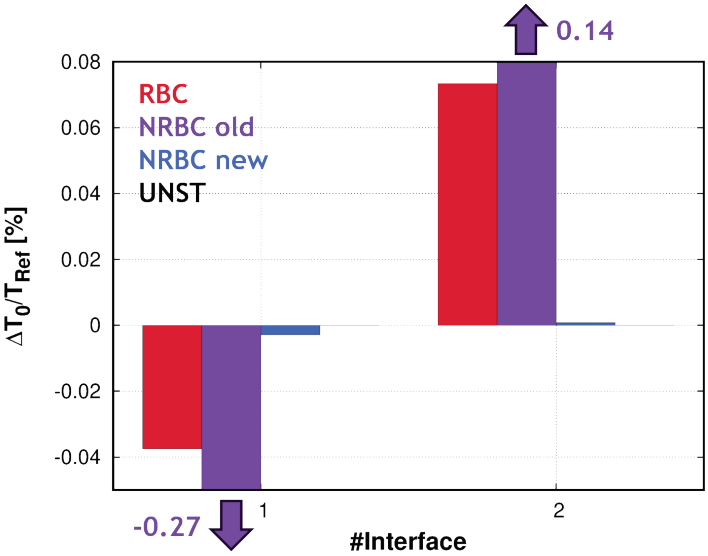

Figure 3.7 Percentage total temperature shift at interfaces

Another thermodynamic parameter that needs to be conserved across each interface between adjacent rows is the total temperature. In order to check the conservation of this flow parameter for the simulations that have been carried out, the percentage total temperature shift at inter-row interfaces with respect to the average inlet total temperature of the unsteady computation (T_{Ref}) is presented in Figure 3.7. A really good temperature conservation is shown by both the unsteady simulation and the steady-state one with the new non-reflecting boundary condition model, while the other analyses face some conservation issues with respect to this parameter.

The blade-to-blade visualization reported in Figure 3.8 helps to highlight the limits of a steady-state modelling of the flow that uses the reflecting mixing plane model. The section considered is the one at channel mid-span and the static pressure contours are presented in the image. Focusing on the inlet interface of the rotor row, as the reflecting mixing plane model forces the solution to have a constant pressure value in the tangential direction on the boundary, the contours need to close before reaching the interface and tend to assume a non-physical configuration. Especially in presence of a significant pressure gradient in the circumferential direction (e.g. when the shock reaches the interface), this limitation can highly affect the solution.

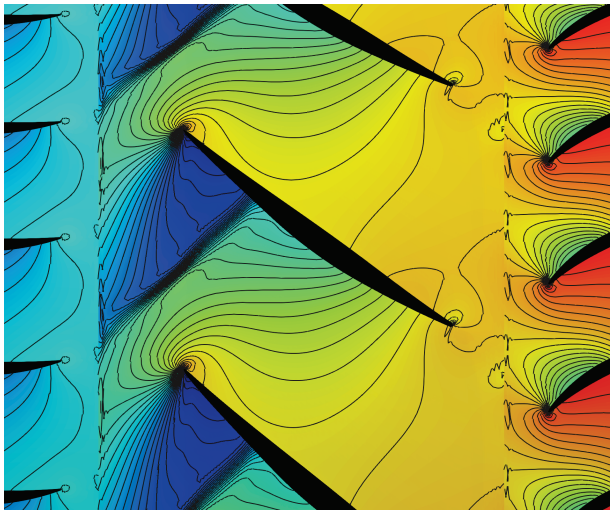

Figure 3.8 Pressure contours at mid-span for the steady run with the reflecting mixing plane model

The correct representation of the flow-field in terms of static pressure close to each inter-row interface is the one shown in Figure 3.9, which refers to the average solution of the unsteady

analysis. Focusing again on the inlet interface of the rotor row, as expected, the pressure contours reaching the boundary are open and hence the static pressure distribution in the circumferential direction on the boundary for a given spanwise position is not uniform.

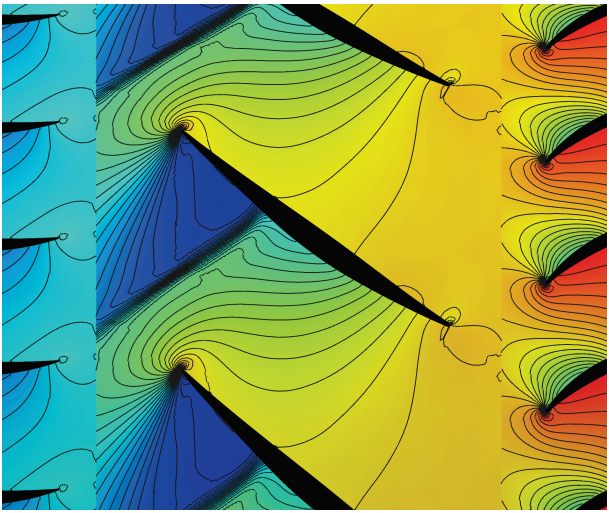

Figure 3.9 Pressure contours at mid-span referring to the time-averaged unsteady solution

The static pressure blade-to-blade visualization at mid-span section for the steady-state run adopting the new non-reflecting mixing plane model is reported in Figure 3.10. The really good match with the averaged unsteady case can be easily verified by comparing this visualization with the one in Figure 3.9.

The interface model does not only impact on the pressure contours in a blade-to-blade plane, but also on some important key design parameters as the blade loading. The loading in terms of isentropic Mach number distribution for the first rotor blade is presented in Figure 3.11. The distributions reported in the figure

refer to five different spanwise positions: 5%, 25%, 50%, 75% and 95% of the channel height. In general, there is a really good agreement between the loading distributions coming from the steady simulations with non-reflecting boundary conditions and the averaged unsteady one. On the contrary, the steady analysis adopting the reflecting mixing plane model shows remarkable departures, especially in predicting the position of the shock-wave on the blade suction side.

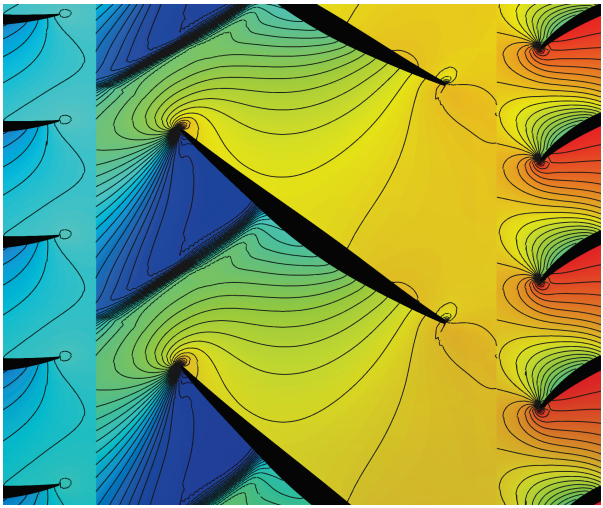

Figure 3.10 Pressure contours at mid-span for the steady run with the new non-reflecting mixing plane model

Considering the load distributions on the first stage stator, presented in Figure 3.12, also in this case the good match between steady computations with non-reflecting boundary conditions and the unsteady averaged results is confirmed. The steady distribution with RBC has a different shape with respect to the others in the lower 50% of blade span, where the interface is really close to the leading edge and the reflection impact is, therefore, magnified.

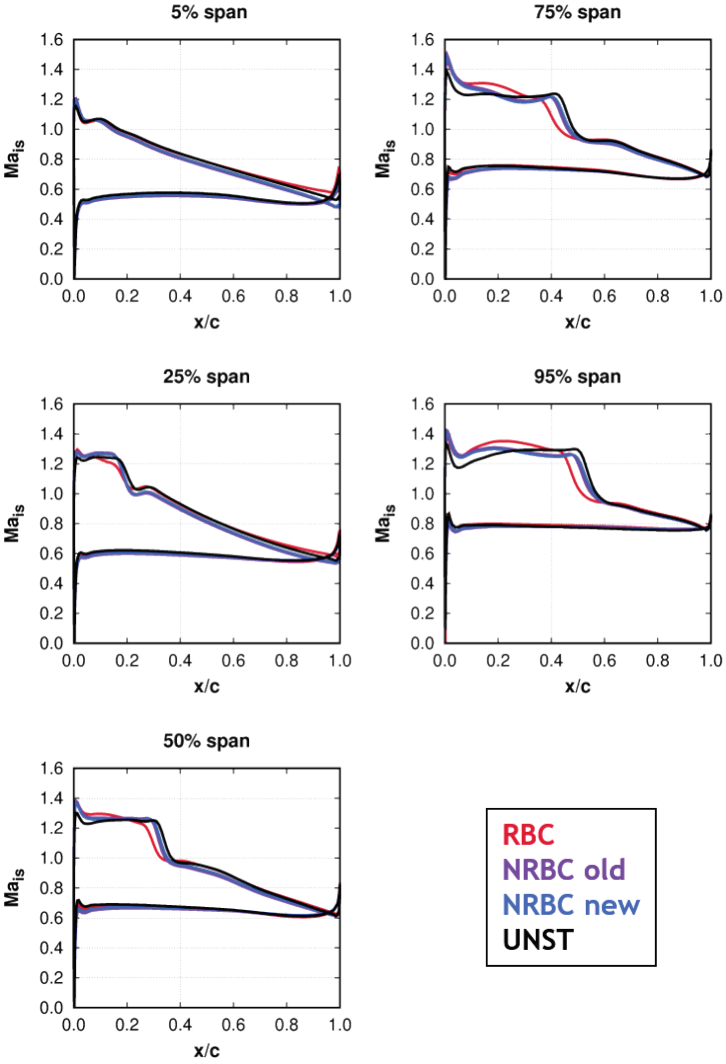

Figure 3.11 Isentropic Mach distributions for the rotor of the first compressor stage

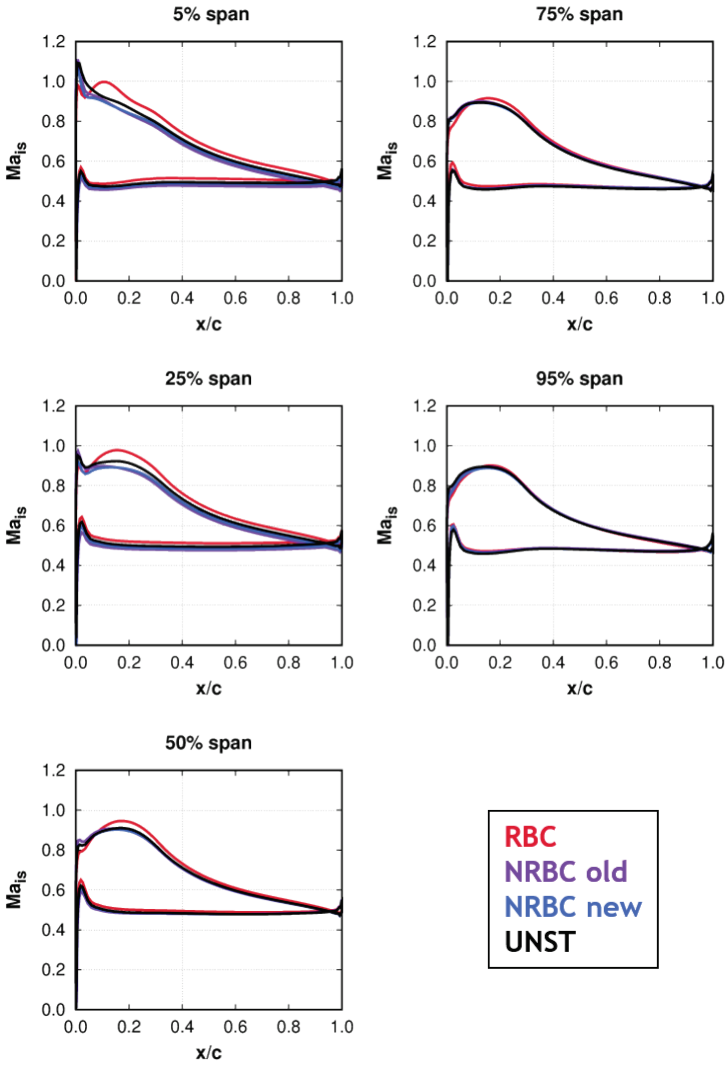

Figure 3.12 Isentropic Mach distributions for the stator of the first compressor stage

4 Numerical Setup for Axial Compressors

Multi-stage axial compressors have always been a great challenge for designers since the flow within this kind of machines, subjected to severe diffusion, is usually characterized by complex and widely developed 3D structures, especially next to the endwalls. The development of reliable numerical tools capable of providing an accurate prediction of the overall machine performance is one of the main research focus areas in the multi-stage axial compressor field. This chapter is intended to present the strategy used to run numerical simulations on compressors achieved during the last few years in the framework of the collaboration between the University of Florence and Ansaldo Energia (AEN), one of the most important companies competing on the world's market of turbomachinery for power generation. All peculiar aspects of the numerical setup are introduced, such as rotor/stator tip clearance modelling, simplified shroud leakage model, gas and turbulence models.

The setup has been validated on an existing machine produced and experimentally tested by Ansaldo Energia. In order to evaluate the impact on performance prediction of the mixing planes introduced in the steady-state computation, unsteady simulations of the whole compressor have been performed at different operating conditions. These calculations have been carried out both at the compressor design point and close to the surge-line, to evaluate the effect of rotor/stator interaction along the compressor working line.

4.1 Challenges in compressors modelling

Multi-stage axial compressors often put a strain on CFD modelling, especially when dealing with off-design operating conditions. However, the need for increasing efficiency and operating range of existing machines pushed the diffusion of CFD tools able to handle multi-stage computational domains within industrial R&D departments [55] [56] [57]. Multistage 3D steady-state RANS simulations started to appear and be used in the 1990's [58], but some decisive aspects of this kind of analysis are still open. Probably the most crucial one is the way to model the interface between stator and rotor rows, in which a circumferential averaging of some sort must be introduced to remove the effects of unsteadiness that are inherent in turbomachinery applications. The averaging process is performed at the interface between adjacent rows in relative motion, called "mixing plane". The first example of multi-row steady-state simulation with the use of mixing planes was published by Denton [59]. In case of small inter-row gaps and/or shock systems reaching the mixing plane, both typically encountered in modern axial compressors, the unrealistic reflections due to a simple circumferential averaging of the flow are enhanced and can lead to inaccurate results. To overcome this issue, Giles developed a non-reflecting boundary conditions theory [60], which started to be used by other authors (e.g. [61]) in the 1990's. Even though mixing plane models with non-reflecting boundary conditions have been used for decades, fluxes conservation and model robustness are still open issues, as demonstrated by several recent publications concerning these topics [62] [63] [64]. Furthermore, the extension to the real gas case of a non-reflecting mixing plane model is rarely addressed in the open literature (e. g. [62]). Steady-state multistage analysis is nowadays a standard for industrial design and design-validation purposes, but understanding the limitations of

this kind of modelling is important for contemporary designers as pointed out by Denton [65]. Some experiences in accounting for unsteady effects in turbomachinery can be found in [66] and [67]. As the computational cost of unsteady simulations on high stage count turbomachines is not yet suitable for industrial needs, assessing the level of accuracy of steady-state approximation still has a great interest.

4.2 Numerical setup

In the framework of the joined research activity between the University of Florence and Ansaldo Energia, an advanced numerical setup for routine steady-state multi-stage axial compressor simulations has been developed, based on the use of the TRAF code introduced in chapter 3. This setup is intended to be an optimal compromise between accuracy, robustness, detailed description of the compressor features impacting on its aerodynamics and computational cost.

Among the several options available in the code, the following have been adopted:

- cell-centered finite volume scheme
- scalar artificial dissipation
- algebraic Baldwin-Lomax turbulence closure

The algebraic Baldwin-Lomax model has been chosen because of its robustness compared with more complex one- and two-equation turbulence models. Furthermore, in compressors with high clearance to blade span ratios, non-algebraic models have sometimes shown convergence issues in steady-state computation even next to the design operating condition.

4.2.1 Gas model

As far as axial compressors of heavy-duty gas turbines are concerned, the working fluid is intended to be air operating in thermodynamic conditions far away from the critical ones, both in terms of pressure and temperature. Between the categories of gas behaviors classified in [68], the most suitable for modelling the fluid evolving in the compressor of an industrial gas turbine is the thermally perfect gas. Such kind of gas obeys the thermal equation of state and is characterized by the fact that specific internal energy, specific enthalpy and the specific heats are only functions of temperature. As shown in [69] for gas turbine applications, the use of a real gas model which considers the specific heat variation with temperature allows a good prediction of the thermodynamic behavior of the working fluid. This real gas model is the standard adopted to run simulations of compressors designed by Ansaldo Energia.

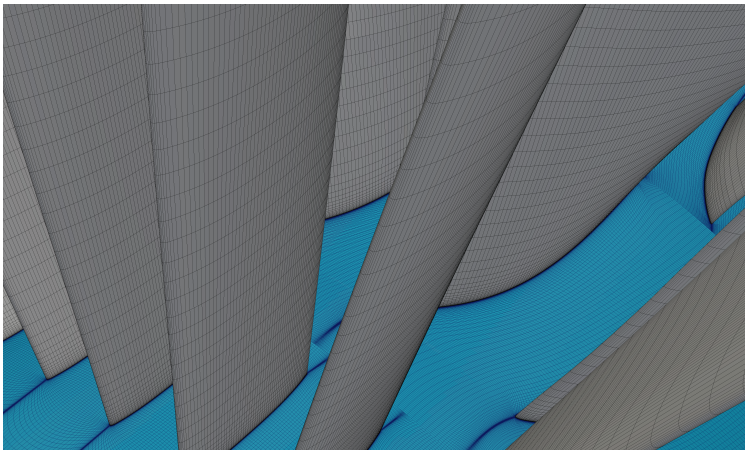

Figure 4.1 Example of a H-type grid adopted for multi-stage steady-state simulations

4.2.2 Computational Grids

When dealing with standard full-compressor analyses, the domain discretization adopted for design and design-validation purposes is based on elliptic H-type grids. Each block has typical dimensions of 141×65×81 grid points in streamwise, pitchwise, and spanwise directions, respectively. Therefore, the number of nodes for each vane is around 0.75 million. A visualization of a computational grid, including three front rows of an F-class GT compressor is reported in Figure 4.1. In the image, the hub endwall surface is colored blue, while the blade surfaces are the gray colored ones.

4.2.3 Mixing plane model

After the extension to the real gas case of the non-reflecting boundary conditions presented in chapter 3, the mixing plane model adopting these conditions has become the standard one for full compressor steady-state analysis. In the development of the non-reflecting model, particular attention has been paid to mass-flow conservation across the interface. This because, especially with axial compressors that generally tend to have a high stage count, also a relatively low error at each interface can lead to unacceptable mass-flow evaluations in the rear part of the machine, resulting in a wrong prediction of the stage matching and overall performance.

In addition to the results on a small computational domain shown when introducing the non-reflecting boundary conditions, this newly implemented mixing plane model has been tested also on full-compressor analyses in order to confirm its good mass-flow conservation properties. The results in terms of mass-flow conservation of steady-state simulations at design point, performed on the 15-stage AE94.3A GT compressor produced by Ansaldo Energia, using both the non-reflecting mixing plane

model and the reflecting one currently available in the TRAF code, are shown in Figure 4.2.

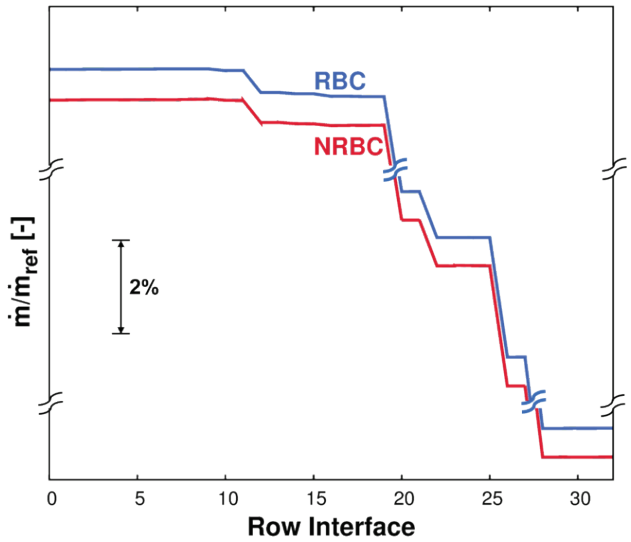

Figure 4.2 Mass-flow along meridional channel using reflecting and non-reflecting mixing plane models

In design conditions, the compressor of this F-class GT has a pressure ratio of about 18:1 and an inlet mass flow around 680 kg/s (see [70] for further details). The computational domain includes the Inlet Guide Vanes (IGV) and the Outlet Guide Vanes (OGV) of the compressor, which is characterized by five air extractions along the meridional flow path. The conservation of mass-flow obtained with the non-reflecting model (NRBC) is comparable to that of the reflecting one (RBC). The different inlet mass-flow predicted by the two models is mainly due to the modifications in the shock structure in front of the first transonic rotor caused by reflections.

4.2.4 Shroud leakage model

Seal cavities under stator rows are a common feature in heavy-duty multi-stage axial compressors. In general, the flow structures which arise inside shrouded cavities are quite complex and typically characterized by axial, radial, and circumferential non-uniformities. Their impact on the main flow-path must be taken into account to properly predict the overall compressor performance, but a detailed 3D solution of all the cavities would lead to a significant growth of the computational cost and possible convergence issues, especially in steady-state simulations. Both these aspects make this option not attractive for industrial design purposes. Nevertheless, the effects of seal cavity flows on the mainstream may be reliably taken into account using a simplified one-dimensional correlation-based cavity model. This is the strategy chosen for the TRAF code, in which a simplified shroud leakage model is available. This model took inspiration from the work presented by Wellborn et al. [71] and a detailed description of it is provided in [72]. A one-dimensional model of shrouded cavity flow is used to estimate the leakage mass-flow, total enthalpy variation, and change in angular momentum having as inputs some geometric parameters and the flow conditions at the interface connecting the cavity with the meridional flow path. The influence of the shroud cavity on the primary flow is considered by imposing coupled source/sink boundary conditions at the cavity/mainstream interface.

To show the impact of the model on a steady-state analysis, two different single-row simulations have been performed on a compressor vane of an existing Ansaldo Energia gas turbine. The first has been run using the shroud leakage model to account for the cavity flow effect while, in the other, wall boundary conditions have been imposed on the cavity inlet and outlet areas on

the hub endwall. The same inlet and outlet boundary conditions for the computational domain have been used for both cases.

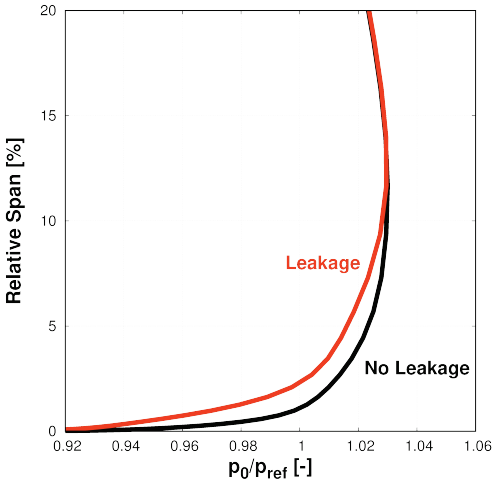

Figure 4.3 Total pressure profile at stator row exit

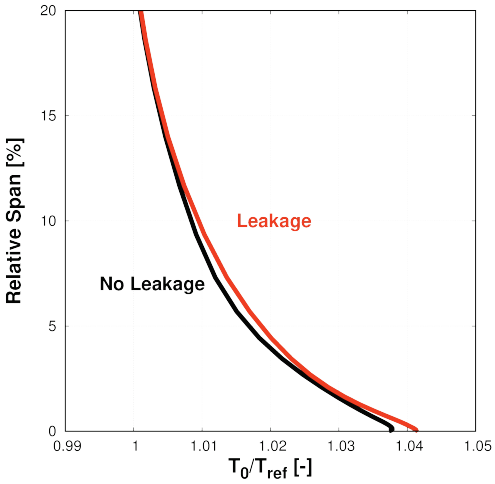

Figure 4.4 Total temperature profile at stator row exit

The results of these numerical simulations in terms of total pressure and temperature outlet radial distributions are shown in Figure 4.3 and Figure 4.4, respectively. As expected, the interaction between the shroud leakage flow and the primary flow results in a loss in total pressure and a rise in total temperature. Both effects are localized next to the hub endwall region and their extension depends on the reinjected cavity flow penetration within the primary flow path.

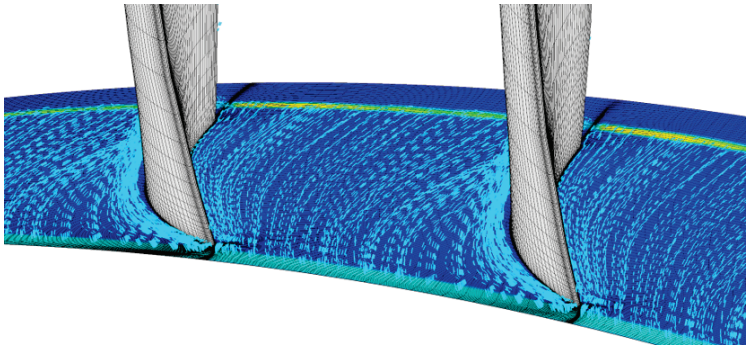

Figure 4.5 Flow visualization close to shroud cavities

A visualization including some streamlines exiting the upstream cavity interface of the shroud and re-entering in the cavity through the downstream interface are shown in Figure 4.5. In the image, velocity magnitude contours are reported on the hub endwall surface.

4.2.5 Clearance models

A reliable evaluation of the behavior in design and off-design conditions of a multi-stage axial compressor cannot be attained without properly modelling the rotor tip clearances. The value of the radial gap between the blade tip and the machine casing

of the rotor rows has a strong influence on the compressor operating range and on the stall margin [73] [74]. Several models of increasing complexity can be used in the TRAF code.

4.2.5.1 Periodicity boundary condition

The simplest and most commonly used clearance model is the one in which periodicity boundary conditions are enforced between the two airfoil sides within the clearance region, obtained by extending the grid from the blade tip to the casing while maintaining the tangential blade thickness. This model is generally referred to as "open tip". All the conservative variables values for each phantom cell on one side of the grid are interpolated, at the same axial position, from the corresponding cells on the other side. This boundary condition is just an approximation of the real configuration in this area, but can lead to really good results especially for thin blades at tip and reasonable values of the clearance thickness, as shown in [75].

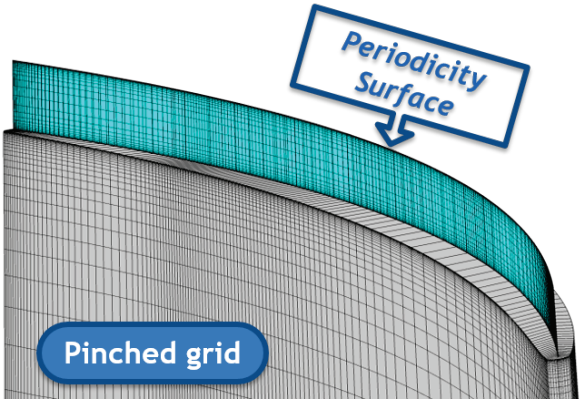

Figure 4.6 Pinched grid for a compressor blade

4.2.5.2 Pinched grid

The need for being able to face cases with high clearances, in which the simplified periodicity method may result in fluxes

conservation errors, has forced the introduction of a more realistic model. By pinching the grid (e. g. [76] [77]) in the clearance region, the use of periodicity boundary conditions between the two grid sides in this area is no longer an approximation. The positive aspects of this solution are the good conservation properties and the fact that a pinched grid allows the solution of the flow field within the clearance region. The only draw-back related with this model is the unavoidable local alteration of the blade tip geometry, that becomes slightly spiky. An example of a pinched grid for the blade of an axial compressor is shown in Figure 4.6.

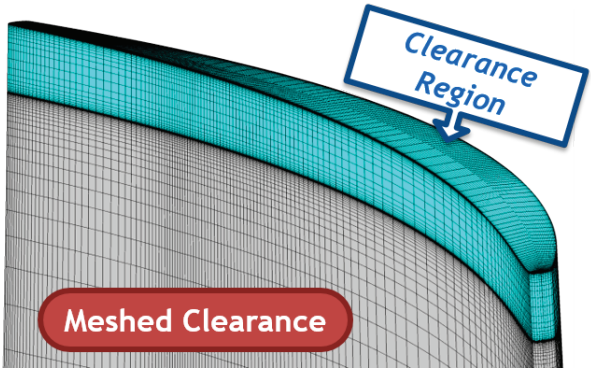

Figure 4.7 Compressor blade with meshed clearance

4.2.5.3 Meshed clearance region

The most advanced model that can be used without introducing any approximation or geometry modification is a meshed clearance region. In this case, a structured O-type grid allows a detailed solution of the flow field inside the clearance. The only disadvantage of this solution is the higher computational cost due to the additional clearance block which is added to the computational domain. An example of axial compressor blade with clearance mesh is represented in Figure 4.7.

4.2.5.4 Models comparison

To compare the clearance models already introduced three steady-state computations on a compressor blade row have been performed. The blade used for the test has a clearance to channel span ratio equal to 1%. Within the 80 cells in the grid spanwise direction, 16 have been used to discretize the clearance region. This choice is the result of a trade-off between resolution in this zone and computational cost. A useful parameter to check the difference between the flow field predictions obtained with the three models is the relative blade-to-blade flow angle at domain outlet section. An outlet radial distribution of flow angle for the test case is shown in Figure 4.8. The slight differences between the distributions are located, as expected, next to the tip endwall in the last 15% of the channel span. The maximum difference registered between the three curves is lower than 0.5°.

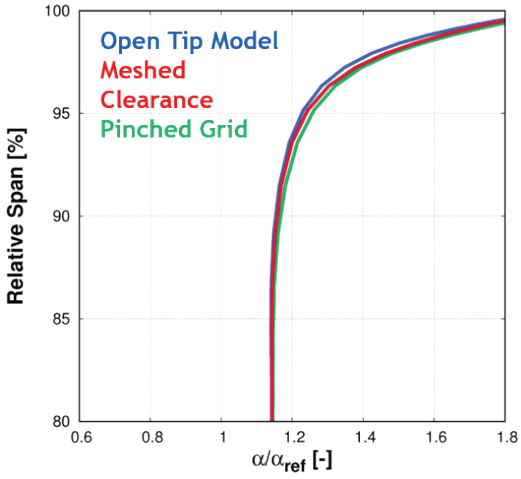

Figure 4.8 Radial exit flow angle distribution for the different clearance models

Another possible way to highlight differences between the available models is a blade-to-blade visualization of the streamlines in the clearance region. Such kind of representation is shown in Figure 4.9.

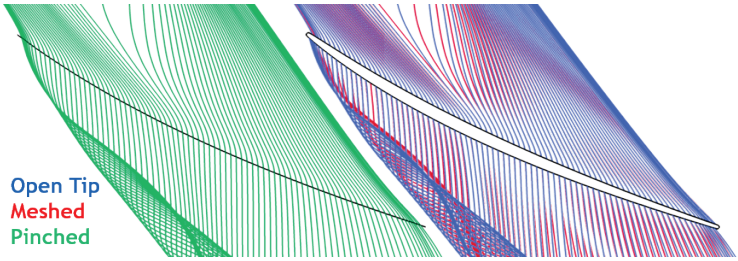

Figure 4.9 Blade-to-blade streamlines in the clearance region for the three clearance models

Both periodicity and pinched grid models lead to a good agreement with the streamlines obtained using the more complex and detailed clearance mesh one. These results confirm that the use of a simplified periodicity boundary condition for the clearance region is an appropriate approximation, especially for axial compressor blades which are commonly really thin at tip section, making this kind of modelling attractive for industrial design purposes. For routine multi-stage axial compressor simulations, the simplified model is used for clearance values lower than 2.5% while, for higher levels, the other options are adopted to avoid possible fluxes conservation issues.

4.3 Validation of the setup

In order to assess the reliability of the computational setup developed within the collaboration between the University of Florence and Ansaldo Energia, a comparison with experimental data has been carried out. The experimental data come from a test campaign handled on an upgraded version of the AE94.3A GT

compressor of the Ansaldo Energia fleet. In this configuration, at design operating conditions, the 15-stage compressor has a pressure ratio of about 19:1 and an inlet mass flow around 735 kg/s. The outline of the turbomachine is shown in Figure 4.10.

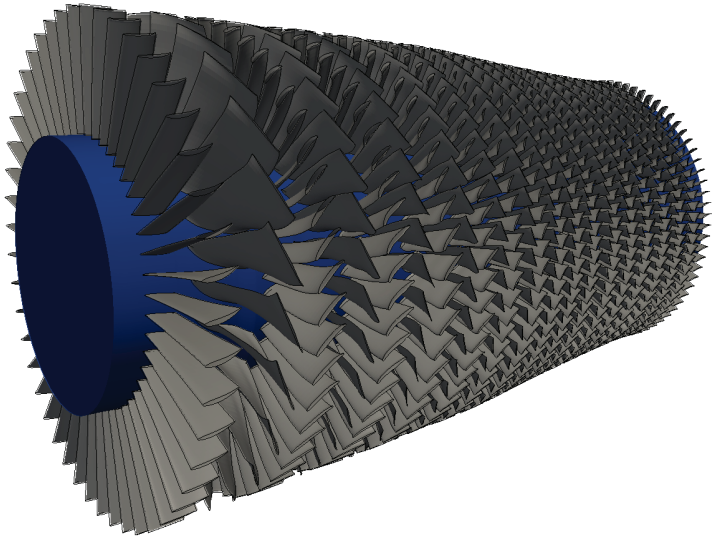

Figure 4.10 Compressor outline

Six measurement stations have been positioned upstream of some of the compressor stator rows. Pressure and temperature static probes have been placed along the meridional flow path at the machine casing. For each measuring station, three probes have been positioned at different, equally spaced, circumferential locations, both for pressure and temperature measurements. The values compared with the numerical results are obtained by averaging the data acquired from the probes at the same axial position.

Two full-compressor steady-state simulations have been performed at the operating condition experimentally tested (design point), using the available mixing plane models.

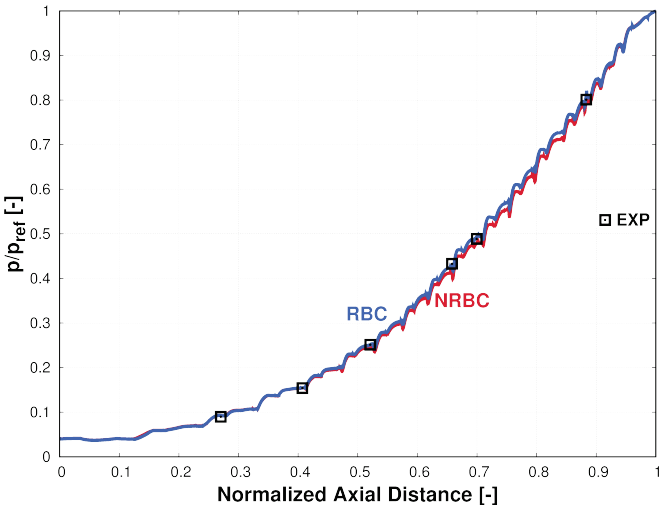

Figure 4.11 Static pressure rise along the meridional channel at machine casing

Figure 4.11 shows the pressure rise along the compressor meridional channel predicted by the numerical simulations and measured on-site. The numerical mean pressure values reported are obtained through a pitchwise averaging process of the 3D solution. In the front part of the machine, up to the third pressure probe, a really good agreement with experimental results is observed. In this part of the compressor, the analyses with different mixing plane models result in a similar predicted pressure rise development. Some differences between numerical computations and experimental data arise in the second part of the machine, especially for the 4^{th} and 5^{th} probe, while for the last

one, closer to the compressor discharge in which the static pressure distribution is enforced as boundary condition, a better agreement is obtained.

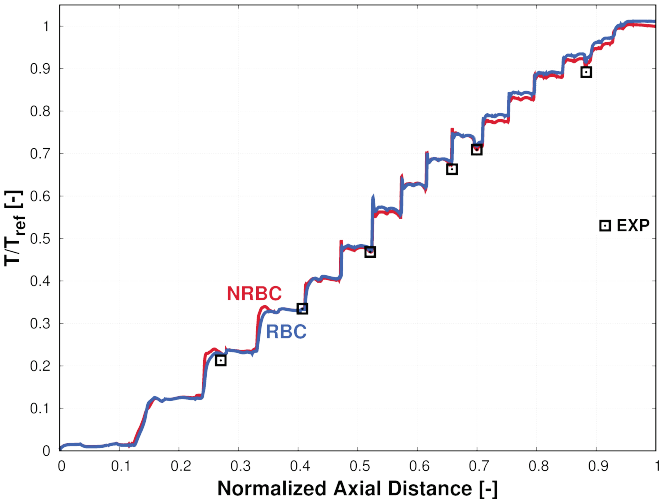

Figure 4.12 Static temperature rise along the meridional channel at machine casing

Simulations results in terms of temperature rise at the casing along the meridional channel are compared with experimental data in Figure 4.12. In this case again, a pitchwise average has been performed on the 3D solutions. Excluding the 2nd and 3rd probe, a general overestimation of the measured values is observed for both the computations. Between the two mixing plane models, the non-reflecting one gets closer to the experiments, mostly predicting a lower temperature level than the one resulting from the other. In general, the numerical analyses tend to forecast higher temperatures with respect to experiments, leading to a lower predicted efficiency.

4.4 Comparison with unsteady results

Due to their really high computational cost, unsteady simulations of a full axial compressor with high stage count are not yet suitable for industrial design purposes. Anyway, unsteady analyses can give useful feedbacks on the reliability of steady-state simulations, which are used as a standard for routine design procedures. In order to assess the impact on performance prediction of the mixing planes, full-annulus unsteady simulations of the whole 15-stage standard AE94.3A compressor have been performed in two different operating conditions: design point and near-stall. Both IGV and OGV rows have been included in the computational domain. The same boundary conditions have been used for steady and unsteady computations.

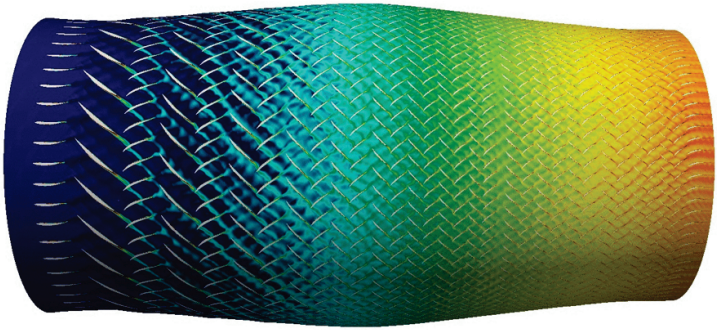

Figure 4.13 Instantaneous entropy field at mid-span for the unsteady full-compressor simulation

The choice of performing a full-annulus unsteady analysis of a compressor with more than 2000 blades instead of a less, computationally speaking, demanding phase-lagged one, has been taken because, especially for near-stall conditions, the interactions between non-adjacent rows may be crucial for the stage matching. In fact, these interactions are not taken into account in a phase-lagged approach, in which only two blade passing

frequencies, the ones referring to the upstream and downstream adjacent rows, are considered in the evaluation of the boundary conditions to be enforced in each computational block, while other perturbations are mixed out at the inter-row interfaces [78]. The typical block size of structured H-type grid used for a blade passage is around 0.75 million of cells, resulting in more than 1.5 billion grid points within the full-annulus computational domain. The time-sampling of the unsteady computations has been imposed considering a trade-off between accuracy and computational costs, adopting 25 time divisions for each blade passage of the row with the highest blade count. Both the operating conditions investigated through an unsteady analysis have required 3 periods to reach periodicity starting from a steady-state solution, each requiring around 7 days using a parallel process involving 200 Intel® E5-2680 V2 CPUs. The difference in terms of computational time with respect to a steady simulation is considerable, the latter requiring about 2 hours running on 32 CPUs. To give an idea of the size of the numerical domain considered for the unsteady analyses, a visualization of the entropy filed at mid-span for the GT compressor considered is shown in Figure 4.13.

4.4.1 Design conditions

The first comparison between steady and unsteady analyses has been carried out at compressor design operating conditions. The results in terms of stage total-to-total pressure ratio are reported in Figure 4.14. In general, a really good agreement between steady-state results with non-reflecting boundary conditions and time-averaged unsteady ones is observed. In the front stages of the compressor, the steady-state simulation with reflecting boundary conditions tends to overestimate the pressure ratio with respect to the full-annulus analysis. On the contrary, it leads to an underestimation in the rear part of the machine.

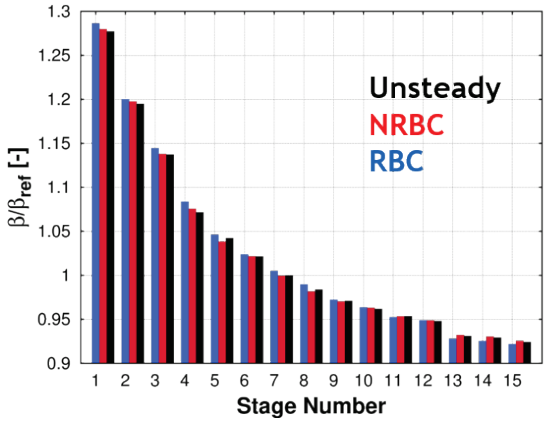

Figure 4.14 Total-to-total stage presure ratio at design point

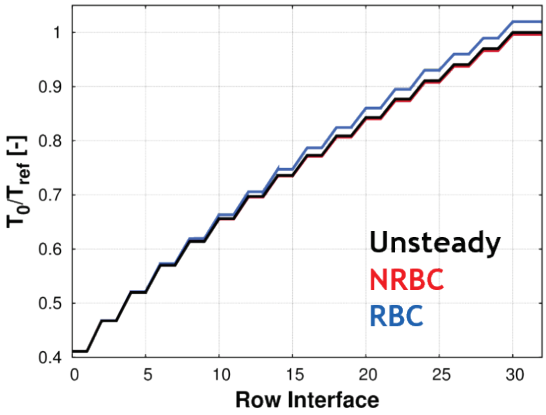

Figure 4.15 Total temperature at row interfaces at design point

The discrepancies between the reflecting steady-state case and the others are even more enhanced when it comes to mass-averaged values of total temperature at row interfaces, shown in Figure 4.15. Both steady-state curves well match the unsteady one up to the end of the second stage. Downstream of this stage

the curve of the steady-state reflecting case starts to diverge from the others, progressively overestimating the total temperature.

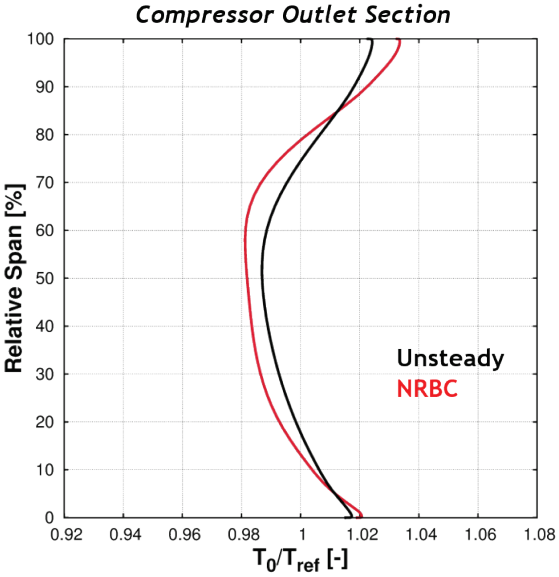

Figure 4.16 Total temperature outlet distribution at design point

Despite the proved good agreement in terms of mean total temperature between the unsteady and the steady non-reflecting cases, the shapes of the radial distribution of this parameter differ for the last stages of the machine, as shown in Figure 4.16, which displays the computed distributions downstream of the last stage stator row. The radial profile obtained through the unsteady simulation is more uniform than the steady one. Something similar has already been observed in literature [79] [80] when comparing experimental temperature profiles in rear stages of multi-stage axial compressors with steady-state CFD

analyses. The more uniform radial temperature profile experimentally measured after several stages is associated with the so called "radial mixing" phenomenon. By accounting for all the interactions between the rows in terms of wakes, potential effects and secondary flows propagation along the flow path, a full-annulus unsteady simulation seems to better predict the effects of radial mixing. A possible explanation could be associated with a major limitation of mixing planes, namely their smoothing-out of actual non-uniformities by pitch-averaging the flow between adjacent rows. On the contrary, the time-accurate calculation allows the growth and the transport of any secondary flow structure throughout the domain, thus enhancing the mixing inherently associated with the streamwise vorticity.

4.4.2 Near-stall conditions

The use of a relatively light and fast steady-state approach with non-reflecting boundary conditions led to a really good approximation of time-averaged unsteady results for the compressor design point. To assess the impact of the steady-state approximation also in off-design, a near-stall condition at compressor nominal speed has been considered. To determine an operating point close to the compressor surge line, various steady state analyses have been performed by progressively increasing the outlet static pressure. The run with higher back-pressure which managed to converge has established the near-stall outlet boundary condition, and the same one has been adopted for the unsteady simulation as well. The comparison results in terms of predicted total-to-total stage pressure ratio are shown in Figure 4.17. A really good agreement between unsteady and steady non-reflecting case is observed for the last five stages of the compressor while, for the front part, some slight discrepancies arise. The reflecting steady-state model generally shows a less accurate match of unsteady results than the non-reflecting one.

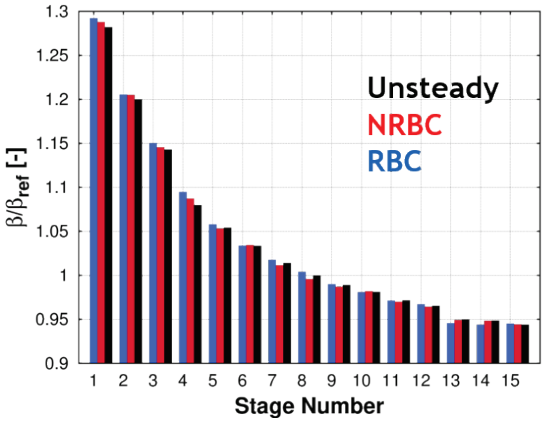

Figure 4.17 Total-to-total stage presure ratio at near-stall condition

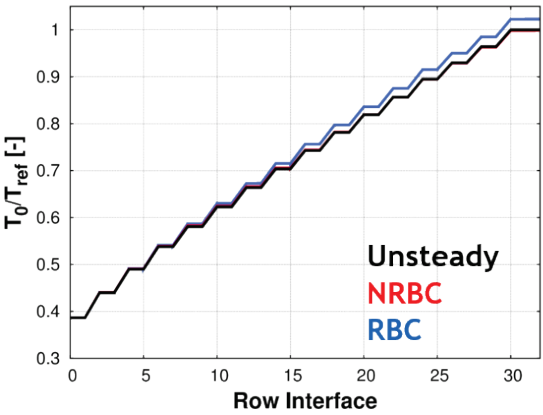

Figure 4.18 Total temperature at row interfaces at near-stall condition

The values of mass-averaged total temperature at row interfaces for the compressor at near-stall conditions are reported in Figure 4.18. In this case, an even better match between steady-state non-reflecting simulation results and unsteady ones is achieved.

Only some slight differences can be found between the two curves in the central stages of the compressor. As seen for the design point, also in this operating condition the steady state analysis with reflecting boundary conditions tends to overestimate the unsteady results immediately after the first two front stages.

As shown in Figure 4.19, the differences in terms of total temperature radial distribution observed at design conditions are enhanced getting closer to compressor stall at nominal speed. The steady distribution has an increased non-uniformity in the span-wise direction with respect to the design point, while the unsteady curve is also in this case more uniform.

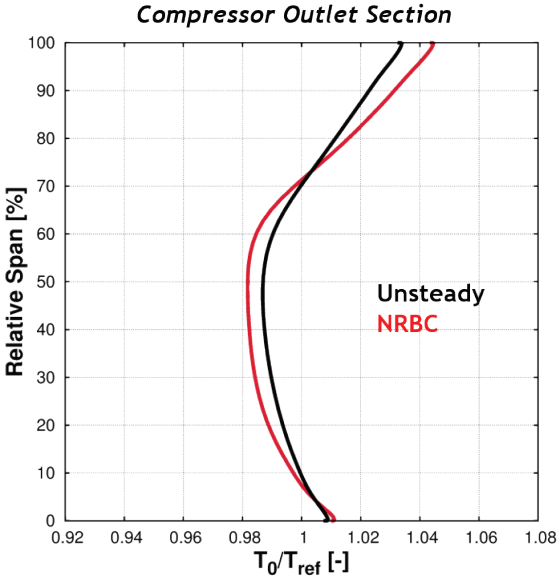

Figure 4.19 Total temperature outlet distribution at near-stall condition

5 Radial Mixing in Axial Compressors

The current industrial standard for numerical simulations of axial compressors is the steady RANS approach. Besides the well-known limitations of mixing planes, namely their inherent inability to capture the potential interaction and the wakes from the upstream blades, there is another flow feature which is lost, and which is a major accountable for the radial mixing: the transport of streamwise vorticity. Streamwise vorticity is generated for various reasons, mainly associated with secondary and tip-clearance flows. A strong link exists between the strain field associated with the vortices and the mixing augmentation: the strain field increases both the area available for mixing and the local gradients in fluid properties, which provide the driving potential for the mixing.

In the rear compressor stages, due to high clearances and low aspect ratios, only accounting for the development of secondary and clearance flow structures it is possible to properly predict the spanwise mixing.

In this chapter, the results of steady and unsteady simulations on a heavy-duty axial compressor are compared with experimental data. Adopting an unsteady framework, the enhanced mixing in the rear stages is properly captured, in remarkable agreement with experimental distributions. On the contrary, steady analyses strongly underestimate the radial transport. It is inferred that the streamwise vorticity associated with clearance flows is a major driver of radial mixing, and restraining it by pitch-averaging the flow at mixing planes is the reason why the steady approach cannot predict the radial transport in the rear part of the compressor.

5.1 Historical background and overview

The CFD modelling of an entire axial compressor with a high stage count is still a great challenge for industrial designers, even with the significantly increased computational resources currently available. Despite the fact that the use of high-fidelity approaches is widely spreading through academia and is already starting to be adopted in some cases by the industry, their huge computational cost allows only simulations restricted to small computational domains and low-Reynolds applications. When dealing with machines characterized by dozens of blade rows and Reynolds numbers greater than 10^6, such kind of approaches cannot obviously even be considered. For industrial design purposes, a compromise between computational cost and simulation accuracy must be found.

The current standard adopted is the multi-stage steady-state RANS approach, while URANS simulations are not yet suitable for a lean industrial design chain. As already introduced in chapter 4, this CFD model was introduced and started to be widely used in the 1990's, but it is really important to understand the inevitable limitations connected with it. Probably, the most crucial one is the fact that the circumferential averaging introduced to be able to model as steady an inherently unsteady case, neglects the effects of blade-row interactions and disrupts the actual development of secondary and clearance flows throughout the flow-path. In particular, due to the introduction of mixing planes, the streamwise vorticity associated with any secondary flow is partially cancelled through the plane itself. A proper description of those flow structures is in fact a key aspect to get good performance predictions for modern axial compressors, which tend to have relatively high stage loadings and low aspect ratios.

A fundamental phenomenon that is strongly enhanced in rear stages of axial compressors is the spanwise transport, better known as "radial mixing". The relevance of this phenomenon was first observed after an experimental campaign conducted by General Electric in the mid 1960's; the spanwise losses distributions after 3-4 compressor stages appeared to be different from the ones expected, with significant losses at mid-span section, in some cases even higher than the values measured next to the endwalls. This suggested that some of the high temperature fluid in the endwall regions was transported towards mid-span by secondary flows. In the following years, several attempts to properly model, with simplified CFD through-flow tools, the radial mixing effects were made. A detailed review of them was done by Wennerstrom [81]. The first comprehensive and somewhat successful model was the one published by Adkins and Smith [82]. The idea from which the model took inspiration was that, from a physical point of view, the radial mixing of fluid properties may be driven by the secondary and clearance flows convection. In particular, they modelled the spanwise mixing as a diffusion process where the variation in the streamwise direction of each fluid property f had the following expression:

$$\frac{\partial \bar{f}}{\partial x} = \varepsilon \frac{\partial^2 \bar{f}}{\partial^2 r} \tag{168}$$

The local values for the mixing coefficient ε were computed from calculated secondary radial velocities. Some years later, Gallimore and Cumpsty pointed out [79] that Adkins and Smith completely neglected the turbulent or "random" mixing, which is a mixing mechanism characterized by disorder and irregular fluctuations typical of a turbulent flow-field. To find out which

mechanism between spanwise convection and turbulent diffusion has the most relevant influence on fluid mixing, they conducted an experimental campaign on two low-speed multi-stage compressors using an ethylene tracer gas technique. From the results obtained, they concluded that non-deterministic turbulent-type diffusion was the major responsible for spanwise mixing. Starting from this outcome, Gallimore developed a radial mixing model based on the turbulent diffusion [83].

As both the abovementioned models showed good agreement with experimental data from multi-stage axial compressor test cases, a great debate about the topic arose within the scientific community. The first relevant attempt to solve the controversy was made by Wisler et al. [84] that conducted further experiments in the General Electric Low Speed Research Compressor (LSRC) facility, on a compressor with four repeating stages. Analyzing the results obtained using the ethylene tracer technique, hot wire anemometry and other experimental methods, the authors concluded that both convective secondary flow transport and turbulent diffusion mechanisms give a fundamental contribution to the radial mixing phenomenon. Despite this remarkable publication, the discussion on the topic continued for some years leaving the question unresolved. The resolution of the debate was reached only through a paper published by Leylek and Wisler [85], which reinforced the conclusion that radial mixing is caused by a combination of secondary flows convection and turbulent diffusion, while the relative importance of these two mechanisms depends on the specific configuration and on the loading level. The most interesting aspect of this work was the use of a 3D viscous CFD code to support experimental results.

When dealing with axial compressors with a high stage count (e.g. the ones typical of heavy-duty and power generation applications), secondary and clearance flows in rear stages do have a relevant impact on spanwise redistribution of flow properties, as blade rows tend to have low aspect ratios and high clearance levels. As shown in chapter 4, an unsteady RANS simulation on a multi-stage compressor leads to more uniform outlet radial total temperature distributions than the ones obtained from a steady-state analysis, indeed being more in agreement with what has always been observed in experimental test cases.

To gain a better understanding of the reasons why this happens and to assess which of the secondary flow contributions is the one that has the major impact on the spanwise mixing, in the present chapter results from steady and unsteady computations on the high-pressure section of a GT compressor of the Ansaldo Energia fleet will be shown. In particular, three different computational domains, with increasing degree of realism, will be considered to analyze the influence on radial mixing of the various secondary flow components, in a compressor section composed of 5 stages. The abovementioned numerical environments are the following: inviscid end-walls without clearances, viscous end-walls without clearances and viscous end-walls, with clearances. Moreover, multi-stage steady and unsteady results, coming from simulations performed using experimental data as boundary conditions, will be compared with measured outlet radial distributions.

5.2 Case study

The case study considered for the work presented in this chapter is the high-pressure section of a heavy-duty axial compressor. A meridional view of it is shown in Figure 5.1. This machine seg-

ment consists of five stages with cantilevered vanes. The annulus height and radius are nearly constant. The last vane has a higher chord with respect to the other rows. This solution has been adopted to allow an increased flow turning needed to remove the flow swirl before the diffuser inlet section. In contrast to the other cantilever stator rows, the hub endwall for this last vane is stationary. The blades and vanes have low aspect ratios. Inlet Mach numbers are in the range 0.3-0.5, while the overall pressure ratio is around 1.4. As far as clearances are concerned, the actual value in heavy-duty applications is mainly determined by the thermal state of the machine. In particular, the minimum values are usually reached after a "hot restart", where the casing is relatively cold with respect to the rotor. On the contrary, the maximum values are touched starting from a cold state after a certain time interval. This because the thermal time response of the casing is usually faster than the one of the rotor.

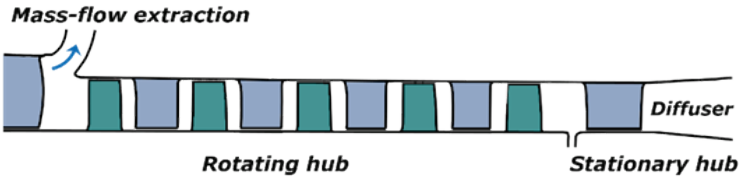

Figure 5.1 Meridional view of the high-pressure section of the compressor adopted as case study

Experimental measurements are available in terms of radial distributions of total temperature and pressure at the compressor outlet, over the span of the last vane. The experimental tests have been performed with high clearance level, up to 5% of the blade height. The instrumentation consists of Kiel probes with pressure transducer and thermocouple mounted on vane leading edges for five different radial positions. This allows to measure

the profiles of total pressure and temperature. At the compressor outlet, the probes are mounted on a rod. For each measuring plane, three rakes are installed at different tangential positions in order to check the non-uniformity of the flow.

5.3 Computational framework

In order to perform more accurate analyses, some differences with respect to the standard numerical setup reported in chapter 4 have been introduced for the simulations whose results will be presented in the following sections of this chapter. In particular, the main change is the use of the two-equation k−ω model in combination with elliptic O-type grids to discretize the blades within the computational domain. The choice of this different grid topology is due to numerical issues registered close to the blade trailing edge when using the k−ω model with H-type grids, which have a metrics discontinuity in this area. Only the duct connecting the low and the high-pressure sections has been meshed with H-type grids.

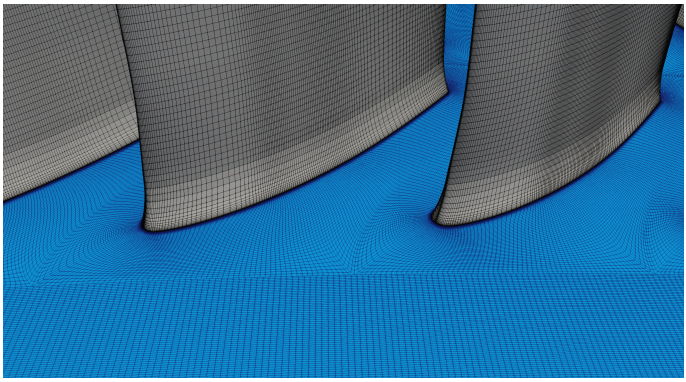

Figure 5.2 View of the HP compressor mesh

The typical dimensions of each grid block used to discretize the blades are 281×61×101 points, resulting in about 1.7 million

nodes. To have a detailed solution of clearance flows, O-type structured grids have been introduced to model blade tip and cantilever-vane hub gaps.

5.4 Simplified multi-row environment

The radial mixing of fluid properties in a multi-stage axial compressor is given by a combination of secondary flows convection and turbulent diffusion. In a CFD simulation adopting a RANS approach, turbulence is not solved but its effect on the average flow-field is modelled by introducing a turbulence closure. Also when adopting an unsteady RANS approach, only large-scale vortical structures are properly solved, while smaller scale phenomena are just modelled. Therefore, in first approximation, the contribution of turbulent diffusion to radial transport is of the same order of magnitude for both steady and unsteady approaches. On the other hand, with unsteady analyses, it is possible to assess the impact of secondary flows convection on radial mixing process.

To quantify the contribution of each secondary flow structure, mainly endwall and clearance components, three steady and unsteady simulations with an increasing degree of realism have been performed in a simplified multi-row environment. The analyses have been limited to the 5 high-pressure stages of the compressor to avoid the need for modelling the significant mass-flow extraction immediately downstream of the last low-pressure compressor vane. To focus on the effect of secondary flows generated in the high-pressure section on the outlet radial distributions, the simulations have been run with the perfect gas version of the TRAF code and adopting uniform boundary conditions upstream of the first rotor row of the computational domain. The three models that have been compared are the following:

- inviscid end-walls, without clearances
- viscous end-walls, without clearances
- viscous end-walls, with clearances

The first model has been introduced with the aim of representing what would happen in the high-pressure compressor section without any secondary flow influence on the primary flow; the second model is intended to quantify the effects on spanwise mixing due to endwall generated secondary flows, while the third one takes account for all the secondary flow convection contributions. As far as unsteady simulations are concerned, between the options available in TRAF code, namely full-annulus and phase-lagged approaches, the former has been chosen for the investigations whose results are presented within this chapter. The full-annulus analysis has been selected because of its capability to take into account also for the interactions between non-adjacent rows. These interactions are not transmitted in the phase-lagged approach implemented in TRAF code [78], which considers only the upstream and downstream blade passing frequencies in the evaluation of the boundary conditions to be enforced in each computational block, while the other perturbations are mixed out at the interfaces. Regarding the time-sampling for unsteady analyses, 25 time divisions for blade passage for the row with the highest blade count have been used, this value being a trade-off between accuracy and computational cost. Although 50 time divisions may be considered as a standard choice for this kind of unsteady runs [66], preliminary tests on smaller domains demonstrated that a lower frequency resolution was sufficient for the purposes of the present application.

The computed radial distributions of average total temperature at compressor outlet section for the three models already introduced are shown in Figure 5.3.

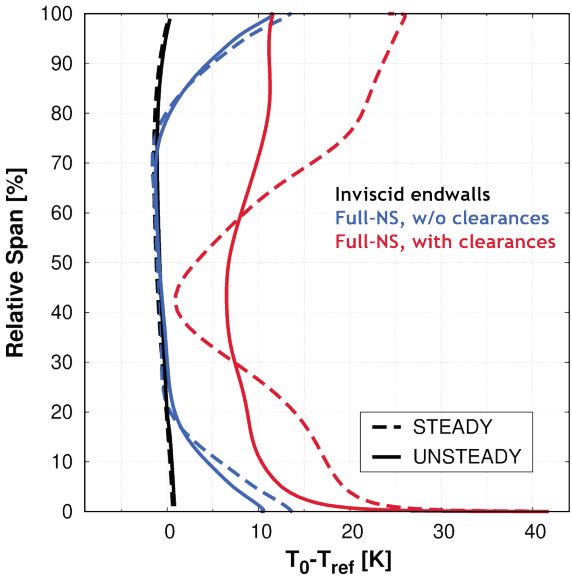

Figure 5.3 Total temperature profile at compressor outlet

As expected, the inviscid endwalls without clearance case leads to a fairly uniform total temperature profile, with negligible differences between steady and unsteady runs. The minor shift in the distributions, with higher temperature values for the unsteady curve, is due to the higher losses of this case, deriving from wake/blade interactions within the computational domain. Considering the model with viscous endwalls and without clearances, the steady-state and unsteady distributions tend to have uniform trend and similar values from 25% to 75% of channel span. As for the first model, the slightly higher total temperature predicted by the URANS computation in this region comes from multi-row wake interactions. Getting close to the endwalls, the two curves start to diverge with just some traces of spanwise temperature redistribution towards mid-channel. For this case, modelling all blade rows as shrouded, only secondary

flows originated from the endwalls can develop within the fluid domain. The most significant differences between steady and unsteady results arise for the last model introduced, the one with viscous endwalls and clearances modelled, both for rotors and cantilever stators. The unsteady profile has an almost uniform trend along the channel span, while the steady one has conspicuous total temperature variations with higher values close to the endwalls and lower values in the mid-channel region. Bearing in mind these significant differences, clearance flows seem to have a major impact on the radial mixing process. Furthermore, the steady-state analysis appears to be unable to properly predict the phenomenon, which is particularly enhanced in this specific application.

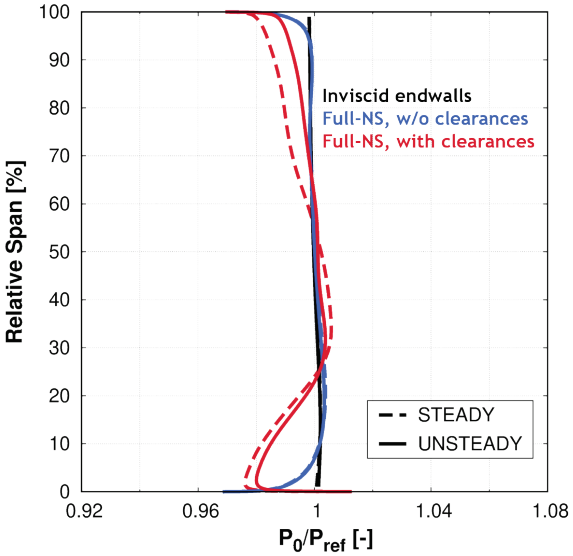

Figure 5.4 Total pressure distribution at compressor outlet

The comparison results in terms of average outlet total pressure distributions are presented in Figure 5.4. As for the total temperature, the steady and unsteady pressure curves obtained for the inviscid endwalls model without clearances are really similar, with almost no pressure variation in the spanwise direction. For the other models, the secondary flows have a relevant effect also on the outlet total pressure profile. In analogy with the total temperature plot, the biggest differences between steady and unsteady modelling can be found in the fully viscous analysis with clearances. The different trend shown by the red and blue curves next to the hub is related to the fact that in the model with clearances the hub endwall is rotating, while it is fixed in the other case.

An instantaneous entropy field visualization of the whole high-pressure segment of the compressor at mid-span, coming from the viscous endwalls with clearances analysis, is shown in Figure 5.5. As uniform boundary conditions at domain inlet section have been enforced, the flow is "clean" upstream of the first rotor row and only downstream of it wakes start to grow and propagate throughout the flow-path.

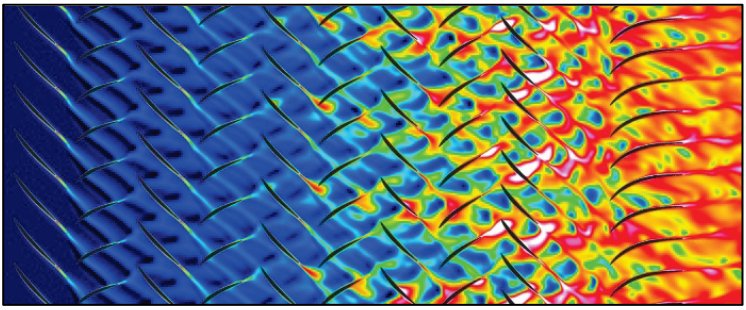

Figure 5.5 Instantaneous entropy field at mid-span section

Even if the focus of this chapter is on the radial mixing, it is worth noting that the large differences found in the outlet radial distributions at compressor outlet do have a deep impact on the aerodynamic loading of the blades. To emphasize this, an example is reported in Figure 5.6, in which the averaged pressure distributions along the blade surface for the last rotor row are displayed. In the figure, the curves resulting from steady and unsteady computations of the viscous endwalls with clearances model refer to a blade-to-blade section at 80% span. The blade loadings and especially the incidence angle of the flow at blade leading edge resulting from steady and unsteady analyses are completely different; while the former predicts positive incidence and high loading in the front part of the airfoil, the latter leads to slightly negative incidence and lower loading close to the leading edge.

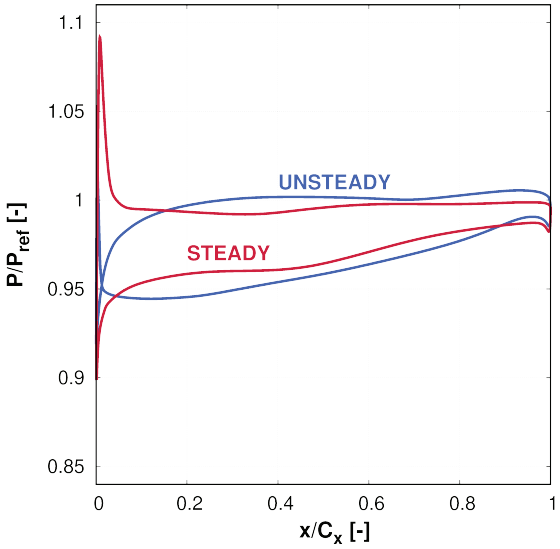

Figure 5.6 Pressure distributions at 80% blade span for the last rotor row

From a broader perspective, moving the working condition towards the compressor surge-line, with more intense secondary and clearance flows than the ones found within the present design point investigation, the steady-state simulation will underpredict the compressor stall margin.

5.5 Stream-wise vorticity, mixing and mixing planes

The focus of the present chapter is indeed on the impact of accounting for the transport of all the flow field features in the CFD analysis of axial compressors. It is inferred, in particular, that a proper URANS modelling enables to capture the so-called "radial mixing". It is worth emphasizing that the prominent feature of the flow field that needs to be transported is in fact the streamwise vorticity.

In this section, the goal is in showing that much of the exit flow field structure is associated with the transport and distortion of the vorticity through the compressor, in particular the one that is formed in the tip clearances.

The streamwise component of vorticity is commonly referred to as secondary flow, assuming that one can identify a primary flow direction and hence specify the departures from this primary direction. In an axial compressor with high values of tip clearances, anyway, looking at the clearance flows as to secondary flows can be misleading, because the cross-flow velocities are often a substantial fraction of the primary velocity. Under these conditions, the streamwise vorticity is a powerful agent for enhancing mixing, as a strong link does exist between mixing augmentation and the strain field associated with the vortices. As well described by Greitzer [86], the vortical strain field increases both the area available for mixing between adjacent streams and

the local gradients in fluid properties. Both provide the driving potential for mixing. Furthermore, as the transport and evolution of secondary flows within the flow-path is developed in a predominantly inviscid manner [86], the impact of turbulence modelling has just a second order influence on this contribution to the radial mixing phenomenon.

As highlighted in the previous section, a steady-state simulation may strongly underestimate the radial transport of the main fluid properties typical of multi-stage compressor applications, leading to errors that could not be negligible in design phase. In order to give a possible explanation of the reason why this underestimation afflicts the steady-state calculation, a flow vorticity component is considered, namely the one in the axial direction. In cylindrical coordinates, this quantity has the following expression:

$$\omega_x = \frac{1}{r}\left(\frac{\partial(r v_\theta)}{\partial r} - \frac{\partial v_r}{\partial \theta}\right) = \underbrace{\frac{v_\theta}{r} + \frac{\partial v_\theta}{\partial r}}_{Term\ 1} - \underbrace{\frac{1}{r}\frac{\partial v_r}{\partial \theta}}_{Term\ 2} \tag{169}$$

The axial vorticity may be divided in two terms. The first one is accounting for radial non-uniformities, while the other one is associated with circumferential flow-field non-uniformities. In the steady-state approach, both tangential and spanwise velocity components are circumferentially averaged at each interface between consecutive rows. When adopting a non-reflecting approach, as the one implemented in the TRAF code, a zero-mean value small perturbation is then superimposed on the averaged values for the governing variables in order to avoid non-physical reflections, but all tangential distributions are irremediably lost.

Bearing in mind this and considering the axial vorticity decomposition introduced in equation (169), it is clear that Term 2 is essentially cancelled throughout a mixing plane, while Term 1 assumes, at every radius, a fundamentally uniform distribution in the circumferential direction.

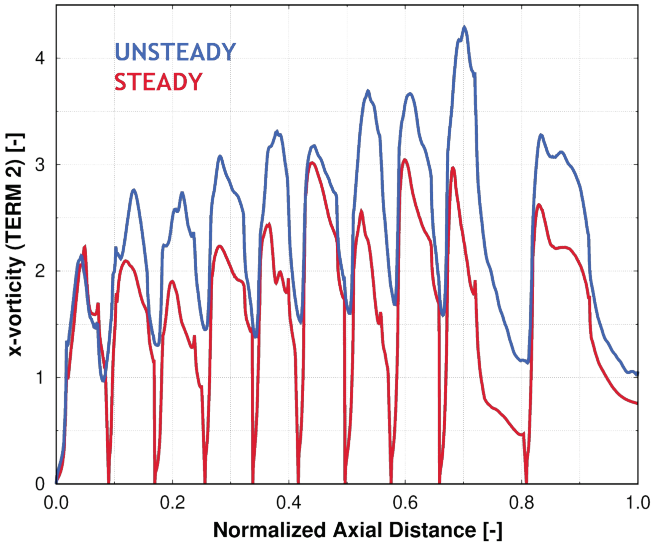

Figure 5.7 Development of the integral value of Term 2 magnitude along the meridional flow-path

The trend of the integral value for Term 2 magnitude along the meridional flow-path is shown in Figure 5.7. Both steady and unsteady curves refer to the simulations run for the model with viscous endwalls and with clearances. For the unsteady case, an instantaneous distribution is displayed to avoid the smoothing-out of the curve that would lead to a similar trend of the steady one, if a time-averaged solution were considered. The main difference between the two curves is the value assumed by the

plotted quantity at row interfaces; while for the steady computation the Term 2 tends to zero at each inter-row interface, for the time-accurate one the decay of this term within the axial inter-row gap after each blade passage stops next to the interfaces reaching a value different from zero. Starting from a non-zero value at each block inlet boundary of embedded blade rows, this axial vorticity component is significantly higher for the unsteady case.

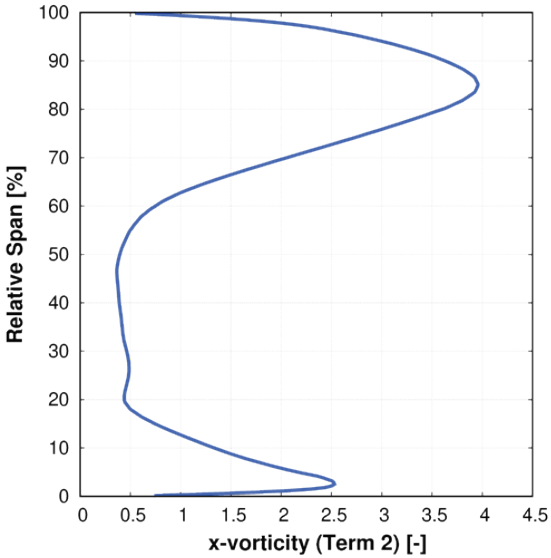

Figure 5.8 Spanwise distribution of Term 2 magnitude upstream of a rotor/stator interface for an unsteady computation

To better understand the sources that contribute to generate the axial vorticity component associated with circumferential non-uniformities, a radial distribution of Term 2 downstream of a rotor row and close to the interface with the following vane is

displayed in Figure 5.8. The plot is the result of the post-processing of an unsteady instantaneous solution, which has been pitchwise averaged along all the annulus. As clearly depicted by the figure, the regions with the higher value for Term 2 are the ones close to hub and tip endwalls. In particular, the upper 50% of channel span is the one in which this vorticity component reaches its peak value. Therefore, the clearance flow coming from rotor tip gaps has a major impact on this term, while secondary flows generated from the endwalls have just a second order contribution to the integral value of Term 2.

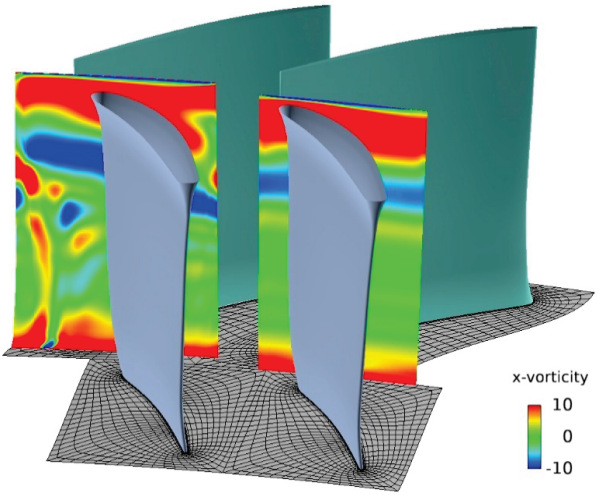

Figure 5.9 Axial vorticity field upstream and downstream of an inter-row interface for a steady-state analysis (only one fourth of grid lines are shown for sake of clarity)

As shown in Figure 5.9, the axial vorticity field undergoes substantial modifications across the mixing plane of a steady-state simulation. All circumferential non-uniformities that can be found in the cross-section upstream of the interface, mainly due to the development of secondary flows within the blade passage,

are smoothed-out, leading to an axial vorticity field with variations constrained only to the radial direction. Since Term 2 of equation (169) is deleted across the mixing plane, only a pitchwise average of Term 1 is transmitted to the following blade row. This considerable alteration of the axial vorticity across each interface may probably be one of the main sources of the radial mixing underestimation typical of the steady-state approach. By introducing the tangential averaging process, the transport of streamwise vorticity throughout the compressor is limited and the mixing enhancement associated with it is strongly reduced.

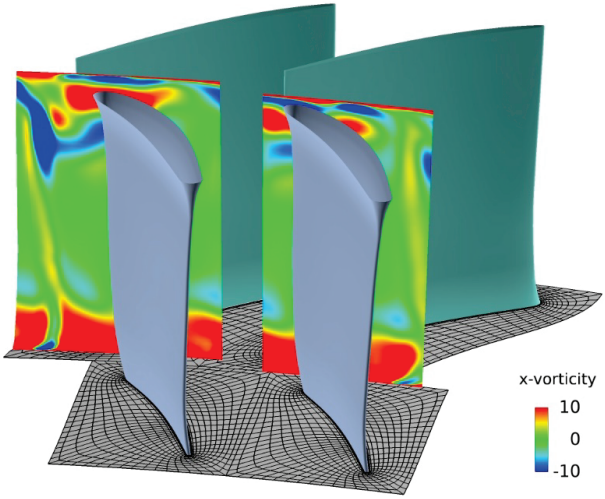

Figure 5.10 Axial vorticity field upstream and downstream of an inter-row interface for an unsteady analysis (only one fourth of grid lines are shown for sake of clarity)

On the other hand, as showed in Figure 5.10, for the unsteady case the axial vorticity is completely transmitted without any kind of alteration, and its contribution to the spanwise transport

of fluid properties is fully taken into account. The image reported in Figure 5.10 comes from the post-processing of an instantaneous unsteady solution.

5.6 Unsteady analysis of the actual compressor

Once shown the great differences in terms of radial distributions coming from RANS and URANS simulations performed on the aft section of a multi-stage axial compressor, characterized by low aspect ratios and high clearances, a comparison with experimental data may help quantifying the reliability of the radial mixing prediction resulting from these two numerical approaches. As the compressor experimentally tested has a very high stage count, to limit the computational resources requested by the unsteady computation (i.e. the computational blocks included in the fluid domain), the smallest aft portion of it included within two consecutive measuring stations has been considered. The first radial distributions available upstream of the high-pressure section are the ones acquired right in front of the last vane of the low-pressure compressor segment. Hence, the fluid domain consists of five and a half stages with a mass-flow extraction located between the first stator row and the following rotor row. The last measuring section with total pressure and temperature rakes is placed on the leading edge of the last stator row of the compressor.

As inlet boundary conditions for the numerical analyses, the experimental total pressure and temperature profiles have been used, while the spanwise flow-angle distribution has been taken from a full-compressor simulation. The experimental static pressure level measured at the machine casing in the domain outlet section has been used to enforce a radial equilibrium boundary condition. Both RANS and URANS analyses have been carried out with the real gas version of the TRAF code, to adopt the

most realistic numerical setup available at the cost of increasing by around 30% the overall computational time.

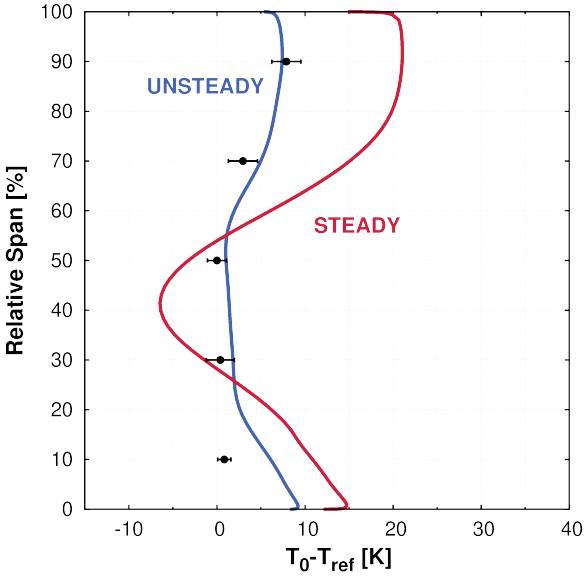

Figure 5.11 Average radial distributions of total temperature upstream of the last high-pressure compressor vane

The averaged radial total temperature distributions of the steady and unsteady computation are compared with the experimental data acquired from the rakes in Figure 5.11. The significantly high level of spanwise transport shown by the averaged unsteady profile is confirmed by the experimental results, which show variations in the spanwise direction of less than 10 degrees. On the contrary, the steady-state profile shows deeper total temperature differences along the channel span, with remarkably high values close to the endwalls and lower temperatures in the mid-span region. For this particularly challenging application, characterized by strongly 3D flow structures due to the high clearances, the steady approximation gives results that are

quite far from the experimental data, both in terms of mean value and spanwise variation of the total temperature and pressure.

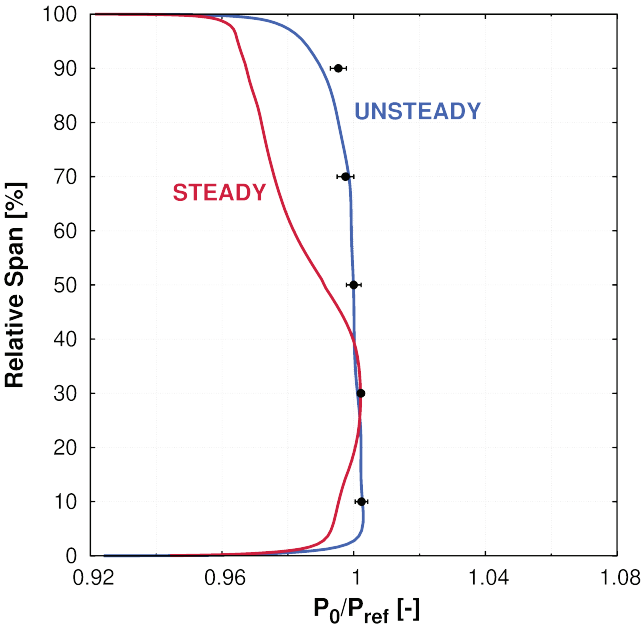

Figure 5.12 Average radial distributions of total pressure upstream of the last high-pressure compressor vane

The radial distributions of total pressure at last measuring section are presented in Figure 5.12. While the unsteady computation profile is in really good agreement with experimental data, the steady one shows remarkable departures, especially in the upper 50% of channel span, which is an area largely influenced by the clearance flow coming from the upstream blade row.

Finally, in order to provide an example of the strong impact of clearance flows for the application investigated within this chap-

ter, a streamline visualization of the flow-field features developed in the tip gap region of one of the rotor blades is displayed in Figure 5.13.

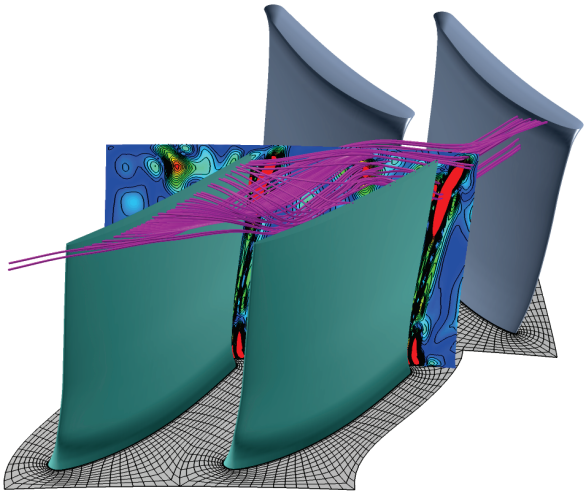

Figure 5.13 Clearance flow and axial vorticity contours visualization in a blade passage (only one fourth of grid lines are shown for sake of clarity)

6 Conclusions

In this thesis, the main outcomes of a research activity aimed to use and tune modern CFD methods to assess a numerical setup for multi-stage simulations on axial compressors, have been presented. Most of the activities have been carried out in the framework of the collaboration between the research group led by Professor Arnone and the industrial partner Ansaldo Energia, one of the main competitors in the world market of large-size turbomachinery for power generation.

The first part of the work has been focused on the implementation of a non-reflecting mixing plane model for steady-state RANS simulations in the in-house CFD code TRAF. In the development of the model, particular attention has been paid to fluxes conservation both in terms of mass-flow and total temperature. The model has also been extended to the real gas case, by removing all the perfect gas assumptions present in the classic non-reflecting boundary condition theory. The key differences with respect to the perfect gas implementation are an iterative procedure to compute mixed-out quantities from the mean fluxes of the governing conservative variables through the interface and the use of numerical derivatives instead of analytical expressions in some of the terms within the transformation matrix from primitive to conservative variables. Some results on a demanding multi-row environment characterized by small inter-row gaps and a shock structure reaching one mixing plane have been presented, showing the good behavior of the model both in terms of non-reflectiveness and fluxes conservation.

In the following part of the thesis, an advanced numerical setup for steady-state multi-stage axial compressor simulations, currently adopted by Ansaldo Energia, has been presented. Some crucial aspects of the compressor modelling have been addressed, namely shroud leakages and rotor tip clearances. In particular, the shroud leakage model adopted has been tested on a single-row case, to assess the influence of cavity flows on the mainstream. All available clearance models have been presented and compared, showing that for compressor blades a simplified periodicity boundary condition can lead to a good approximation of clearance flows. The numerical setup has been validated on a compressor designed and experimentally tested by Ansaldo Energia. To determine the influence of mixing plane models on performance prediction, unsteady full-annulus simulations of a whole 15-stage compressor have been performed at two different operating conditions: design point and near-stall. The comparison between steady and unsteady computations demonstrated a really good agreement in terms of averaged values. Some interesting differences between steady and unsteady results arose in the radial distribution of total temperature at compressor outlet, showing that the unsteady analysis predicts a smoother temperature profile. Bearing in mind that experimental measurements on axial compressors have always shown more spanwise mixing than CFD results, this outcome seems of particular interest and deserves an in-depth analysis, which is in fact the object of the last part of the thesis.

Finally, the results coming from steady and unsteady RANS simulations on the high-pressure section of an industrial heavy-duty axial compressor have been presented and compared with experimental data acquired during a test campaign. The machine portion considered well exemplifies the features of rear stages of multi-stage axial compressors, characterized by low

blade aspect ratios and really high clearance values. Both these features tend to promote the growth and the development of intense secondary flows along the compressor flow-path. As secondary flows convection has, along with turbulent diffusion, a crucial impact on the radial transport of fluid properties, better known as radial mixing, the case considered has been used to evaluate the influence of each source of secondary flow on the overall radial transport phenomenon. In order to achieve this goal, numerical analyses with different models of increasing complexity have been performed, showing that clearance flows have a higher influence on the radial transport than endwall generated secondary flow structures. Only adopting an unsteady full-annulus approach, the enhanced radial mixing in the rear stages of the compressor has been properly captured. A really good agreement with experimental data has been obtained, in terms of both total temperature and pressure radial distributions immediately ahead of the last compressor vane. On the contrary, with a steady-state modelling, the radial transport has been strongly underestimated, leading to results with marked departures from experiments. Focusing on what occurs across the inter-row interfaces for RANS and URANS solutions, a possible explanation for this underestimation has been provided. In particular, as the streamwise vorticity associated with clearance flows is one of the main drivers of radial mixing, limiting it by pitch-averaging the flow at mixing planes of a steady-state analysis is the reason why this simplified approach is not able to properly predict the radial transport of fluid properties in the rear part of the axial compressor.

An interesting future development sparkled from the present work could be the introduction of a modification in the RANS model aimed to make the steady-state analysis able to attain some improvements in the radial mixing prediction. From the

above discussion, one may infer that the inability of a steady analysis to capture the radial mixing is essentially associated with the lack of convection of the streamwise vorticity across the mixing planes. Bearing in mind this limitation, one could try to re-include in the calculation the main effect of vorticity by acting on another mixing driver, which could provide a similar outcome. In particular, similarly to what has already been elaborated in through-flow methods, a possible solution could be to enhance the turbulent viscosity in order to promote diffusion. In doing this, the streamwise vorticity upstream of each mixing plane could be exploited to quantify such enhancement. The implementation of this idea is in fact the object of an ongoing activity.

References

[1] J. Weatheritt and R. Sandberg, "A novel evolutionary algorithm applied to algebraic modifications of the RANS stress-strain relationship," *Weatheritt, J., & Sandberg, R. (2016). A novel evolutionary algorithm applied to algebraic modifications of Journal of Computational Physics,* vol. 325, pp. 22-37, 2016.

[2] H. D. Akolekar, J. Weatheritt, N. Hutchins, R. D. Sandberg, G. Laskowski and V. Michelassi, "Development and Use of Machine-Learnt Algebraic Reynolds Stress Models for Enhanced Prediction of Wake Mixing in Low Pressure Turbines," in *Proceedings of ASME Turbo Expo 2018*, Oslo, Norway, 2018.

[3] S. Saito, K. Yamada, M. Furukawa, K. Watanabe, A. Matsuoka and N. Niwa, "Flow Structure and Unsteady Behavior of Hub-Corner Separation in a Stator Cascade of a Multi-Stage Transonic Axial Compressor," in *Proceedings of ASME Turbo Expo 2018*, Oslo, Norway, 2018.

[4] L. Cozzi, F. Rubechini, M. Marconcini, A. Arnone, P. Astrua, A. Schneider and A. Silingardi, "Facing the Challenges in CFD Modelling of Multistage Axial Compressors," in *Proceedings of ASME Turbo Expo 2017: Turbomachinery Technical Conference and Exposition*, Charlotte, NC, USA, 2017.

[5] L. Cozzi, F. Rubechini, M. Giovannini, M. Marconcini, A. Arnone, A. Schneider and P. Astrua, "Capturing Radial

Mixing in Axial Compressors With CFD," in *Proceedings of ASME Turbo Expo 2018: Turbomachinery Technical Conference and Exposition*, Oslo, Norway, 2018.

[6] G. Stoney, "Scientific Activities of the Late Hon. Sir Charles Parsons," *F.R.S. Engineering,* vol. 144, pp. 632-695, 1937.

[7] R. A. Howell, "Fluid Dynamics of Axial Compressors," *Proc. Inst. Mech. Eng.,* vol. 153, no. 1, pp. 441-452, 1945.

[8] H. R. Cox, "British Aircraft Gas Turbines," *Journal of the Aeronautical Sciences,* vol. 13, no. 2, pp. 53-83, 1946.

[9] H. Constant, "The Gas Turbine in Perspective," *Proc. Inst. Mech. Eng.,* vol. 163, no. 1, pp. 185-192, 1950.

[10] A. J. Wennerstrom, "Highly Loaded Axial Flow Compressors: History and current Development," *J. Turbomach.,* vol. 112, pp. 567-578, 1990.

[11] A. J. Wennerstrom, "Low Aspect Ratio Axial Flow Compressors: Why and What it Means," *J. Turbomach.,* vol. 111, pp. 357-365, 1989.

[12] D. C. Wisler, "Advanced Compressor and Fan Systems," GE Aircraft Engines, Cincinnati, Ohio, USA, 1988.

[13] S. L. Dixon and C. A. Hall, Fluid Mechanics and Thermodynamics of Turbomachinery, 7th ed., Elsevier Inc., 2014.

[14] A. D. S. Carter, "Low-Speed Performance of Related Aerofoils in Cascade," *ARC Current Paper,* no. 29, 1950.

[15] S. Lieblein, F. C. Schwenk and R. L. Broderick, "Diffusion Factor for Estimating Losses and Limiting Blade Loadings in Axial Flow Compressor Blade Elements," NACA RM E53D01, 1953.

[16] S. Lieblein, "Incidence and Deviation-Angle Correlations for Compressor Cascades," *Journal of Basic Engineering,* vol. 82, pp. 575-587, 1960.

[17] P. De Haller, "Das verhalten von tragflügelgittern in axialverdichtern und im windkanal," *BWK Zeitschrift,* vol. 5, no. 10, pp. 333-337, 1953.

[18] C. C. Koch and L. Smith, "Loss Sources and Magnitudes in Axial-Flow Compressors," *J. Eng. Power,* vol. 98, no. 3, pp. 411-424, 1976.

[19] C. Freeman, "Effect of tip clearance flow on compressor stability and engine performance," Von Karman Institute for Fluid Dynamics, Lecture Series 1985-0, 1985.

[20] L. H. Smith, "Recovery ratio—A measure of the loss recovery potential of compressor stages," *Transactions of the American Society of Mechanical Engineers,* vol. 80, no. 3, 1958.

[21] T. Dickens and I. J. Day, "The design of highly loaded axial compressors," *J. Turbomach.,* vol. 133, no. 3, 2011.

[22] C. C. Koch, "Stalling pressure rise capability of axial flow compressors," in *Transactions of the American Society of Mechanical Engineer, paper 97-GT-535*, 1997.

[23] N. A. Cumpsty, Compressor Aerodynamics, Longman Scientific & Technical, 1989.

[24] B. S. Baldwin and H. Lomax, "Thin Layer Approximation and Algebraic Model for Separated Turbulent Flows," *AIAA paper 78--257,* 1978.

[25] D. Degani and L. B. Schiff, "Computation of Turbulent Supersonic Flows Around Pointed Bodies Having Crossflow Separation," *Journal of Computational Physics,* vol. 66, pp. 173-196, 1986.

[26] A. Arnone and R. Pacciani, "IGV-Rotor Interaction Analysis in a Transonic Compressor Using the Navier--Stokes Equations," *ASME Journal of Turbomachinery,* vol. 120, pp. 143-155, 1 1998.

[27] P. R. Spalart and S. R. Allmaras, "A One-equation Turbulence Model for Aerodynamic Flows," *AIAA Paper 92-0439,* 1 1992.

[28] P. R. Spalart and M. Shur, "On the Sensitization of Turbulence Models to Rotation and Curvature," *Aerospace Science and Technology,* vol. 1, pp. 297-302, 1997.

[29] D. C. Wilcox, Turbulence Modeling for CFD, 2nd ed., DCW Ind. Inc., La Cañada, CA, USA, 1998.

[30] F. R. Menter, "Two-Equations Eddy Viscosity Turbulence Models for Engineering Applications," *AIAA J.,* vol. 32, pp. 1598-1605, 8 1994.

[31] D. C. Wilcox, "Formulation of the k-ω Turbulence Model Revisited," *#AIAAJ#,* vol. 46, pp. 2823-2838, 11 2008.

[32] A. Jameson, W. Schmidt and E. Turkel, "Numerical Solutions of the Euler Equations by Finite Volume Methods Using Runge--Kutta Time--Stepping Schemes," *AIAA paper 81--1259,* 1981.

[33] R. H. Ni, "A Multiple-Grid Scheme for Solving the Euler Equations," *AIAA paper 81-1025,* 1981.

[34] D. Holmes and S. Tong, "A Three-Dimensional Euler Solver for Turbomachinery Blade Rows," *ASME J. Eng. Gas Turbines Power,* vol. 117, no. 2, pp. 258-264, 1985.

[35] R. C. Swanson and E. Turkel, "On Central-Difference and Upwind Schemes," *Journal of Computational Physics,* vol. 101, pp. 292-306, 1992.

[36] L. Martinelli and A. Jameson, "Validation of a Multigrid Method for Reynolds Averaged Equations," *AIAA paper 88--0414,* 1988.

[37] R. C. Swanson and E. Turkel, "Artificial Dissipation and Central Difference Schemes for the Euler and Navier--Stokes Equations," *AIAA paper 87--1107--CP,* 1987.

[38] P. L. Roe and M. J. Baines, "Algorithms for advection and shock problems," in *Proceedings of the Fourth GAMM Conference on Numerical Methods in Fluid Mechanics, Notes on Numerical Fluid Mechanics, 5; p. 281*, Vieweg, 1981.

[39] M. Arora and P. L. Roe, "A Well-Behaved TVD Limiter for High-Resolution Calculations of Unsteady Flow," *Journal of Computational Physics,* vol. 132, pp. 3-11, 1997.

[40] A. Arnone, "Viscous Analysis of Three–Dimensional Rotor Flow Using a Multigrid Method," *J. Turbomach.,* vol. 116, no. 3, pp. 435-445, 1994.

[41] A. Arnone, M. S. Liou and L. A. Povinelli, "Integration of Navier-Stokes Equations Using Dual Time Stepping and a Multigrid Method," *AIAA Journal,* vol. 33, pp. 985-990, 6 1995.

[42] A. Arnone, "Multigrid Methods for Turbomachinery Navier-Stokes Calculations," in *Solution Techniques for Large--Scale CFD Problems*, 1995.

[43] A. Lerat, "Une Classe de Schemas aux Differences Implicites Pour les Systemes Hyperboliques de Lois de Conservation," *Comptes Rendus Hebdomadaires des Seances de l'Academic des Sciences, Series A: Sciences Mathematiques,* vol. 288A, 1979.

[44] A. Jameson, "The Evolution of Computational Methods in Aerodynamics," *J. Appl. Mech.,* vol. 50, 1983.

[45] A. Brandt, "Multi-Level Adaptive Computations in Fluid Dynamics," *AIAA paper 79-1455,* 1979.

[46] M. Giovannini, M. Marconcini, A. Arnone and A. Dominguez, "A Hybrid Parallelization Strategy of a CFD Code for Turbomachinery Applications," in *11th European*

Turbomachinery Conference, paper ETC2015-188, Madrid, 2015.

[47] P. Boncinelli, F. Rubechini, A. Arnone, M. Cecconi and C. Cortese, "Real Gas Effects in Turbomachinery Flows: a CFD Model for Fast Computations," *ASME paper 2003--GT--38101,* 2003.

[48] J. L. Steger and R. L. Sorenson, "Automatic Mesh Point Clustering Near a Boundary in Grid Generation with Elliptic Partial Differential Equations," *Journal of Computational Phisycs,* vol. 33, pp. 405-410, 12 1979.

[49] M. B. Giles, "Nonreflecting Boundary Conditions for Euler Equation Calculations," *AIAA Journal,* vol. 28, pp. 2050-2058, 1990.

[50] M. B. Giles, "UNSFLO: A Numerical Method For Unsteady Inviscid Flow in Turbomachinery," 1988.

[51] A. P. Saxer and M. B. Giles, "Quasi-Three-Dimensional Nonreflecting Boundary Conditions for Euler Equations Calculations," *Journal of Propulsion and Power,* vol. 9, pp. 263-271, 3 1993.

[52] H. C. Yee, R. M. Beam and R. F. Warming, "Stable Boundary Approximations for the One-Dimensional Inviscid Equations of Gas Dynamics," in *AIAA Paper 81-1009*, 1981.

[53] G. Fritsch, An Analytical and Numerical Study of the Second-Order Effects of Unsteadiness on the Performance of Turbomachines, MIT: PhD Thesis, 1992.

[54] M. B. Giles, "Non-Reflecting Boundary Conditions for the Euler Equations," 1988.

[55] M. L. Mansour, J. Gunaraj and S. Goswami, "Validation of Steady Average-Passage and Mixing Plane CFD Approaches for the Performance Prediction of a Modern Gas Turbine Multistage Axial Compressor," in *ASME Turbo Expo 2008, Paper No. GT2008-50653*, Berlin, Germany, 2008.

[56] C. Cornelius, T. Biesinger, P. Galpin and A. Braune, "Experimental and Computational Analysis of a Multistage Axial Compressor Including Stall Prediction by Steady and Transient CFD Methods," *J. Turbomach.,* vol. 136, no. 3, pp. 061013-061013-12, 2013.

[57] A. Wiedermann, D. Frank, U. Orth and M. Beukenberg, "Computational and Experimental Analysis of an Industrial Gas Turbine Compressor," in *Proceedings of ASME Turbo Expo 2011, Paper No. GT2011-46336*, Vancouver, Canada, 2011.

[58] J. J. Adamczyk, "Aerodynamic Analysis of Multistage Turbomachinery Flows in Support of Aerodynamic Design," in *ASME 1999 International Gas Turbine and Aeroengine Congress and Exhibition, Paper No. 99-GT-080*, Indianapolis, USA, 1999.

[59] J. D. Denton, "An Improved Time-Marching Method for Turbomachinery Flow Calculation," *J. Eng. Power,* vol. 105, no. 3, pp. 514-521, 1983.

[60] M. B. Giles, "Non–Reflecting Boundary Conditions for the Euler Equations," Tech. rep., MIT Dept. of Aero. and Astro., CFDL Report 88-1, 1988.

[61] R. Chima, "Calculation of Multistage Turbomachinery Using Steady Characteristic Boundary Conditions," in *36th Aerospace Sciences Meeting & Exhibit, Paper No. AIAA 98-0968*, Reno, USA, 1998.

[62] D. G. Holmes, "Mixing Planes Revisited: A Steady Mixing Plane Approach Designed to Combine High Levels of Conservation and Robustness," in *ASME Turbo Expo 2008, Paper No. GT2008-51296*, Berlin, Germany, 2008.

[63] L. Hanimann, L. Mangani, E. Casartelli, T. Mokulys and S. Mauri, "Development of a Novel Mixing Plane Interface Using a Fully Implicit Averaging for Stage Analysis," *J. Turbomach.,* vol. 136, no. 8, p. 081010, 2014.

[64] F. Gisbert and R. Corral, "A Novel Mixing Plane Method Using Nonreflecting Boundary Conditions for Multirow Analysis in Turbomachines," *J. Turbomach.,* vol. 138, no. 7, p. 071009, 2016.

[65] J. D. Denton, "Some Limitations of Turbomachinery CFD," in *ASME Turbo Expo 2010, Paper No. GT2010-22540*, Glasgow, UK, 2010.

[66] F. Rubechini, M. Marconcini, M. Giovannini, J. Bellucci and A. Arnone, "Accounting for Unsteady Interaction in Transonic Stages," *J. Eng. Gas Turbines Power,* vol. 137, no. 5, pp. 052602-052602-9, 2015.

[67] D. G. Holmes, B. J. Moore and S. D. Connell, "Unsteady vs. Steady Turbomachinery Flow Analysis: Exploiting Large-Scale Computations to Deepen our Understanding of Turbomachinery Flows," in *SciDAC Conference*, Denver, USA, 2011.

[68] J. B. Young, "An Equation of State for Steam for Turbomachinery and Other Flow Computations," *ASME J. Fluids Eng.,* vol. 110, pp. 1-7, 1988.

[69] F. Rubechini, M. Marconcini, A. Arnone, M. Maritano and S. Cecchi, "The Impact of Gas Modeling in the Numerical Analysis of a Multistage Gas Turbine," *J. Turbomach.,* vol. 130, no. 2, pp. 021022-021022-7, 2008.

[70] P. Astrua, E. Puppo, S. Cecchi and A. Silingardi, "A Method for Axial Compressor Start-Up Assessment," in *ASME Turbo Expo 2015, Paper No. GT2015-42445*, Montréal, Canada, 2015.

[71] S. R. Wellborn, I. Tolchinsky and T. H. Okiishi, "Modeling Shrouded Stator Cavity Flows in Axial Flow Compressors," *ASME Journal of Turbomachinery,* vol. 122, no. 1, pp. 55-61, 2000.

[72] F. Rubechini, M. Marconcini, A. Arnone, S. Cecchi and F. Daccà, "Some Aspects of CFD Modeling in the Analysis of a Low-Pressure Steam Turbine," in *Proceedings of ASME Turbo Expo 2007, Paper No. GT2007-27235*, Montréal, Canada, 2007.

[73] W. W. Copenhaver, E. R. Mayhew, C. Hah and A. R. Wadia, "The Effect of Tip Clearance on a Swept Transonic

Compressor Rotor," *J. Turbomach.,* vol. 118, no. 2, pp. 230-239, 1996.

[74] J. J. Adamczyk, M. L. Celestina and E. M. Greitzer, "The Role of Tip Clearance in High-Speed Fan Stall," *J. Turbomach.,* vol. 115, no. 1, pp. 28-38, 1993.

[75] R. V. Chima, "Calculation of Tip Clearance Effects in a Transonic Compressor Rotor," *J. Turbomach.,* vol. 120, no. 1, pp. 131-140, 1998.

[76] J. A. Storer and N. A. Cumpsty, "Tip Leakage Flow in Axial Compressors," *J. Turbomach.,* vol. 113, no. 2, pp. 252-259, 1991.

[77] A. J. Crook, E. M. Greitzer, C. S. Tan and J. J. Adamczyk, "Numerical Simulation of Endwall and Casing Treatment Flow Phenomena," *J. Turbomach.,* vol. 115, no. 3, pp. 501-512, 1993.

[78] M. Giovannini, M. Marconcini, A. Arnone and F. Bertini, "Evaluation of Unsteady Computational Fluid Dynamics Models Applied to the Analysis of a Transonic High-Pressure Turbine Stage," *Part A: Journal of Power and Energy,* vol. 228, no. 7, p. 813–824, 2014.

[79] S. J. Gallimore and N. A. Cumpsty, "Spanwise Mixing in Multistage Axial Flow Compressors: Part I - Experimental Investigation," *J. Turbomach.,* vol. 108, no. 1, pp. 2-9, 1986.

[80] S. J. Gallimore, «Spanwise Mixing in Multistage Axial Flow Compressors: Part II - Throughflow Calculations

Including Mixing,» *J. Turbomach.,* vol. 108, n. 1, pp. 10-16, 1986.

[81] A. J. Wennerstrom, "A Review of Predictive Efforts for Transport Phenomena in Axial Flow Compressors," *J. Turbomach.,* vol. 113, pp. 175-179, 1991.

[82] G. G. Adkins and L. H. Smith, "Spanwise Mixing in Axiai-Fiow Turbomachines," *Journal of Engineering for Power,* vol. 104, pp. 97-104, 1982.

[83] S. J. Gallimore, "Spanwise Mixing in Multistage Axial Flow Compressors: Part II - Throughflow Calculations Including Mixing," *J. Turbomach.,* vol. 108, pp. 10-16, 1986.

[84] D. C. Wisler, R. C. Bauer and T. H. Okiishi, "Secondary Flow, Turbulent Diffusion, and Mixing in Axial-Flow Compressors," *J. Turbomach.,* vol. 109, no. 4, pp. 455-482, 1987.

[85] J. H. Leylek and D. C. Wisler, "Mixing in Axial-Flow Compressors: Conclusions Drawn From 3-D Navier-Stokes Analyses and Experiments," *J. Turbomach.,* vol. 113, no. 2, pp. 139-155, 1991.

[86] E. M. Greitzer, C. S. Tan and M. B. Graf, Internal Flow. Concepts and Applications, Cambridge: Cambridge University Press, 2004.